Concerted electron-proton transfer in the optical excitation of hydrogen-bonded dyes

Brittany C. Westlake, M. Kyle Brennaman, Javier J. Concepcion, Jared J. Paul, Stephanie E. Bettis, Shaun D. Hampton, Stephen A. Miller, Natalia V. Lebedeva, Malcolm D. E. Forbes, Andrew M. Moran, Thomas J. Meyer[1], and John M. Papanikolas[1]

Department of Chemistry, University of North Carolina at Chapel Hill, Chapel Hill, NC 27599

Contributed by Thomas J. Meyer, March 28, 2011 (sent for review February 10, 2011)

The simultaneous, concerted transfer of electrons and protons—electron-proton transfer (EPT)—is an important mechanism utilized in chemistry and biology to avoid high energy intermediates. There are many examples of thermally activated EPT in ground-state reactions and in excited states following photoexcitation and thermal relaxation. Here we report application of ultrafast excitation with absorption and Raman monitoring to detect a photochemically driven EPT process (photo-EPT). In this process, both electrons and protons are transferred during the absorption of a photon. Photo-EPT is induced by intramolecular charge-transfer (ICT) excitation of hydrogen-bonded-base adducts with either a coumarin dye or 4-nitro-4′-biphenylphenol. Femtosecond transient absorption spectral measurements following ICT excitation reveal the appearance of two spectroscopically distinct states having different dynamical signatures. One of these states corresponds to a conventional ICT excited state in which the transferring H^+ is initially associated with the proton donor. Proton transfer to the base (B) then occurs on the picosecond time scale. The other state is an ICT-EPT photoproduct. Upon excitation it forms initially in the nuclear configuration of the ground state by application of the Franck–Condon principle. However, due to the change in electronic configuration induced by the transition, excitation is accompanied by proton transfer with the protonated base formed with a highly elongated $^+$H—B bond. Coherent Raman spectroscopy confirms the presence of a vibrational mode corresponding to the protonated base in the optically prepared state.

electron transfer | proton-coupled electron transfer

Proton-coupled electron transfer (PCET), in which electrons and protons are both transferred, is at the heart of many energy conversion processes in chemistry and biology (1–6). PCET reactions can occur by sequential two-step transfers (e.g., electron transfer followed by proton transfer, ET-PT, or proton transfer followed by electron transfer, PT-ET) or by concerted electron-proton transfer (EPT) (1, 2). EPT pathways are important in avoiding high-energy intermediates, playing an integral role in photosynthesis and respiration, for example.

Photo-driven EPT (photo-EPT), with electron and proton transfers occurring simultaneously during the optical excitation process, would appear to be ruled out on fundamental grounds, because electronic excitation occurs rapidly on the time scale for nuclear motions, including proton transfer. Using a combination of femtosecond pump-probe and coherent Raman techniques, we have observed simultaneous electron-proton transfer induced by intramolecular charge transfer (ICT) excitation in two different hydrogen-bonded adducts formed between an organic dye (A—O—H) and an external base (:B). One is formed between a *para*-nitrophenyl-phenol and an amine base, and the other between a coumarin derivative and an imidazole base (Fig. 1).

The shift in electron density away from the hydroxyl group to the intramolecular acceptor during ICT excitation greatly enhances the acidity of the hydrogen-bonded proton and leads to proton transfer in the excited state (7–9). Initially, the proton in the optically prepared ICT excited state is located

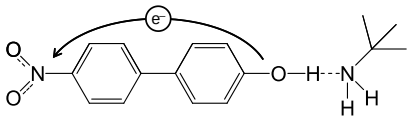

(1) Nitrophenyl-Phenol / t-Butylamine

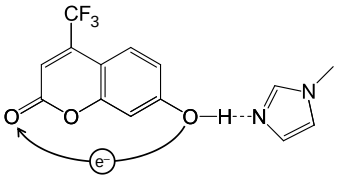

(2) Hydroxy-Coumarin / Methyl Imidazole

Fig. 1. Chemical structures of the two hydrogen-bonded adducts studied in this work: (1) 4-hydroxy-4′-nitro-biphenyl (para-nitrophenyl-phenol) and *t*-butylamine (TBA) in 1,2 dicholoro-ethane (DCE). Hydrogen bonding is confirmed for a range of bases in a variety of solvents using UV-visible and direct infrared absorption. (2) 7-hydroxy-4-(trifluoromethyl)-coumarin and 1-methylimidazole in toluene. Evidence of hydrogen-bonding in the ground state is observed by shifts in the coumarin absorption spectrum.

at the equilibrium coordinate of the A—O—H ground state, $(^{-\cdot}A—O^{\cdot}—H^+\cdots:B)^*$. In a conventional proton transfer event, H^+ motion occurs after excited state equilibration in coupled vibrational and solvent modes. The stepwise process is analogous to ET-PT with excitation (ET) followed by proton transfer and has been studied by several groups using ultrafast methods (9–12). Conversely, the same configuration produced by vertical excitation could also be viewed as an ICT-EPT photoproduct. In this product, the proton has transferred to the nitrogen in concert with the change in electronic configuration induced by the optical excitation. A protonated base is formed with a highly elongated $^+$H—N bond[†]—i.e., $(^{-\cdot}A—O^{\cdot}\cdots{}^+H—B)^*$ (Fig. 2). A predicted spectroscopic signature of such an "ICT-EPT" transition would be possible appearance of a second optically accessible excited state and the instantaneous appearance of an H^+—N vibrational mode.

Results and Discussion

We report here results on two systems in which ICT to an internal electron acceptor is accompanied by proton transfer to an

Author contributions: M.D.F., A.M.M., T.J.M., and J.M.P. designed research; B.C.W., M.K.B., J.J.C., J.J.P., S.E.B., S.D.H., S.A.M., and N.V.L. performed research; B.C.W., M.K.B., J.J.P., M.D.F., A.M.M., T.J.M., and J.M.P. analyzed data; and T.J.M. and J.M.P. wrote the paper.

The authors declare no conflict of interest.

[†]The femtosecond laser pulses used here most likely do not have the bandwidth to excite an H-N vibrational wavepacket. As a consequence, the excited state nuclear wavefunction probably extends to some degree across the ICT-EPT well.

[1]To whom correspondence may be addressed. E-mail: tjmeyer@unc.edu or John_Papanikolas@unc.edu.

This article contains supporting information online at www.pnas.org/lookup/suppl/doi:10.1073/pnas.1104811108/-/DCSupplemental.

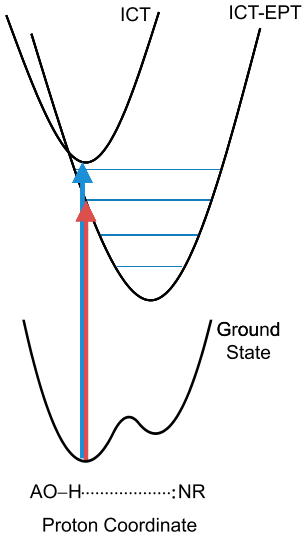

Fig. 2. Illustration of the ICT and ICT-EPT energy-coordinate surfaces. Red and blue arrows illustrate excitation wavelengths used in this work. Excitation of the ICT state (blue arrow) results in delayed proton transfer. Proton transfer occurs concomitantly with excitation to the ICT-EPT state (red arrow).

external base. Structures are shown in Fig. 1. In both cases, the hydroxyl group on the chromophore forms an intermolecular hydrogen bond with a nitrogen-containing base in solution—i.e., A—O—H···:B.

We present results first on the hydrogen-bonded adduct formed between *para*-nitrophenyl-phenol and *t*-butylamine (**1**) in 1,2-dichloroethane (DCE). Spectroscopic measurements (IR, UV visible) demonstrate hydrogen-bond formation in the ground state—i.e., A—O—H···:B. Femtosecond transient absorption experiments performed at different excitation wavelengths on the hydrogen-bonded adduct reveal two optically accessible states that produce different photoproducts. In one, the H-bonded proton is still associated with the oxygen atom. In the other, it is bound to the base but, by application of the Franck–Condon principle, through an elongated H^+—N bond. Coherent Raman spectra of the optically prepared state obtained at the moment of excitation show the appearance of a $\nu(H^+—N)$ mode at higher frequency, consistent with transfer of the proton to the base during the ICT excitation process. A similar feature is observed in ultrafast Raman spectra of the hydrogen-bonded adduct formed between hydroxy-coumarin and 1-methyl-imidazole (**2**) in toluene.

***Para*-nitrophenyl-phenol.** ICT absorption in *para*-nitrophenyl-phenol promotes an electron from a nonbonding orbital on the oxygen to the nitro group, producing a $^1(n\pi^*)$ charge transfer excited state (Fig. 1).

Analysis of ground-state absorption spectra for a series of organic bases shows that the ICT absorption band at 335 nm systematically shifts to lower energy as the O—H bond is weakened through hydrogen bonding, ultimately leading to deprotonation. Hydrogen-bond formation with bases ranging from *t*-butylamine ($pK_a = 10.7$) to pyridine ($pK_a = 5.25$) in DCE result in incremental shifts in the ICT absorption band with increasing base strength from $\lambda_{max} = 335$ nm (no base) to a limiting value of 354 nm for *t*-butylamine. For *t*-butylamine, $K_A = 104 \pm 10\ M^{-1}$ at 23 ± 2 °C with adduct formation >90% complete with 0.3 mM *para*-nitrophenyl phenol and 90 mM base. The latter were the experimental conditions used in the transient experiments.

Complete deprotonation of the phenol occurs upon addition of tetra-*n*-butylammonium hydroxide, which further red shifts the ICT absorption to $\lambda_{max} = 466$ nm. The intermediate proton transfer state, A—O^-···H^+—:B, cannot be accessed experimentally; however, DFT calculations suggest that its ICT absorption lies at 410 nm between the absorptions for the hydrogen-bonded (354 nm) and deprotonated forms of the phenol (466 nm). The position of the ICT absorption provides a spectroscopic indicator of the location of the proton in the ground state, ranging from 335 nm (A—O—H) to 354 nm (A—O—H···:B) to 410 nm (A—O^-···$^+$H—B) to 466 nm (A—O^-). Examination of the ground-state absorption spectrum (Section I.B, *SI Appendix*) shows no evidence of significant concentrations of either deprotonated anion (A—O^-) or proton transfer adduct (A—O^-···$^+$H—B). These observations are consistent with both states lying energetically above the hydrogen-bonded adduct.

The acidity in the ICT excited state is enhanced by approximately 9 pK_a units, resulting in a large driving force for proton transfer after photoexcitation. We have used a combination of femtosecond transient absorption and coherent Raman spectroscopies to probe the structure of the optically prepared state and the dynamics that take place following photon absorption. Details regarding observations and analysis can be found in Sections I.C and III of the *SI Appendix*.

Femtosecond transient absorption spectra of the hydrogen-bonded adduct show evidence for three excited state absorption bands between 400 and 700 nm. The spectra obtained one picosecond following excitation of the free *para*-nitrophenyl-phenol and the hydrogen-bonded adduct (**1**) are shown in Fig. 3.

Excitation of free phenol at 355 nm in DCE results in an absorption band with $^1\lambda_{max} = 440$ nm (labeled S_a in Fig. 3). It is assigned to an excited state absorption from the singlet $^1n\pi^*$ ICT state—i.e., $^1(^{-\cdot}A—O^{\cdot}—H^+)^*$. The singlet undergoes rapid ($\tau \sim 3$ ps) intersystem crossing to the corresponding $^3n\pi^*$ state, $^1(^{-\cdot}A—O^{\cdot}—H^+)^* \rightarrow {}^3(^{-\cdot}A—O^{\cdot}—H^+)^*$, giving rise to the red absorption band at $^3\lambda_{max} = 630$ nm, denoted T_a. The triplet character of the red absorption was verified by transient EPR measurements at 77 K in a toluene glass (*SI Appendix*) and the intersystem crossing time observed here is comparable to that observed for $n\pi^*$ states in nitrobenzenes (13). The T_a band reaches its maximum amplitude within a few ps and then decays, without a change in spectral position on a time scale of 2–3 μs.

The singlet and triplet bands are also observed in the transient absorption spectra of the hydrogen-bonded adduct (A—O—H···:B), Fig. 3. These absorptions depend upon excitation wavelength and exhibit complex temporal evolution including changes in both the amplitude and position of the bands. Our analysis of the transient spectra, which is discussed in detail in the *SI Appendix*, correlates observations of the spectral evolution from fs to μs, at two different excitation wavelengths, 355 nm and 388 nm.

The singlet and triplet absorptions observed following 388 nm excitation of the adduct (S_c and T_c) are both shifted to higher energy relative to the free phenol, with λ_{max} at 395 nm and 570 nm, respectively. While the singlet absorption decays with $\tau \sim 4.5$ ps, the triplet absorption shows no appreciable evolution during the first 300 ps after excitation.

With 355 nm excitation, the singlet band is shifted to higher energy relative to the unassociated phenol with λ_{max} at 410 nm (Fig. 3). The triplet band appears at $\lambda_{max} = 620$ nm at early pump-probe delays, similar to the phenol itself (Section I.C.1, *SI Appendix*).

Careful examination of the singlet absorption reveals that the red and blue edges decay with different kinetics, consistent with two unresolved absorptions with different decay characteristics (Section 1.C.2, *SI Appendix*). The decay on the lower-energy side is kinetically correlated with the growth of the triplet absorption at 630 nm ($\tau \sim 1.5$ ps), a clear indication that it arises from the singlet ICT state, $^1(^{-\cdot}A—O^{\cdot}—H^+\cdots:B)^*$. The higher-energy side decays more slowly with $\tau \sim 4.5$ ps. This is identical to the lifetime

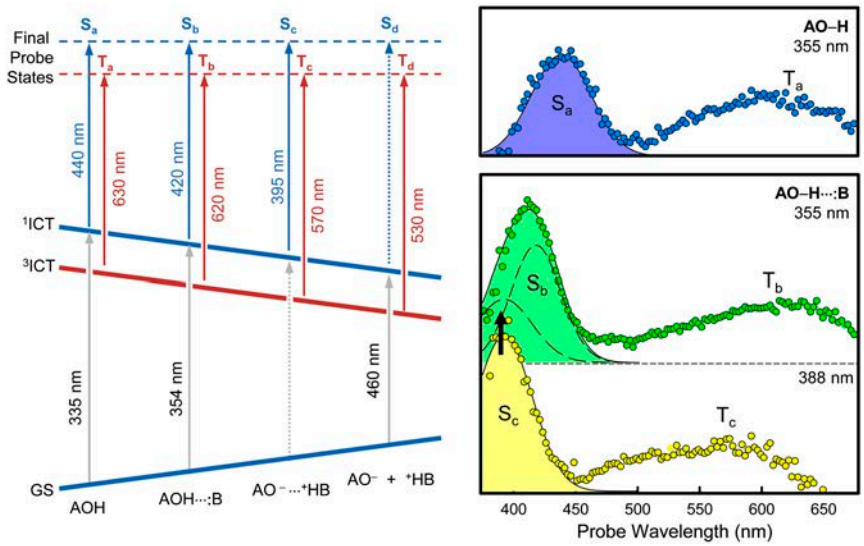

Fig. 3. Transient absorption spectra at early pump-probe delay times of 4-hydroxy-4′-nitro-biphenyl (nitrophenyl-phenol) (*Upper*, right) and the hydrogen-bonded adduct with *t*-butylamine (TBA) (*Lower*, right) in 1,2 dicholoro-ethane (DCE). All spectra were observed 1.0 ps after photoexcitation. The free phenol spectrum was obtained after photoexcitation at 355 nm. Two spectra for the hydrogen-bonded adduct are shown, collected at 355 nm and the other at 388 nm. The diagram at the left illustrates the band assignments made by correlation of a wide array of experimental observations (see *SI Appendix*). The dashed gray and blue arrows indicate transitions that are not observed experimentally.

of S_c, suggesting that it and the unresolved higher-energy contribution in the 355 nm spectrum arise from the same transition. Taking this contribution to have the same position and spectral width as S_c enables a deconvolution of the two unresolved absorptions and suggests that the lower-energy absorption (S_b) has its λ_{max} at 420 nm. These two bands (S_b and S_c) are depicted by the dashed lines beneath the singlet absorption band in the 355 nm spectrum.

The shift of the singlet absorption from 440 nm in free *para*-nitrophenyl-phenol (S_a) to 420 nm when hydrogen bonded to the amine (S_b) indicates that the excited state absorption in the ICT state is also sensitive to the location of the proton, shifting to the blue as the O—H bond weakens. With this observation the appearance of the feature at $\lambda_{max} \approx 395$ nm is consistent with a $^1n\pi^*$ ICT state that has a considerable degree of proton transfer character—i.e., $^1(^{-\cdot}A—O^{\cdot}\cdots{}^+H—B)^*$. The proton in this configuration is located at the same nuclear configuration as in the ground state, by application of the Frank–Condon approximation, but is transferred to the base.

This systematic blue shift with O—H bond weakening is also observed in the triplet absorption. Peaking at 630 nm in the free phenol, $^3(^{-\cdot}A—O^{\cdot}—H^+)^*$, this band is observed to shift to higher energy as the interaction with the proton is weakened, first through hydrogen bonding $^3(^{-\cdot}A—O^{\cdot}—H^+\cdots:B)^*$, 620 nm, then proton transfer to the base $^3(^{-\cdot}A—O^{\cdot}\cdots{}^+H—B)^*$, 570 nm, and ultimately with deprotonation to the anion $^3(^{-\cdot}A—O^{\cdot})^*$, 530 nm (Section I.C.2, *SI Appendix*). The transition energies of the ground and excited state absorptions for the different protonation states of the nitrophenyl-phenol chromophore are summarized schematically in Fig. 3.

Based on our band assignments, the transient spectra at early times suggest that there are two spectroscopically accessible states corresponding to the configurations $^1(^{-\cdot}A—O^{\cdot}—H^+\cdots:B)^*$ and $^1(^{-\cdot}A—O^{\cdot}\cdots{}^+H—B)^*$. They are illustrated in the energy-coordinate diagram shown in Fig. 2. While both states appear to be populated by 355 nm excitation (as evidenced by the presence of both S_b and S_c), 388 nm excitation seems to produce only the latter. The absence of the $^1(^{-\cdot}A—O^{\cdot}—H^+\cdots:B)^*$ absorption feature following 388 nm excitation suggests that, at the ground-state geometry, $^1(^{-\cdot}A—O^{\cdot}\cdots{}^+H—B)^*$ is lowest in energy, as depicted in the figure. It is interesting to note that similar ultrafast proton transfer has been observed in related measurements on the green fluorescent protein (GFP). In GFP ultrafast proton transfer was attributed to excitation to a second state underlying the electronic absorption band, but the nature of the transition was unclear (10).

In the *para*-nitrophenyl-phenol adduct, the two initial singlet states have distinctly different dynamical signatures. Photoexcitation to $^1(^{-\cdot}A—O^{\cdot}—H^+\cdots:B)^*$ results in delayed proton transfer following intersystem crossing to the triplet, $^3(^{-\cdot}A—O^{\cdot}—H^+\cdots:B)^*$. Excitation to the lower-energy surface at 388 nm gives rise to prompt appearance of protonated base—i.e., $(^{-\cdot}A—O^{\cdot}\cdots{}^+H—B)^*$ in both the singlet and triplet spectra.

The presence of $(^{-\cdot}A—O^{\cdot}\cdots{}^+H—B)^*$ at the earliest observable pump-probe delay times (200 fs) is consistent with a photoinduced electron-proton transfer (photo-EPT) process. However, given the time scale of the experiment, we cannot rule out the presence of an ultrafast but delayed proton transfer process that occurs during the 200 fs excitation pulse solely from the transient absorption data. The key question is whether direct photoexcitation to the ICT-EPT state occurs from the ground-state configuration.

Coherent Raman measurements provide a direct probe of excited state vibrational modes at the Franck–Condon geometry. Similar to spontaneous resonance Raman spectroscopy, the amplitudes of the vibrational resonances reflect geometric distortions between the ground and excited states (i.e., Franck–Condon factors). However, application of a broadband field initiates nuclear motion on both the ground and excited state surfaces.

Details involved in the acquisition and analysis of the Raman signals are provided in the *SI Appendix*. A typical coherent Raman spectrum obtained from the *para*-nitrophenyl-phenol adduct is shown in Fig. 4. In this representation, the spectra contain positive and negative going signals, which are described for a general system by Eq. **S8** in the *SI Appendix*. For the systems discussed here, the signals with positive signs correspond to nuclear coherences in the ground electronic state, while the negative going signals are associated with nuclear coherences in the excited electronic state.

The spectrum of the nitrophenyl-phenol adduct shows the ν(O—H) ground-state band at 2,850 cm^{-1} and a band at 2,970 cm^{-1} that is assigned to an excited state vibrational coher-

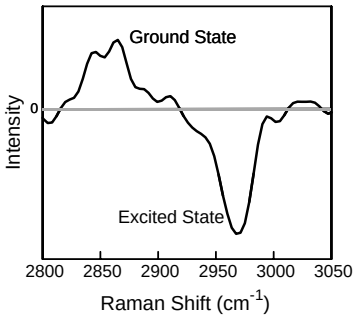

Fig. 4. Coherent Raman spectrum of the nitrophenyl-phenol/t-butylamine hydrogen-bonded adduct. The positive going feature is the Raman response of the O—H mode in the ground electronic state. The higher frequency negative going feature is an excited state vibrational resonance assigned to the $^{+}$H—N mode.

ence based on the sign of the signal. ICT excitation of the *para*-nitrophenyl-phenol weakens the O—H bond and shifts its vibrational frequency to lower energy, suggesting that the O—H mode is not the origin of the excited state resonance. Based on the shift to higher energy, the new band is assigned to the ν(N—H^{+}) mode in the ICT adduct. The 2,970 cm^{-1} frequency is consistent with ν(N—H^{+}) stretching vibrations observed in protonated amines (14), which range from 3,100 to 3,300 cm^{-1}.

From a Frank–Condon perspective, excitation to the ICT-EPT state is a vertical process along the coupled nuclear coordinates including the proton transfer coordinate. The formation of the protonated base in the optical excitation process is remarkable because it implies that there is redistribution of electron density both in the phenol and at the base. The rearrangement of electron density in intramolecular examples is expected because both the proton donor and acceptor are part of the same electronic framework. The electronic redistribution at the base in the intermolecular adduct is noteworthy, pointing to extensive electronic coupling across the hydrogen bond.

Hydroxy-Coumarin. ICT excitation of 7-hydroxy-4-(tri-fluoromethyl)-coumarin (HFC) promotes a largely nonbonding electron from the hydroxyl group to a π^{*} orbital with considerable carbonyl character, increasing the acidity of the OH proton by approximately 14 pK*a* units (7, 8). Evidence of ground-state H-bonding between the coumarin and 1-methyl-imidazole (1-MeIm) base in toluene is observed as a shift in the ICT absorption spectrum from 330 nm to 342 nm upon adduct formation. For 1-methylimidazole, $K_A = 2{,}100$ M^{-1} with adduct formation of 73% at 2 mM base concentration.

We have used the emissive properties of the coumarin to probe coupled electron-proton transfer following ultrafast excitation. In the absence of an external base, hydroxy-coumarins emit weakly with an emission maximum in toluene of 403 nm. The deprotonated form is strongly emissive with $\lambda_{max} = 506$ nm. Intense emission is also observed upon the addition of hydrogen-bonding bases, and the 1:1 adduct with 1-MeIm (A—O—H···:B) emits at 459 nm (15). The blue-shifted emission in the adduct relative to the anion can be attributed to H-bond stabilization of the ground-state anion by complex formation with the protonated base.

The appearance of the emission at 459 nm is thus an indicator of proton transfer in the excited state. Femtosecond transient absorption methods were used to monitor the growth of stimulated emission at 459 nm (Fig. 5*A*). Based on this result, approximately 75% of the emission appears on a time scale short relative to the instrument response time (<1 ps) consistent with rapid proton transfer.

The coherent Raman spectrum for the coumarin adduct is shown in Fig. 5*B*. Like *para*-nitrophenyl-phenol, the ν(O—H)

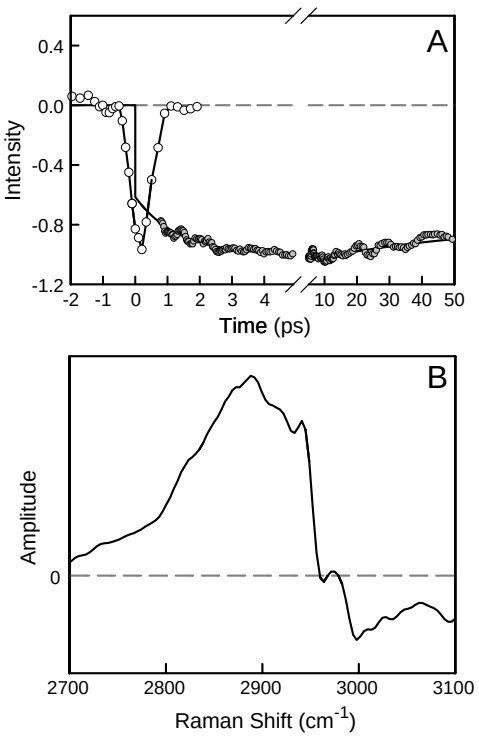

Fig. 5. (*A*) Transient stimulated emission data for the hydroxyl-coumarin 1:1 adduct with 1-MeIm (2 mM) in toluene following 355 nm excitation. The open circles display the laser excitation pulse reacting with the solvent nuclear response in toluene. Gray points represent the stimulated emission data at 465 nm; only data points outside the instrument response are shown. (*B*) Coherent Raman spectrum of the hydroxyl coumarin 1:1 adduct with 1-MeIm (2 mM) in toluene.

Raman response of the ground state is observed at 2,900 cm^{-1}, whereas an excited state vibrational resonance is observed near 3,050 cm^{-1}. Based on the shift to higher energy, the new band can be assigned to ν(N—H^{+}) in the ICT adduct ^{1}($^{-\cdot}$A—O$^{\cdot}$···$^{+}$H—B)*.

Conclusions

Our spectroscopic results reveal the presence of a concerted electron-proton transfer process in the optical ICT excitation of two different hydrogen-bonded dyes. Transient absorption spectra reveal that two spectroscopic states are accessed having different dynamical signatures. One of the states corresponds to a conventional excited state proton transfer process in which proton transfer occurs after vibrational and solvent relaxation. The other is an ultrafast concerted electron-proton transfer event with proton transfer coupled to the change in electronic configuration. The appearance of the ν(N—H^{+}) mode in the coherent Raman spectra shows that the proton transfer state is directly accessible via optical excitation. Here charge transfer occurs in concert with proton transfer to the nitrogen atom of the acceptor base with the newly formed H—N bond highly elongated along the H—N axis, ($^{-\cdot}$A—O$^{\cdot}$···$^{+}$H—B)*, as illustrated in Fig. 2. The evidence points to concerted transitions in both cases in which a proton transfer state is formed directly from the ground state during the ICT excitation.

Experimental Methods

A brief description of the materials and experimental methods are provided below and more detail can be found in the *SI Appendix*.

Materials. 4-hydroxy-4′-nitrobiphenyl (nitrophenyl-phenol) was purchased from TCI America and used as received. 7-hydroxy-

4-(trifluoromethyl)-1-coumarin (coumarin) (98%), and 1-methylimidazole (1-MeId) (99%) were purchased from Sigma-Aldrich and used as received. All solvents were purchased from Aldrich and used as received. All experiments on *para*-nitrophenyl-phenol were performed in dichloro-ethane (DCE). All experiments on the coumarin dye were performed in toluene.

Femtosecond Transient Absorption. Femtosecond transient absorption measurements were done using a pump-probe technique based on a Ti:Sapphire chirped pulse amplification (CPA) laser system (Clark-MXR CPA-2001). The pump pulse was produced by an Optical Parametric Amplifier (OPA) and the probe pulse was generated by continuum generation in a CaF_2 substrate and detected by a CCD camera. The spectrometer is capable of measuring transient spectra with approximately 200 fs time resolution and a sensitivity of better than 1 mOD.

Nanosecond Transient Absorption. The nanosecond transient absorption spectrometer is based on a Nd:YAG/OPO laser system used for sample excitation. The transient changes in a white-light continuum generated by Xe arc lamp were detected by a monochromator/PMT system and monitored using a digital oscilloscope.

Coherent Raman Spectrometer. The coherent Raman experiments apply two narrowband pulses and two broadband pulses with independently controlled delays; one broadband pulse is used for signal detection by spectral interferometry. The narrowband pulses are 500 fs in duration with spectra centered at 400 nm. The 355 nm broadband pulses have durations of 45 fs. The pulses are focused to 120 um FWHM spot size at the sample and possess energies of 50–100 nJ. Signals are detected using a back-illuminated CCD array (Princeton Instruments PIXIS 100B) mounted on a 0.3 m spectrograph.

ACKNOWLEDGMENTS. Support by National Science Foundation Grants CHE0957215 (T.J.M.), CHE0809530 (M.D.E.F.), and CHE0809045 (J.M.P.) is gratefully acknowledged. In addition, support for S.A.M., and support for B.C.W and M.K.B during the latter stages of the project, was provided as part of University of North Carolina Solar Fuels and Next Generation Photovoltaics, an Energy Frontier Research Center funded by the US Department of Energy, Office of Science, Office of Basic Energy Sciences under Award DE-SC0001011.

1. Huynh M, Meyer T (2007) Proton-coupled electron transfer. *Chem Rev* 5004–5064.
2. Gagliardi CJ, et al. (2010) Integrating proton coupled electron transfer (PCET) and excited states. *Coord Chem Rev* 254:2459–2471.
3. Hammes-Schiffer S, Iordanova N (2004) Theoretical studies of proton-coupled electron transfer reactions. *Biochim Biophys Acta* 1655:29–36.
4. Hammes-Schiffer S (2009) Theory of proton-coupled electron transfer in energy conversion processes. *Acc Chem Res* 42:1881–1889.
5. Meyer T, Huynh M, Thorp H (2007) The possible role of proton-coupled electron transfer (PCET) in water oxidation by photosystem II. *Angew Chem Int Ed Engl* 46:5284–5304.
6. Chang CJ, Chang MCY, Damrauer NH, Nocera DG (2004) Proton-coupled electron transfer: A unifying mechanism for biological charge transport, amino acid radical initiation and propagation, and bond making/breaking reactions of water and oxygen. *Biochim Biophys Acta* 1655:13–28.
7. Cohen B, Huppert D (2001) Evidence for a continuous transition from nonadiabatic to adiabatic proton transfer dynamics in protic liquids. *J Phys Chem A* 105:2980–2988.
8. Cohen B, Huppert D (2001) Excited state proton-transfer reactions of coumarin 4 in protic solvents. *J Phys Chem A* 105:7157–7164.
9. Tolbert L, Solntsev K (2002) Excited-state proton transfer: From constrained systems to "super" photoacids to superfast proton transfer. *Acc Chem Res* 35:19–27.
10. Shi X, et al. (2007) Ultrafast excited-state dynamics in the green fluorescent protein variant S65T/H148D. 2. Unusual photophysical properties. *Biochemistry* 46:12014–12025.
11. Shu X, et al. (2007) Ultrafast excited-state dynamics in the green fluorescent protein variant S65T/H148D. 1. Mutagenesis and structural studies. *Biochemistry* 46:12005–12013.
12. Leiderman P, et al. (2007) Ultrafast excited-state dynamics in the green fluorescent protein variant S65T/H148D. 3. Short- and long-time dynamics of the excited-state proton transfer. *Biochemistry* 46:12026–12036.
13. Yip R, Sharma D, Giasson R, Gravel D (1984) Picosecond excited-state absorption of alkyl nitrobenzenes in solution. *J Phys Chem* 88:5770–5772.
14. Socrates G (2001) *Infrared and Raman Characteristic Group Frequencies* (Wiley, New York), 3rd Ed.
15. Shank CV, Dienes A, Trozzolo AM, Myer JA (1970) Near UV to yellow tunable laser emission from an organic dye. *Appl Phys Lett* 16:405–407.

Supporting Information - Concerted Electron-Proton Transfer in the Optical Excitation of Hydrogen Bonded Dyes

Brittany C. Westlake, M. Kyle Brennaman, Javier J. Concepcion, Jared J. Paul, Stephanie E. Bettis, Shaun D. Hampton, Stephen A. Miller, Natalia V. Lebedeva, Malcolm D. E. Forbes, Andrew M. Moran, Thomas J. Meyer and John M. Papanikolas**

I. NITROPHENYL-PHENOL/T-BUTYL AMINE

A. Materials and Methods

Materials: 4-hydroxy-4'-nitrobiphenyl (nitrophenyl-phenol) was purchased from TCI America and used as received. 1,2-dichloroethane (> 99.8 %), toluene (> 99.9 %), butyronitrile (99 %), dichloro-methane (99.6 %), tetrahydrofuran (> 99.9 %), tert-butylamine (≥ 99.8 %), 1-methylimidazole (99 %), diisopropylamine (99.95 %), triethylamine (99 %), 4-(dimethylamino)pyridine (99 %) were purchased from Aldrich and used as received. Acetonitrile (99.8 %) was purchased from Aldrich and dried over molecular sieves (4 Å, 8-12 mesh purchased from Acros) to reduce the amount of water present. Pyridine (99.9 %) was purchased from Fisher and used as received. All experiments, unless otherwise noted, were performed in dichloro-ethane (DCE).

Femtosecond Transient Absorption. Femtosecond transient absorption measurements were done using a pump probe technique which has been described previously in detail.[1-5] Briefly, the excitation source was a Clark 2001 chirped pulse amplification (CPA) laser system which outputs a 800 mW, 775 nm, pulse at a 1 kHz rep rate, with an autocorrelation full width half max of 250 fs. The probe pulse was generated by focusing a small portion of the beam into a CaF_2 window to generate a white light continuum from 380-700 nm. The spot size at the sample was ~ 280 micron. The 388 nm pump pulse was created by second harmonic generation of the 775 nm beam by a beta barium borate (BBO) crystal. The 355 nm pump pulse was created with a tunable Clark Optical Parametric Amplifier (OPA) (1420 nm) and subsequent second (710 nm) and fourth (355 nm) harmonic generation. The data was collected at magic angle polarization (54.7 degrees) with pump beam focused to ~1400 micron spot size and power of 0.60 mW. Samples with concentrations of 0.3 mM nitrophenyl-phenol with (90 mM) or without tert-butylamine base were prepared. Samples were placed in a 2 mm quartz cuvette and degassed with Ar gas for 30 mins prior to data collection. The Argon gas was first bubbled through neat solvent before passing through the sample solution such that solvent evaporation from the sample was minimized. The chirp in the white light was accounted for using an optical gating technique described earlier.[1]

Nanosecond Transient Absorption. Transient absorption experiments on the nanosecond time scales were performed with instrumentation described previously.[6] In brief, samples were prepared in a 2 mm pathlength quartz cuvette to maintain consistent concentrations with experiments performed using the femtosecond TA apparatus. All samples were argon degassed for at least 30 minutes just prior to performing experiments. The third harmonic of a Continuum Surelite II-10 Nd:YAG laser system (355 nm, 5-7 ns, 1 Hz, 0.4 mJ/pulse) served as an excitation source. Because the white light probe pulses generated by a 150 W pulsed lamp were passed through the sample at 90° relative to excitation, the 2mm cuvette was placed 45° relative to pump and probe. The probe was collected by an Applied Photophysics laser kinetic spectrometer consisting of an f3.4 monochromator and Hamamatsu R928 PMT. Given the small pathlength of the cuvette, the cuvette was oriented at 45° relative to both pump and probe pulses. The output from the PMT is sent to a LeCroy WavePro 7100A oscilloscope interfaced to a PC. Electronic synchronization and control of the experiment are achieved by electronics and software of local design. Kinetic traces, (average of 100) decaying to (at least) >5 lifetimes of the transient observed, were acquired and averaged at each wavelength. Quantitative analysis of the average decay curves was done using the algorithms of SigmaPlot (Systat Software, Inc.). Transient absorption probed anywhere between 300 nm and 800 nm was measured with a sensitivity of 1 mOD.

B. UV-VIS Absorption Spectra

UV-Visible absorption spectra of nitrophenyl-phenol, nitrophenyl-phenol with base, and nitrophenyl-phenol anion in dicholorethane (DCE) are shown in Figure S1. Nitrophenyl-phenol in DCE has an absorption (λ_{max} = 335 nm) arising from an intramolecular charge transfer from the phenolic oxygen to the nitro group. Upon addition of excess *tert*-butylamine, the absorption maximum shifts to lower energy (λ_{max} = 354 nm) as a result of H-bonding between nitrophenyl-phenol and base. The nitrophenyl-phenol anion

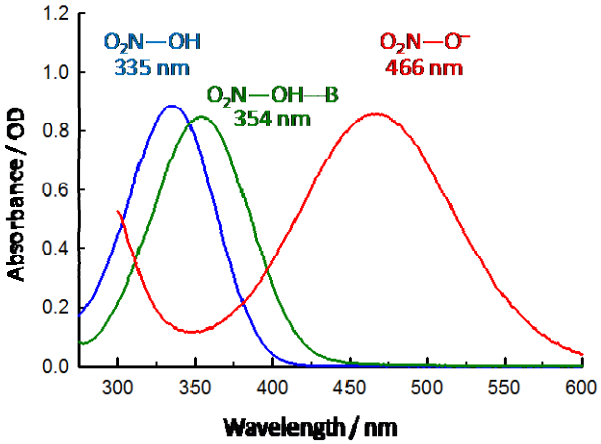

Figure S1: UV-Visible absorption spectra for nitrophenyl-phenol, nitrophenyl-phenol hydrogen bound to *tert*-butylamine, and the nitrophenyl-phenolate anion in 1,2-dichloroethane. Absorption maxima for each species are indicated above the spectra.

absorption is shifted even further to lower energy (λ_{max} = 466 nm) consistent with a higher energy ground state due to proton loss on the nitrophenyl-phenol.

C. Transient Absorption Spectroscopy

Figure S2 (also Figure 3 of the manuscript) shows results from fs-TA experiments performed on nitrophenyl-phenol hydrogen-bound to *tert*-butylamine in DCE. The uppermost panel shows the TA observed 1 ps after photoexcitation of the free nitrophenyl-phenol at 355 nm. The lower two panels of the figure depicts TA spectra obtained at 1 ps following 355 nm and 388 nm excitation of the hydrogen-bonded adduct. Each of the spectra exhibit a lower-energy band extending from 500 to 700 nm, and a higher energy band at centered at ≈ 400-450 nm. Based on experiments performed on the free nitrophenyl-phenol described in Section C.1, we assign these two features to absorptions from singlet (higher energy band) and triplet (lower-energy band) excited states.

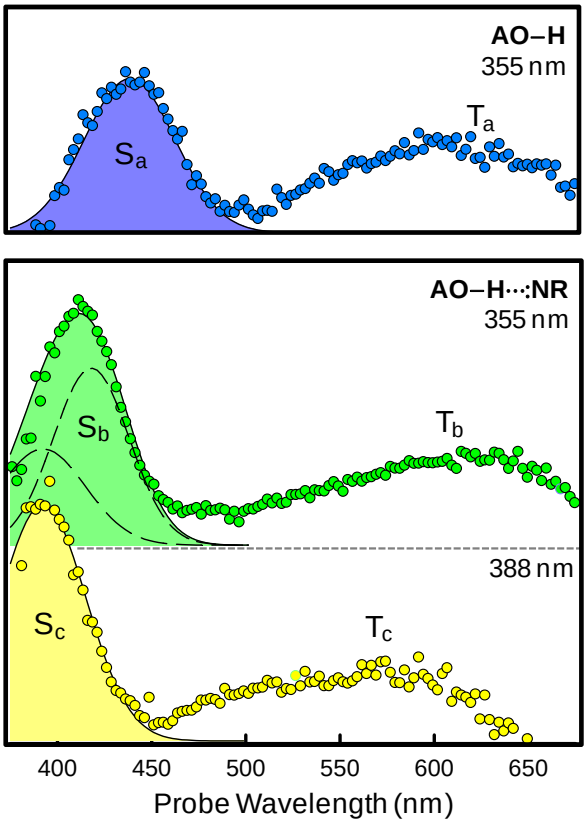

Figure S2: Transient absorption spectra observed at 1 ps after excitation for the free nitrophenyl-phenol (top panel) excited at 355 nm and the hydrogen bonded adduct (lower two panels) excited at 355 nm and 388 nm.

C.1: Nitrophenyl-phenol in DCE (355 nm Excitation): Delta absorbance spectra covering a 400 - 700 nm spectral window following photoexcitation near the maximum of the nitrophenyl-phenol absorption band at 355 nm are shown as a function of pump-probe delay in Figure S3. At our earliest observation time (250 fs), we observe two absorptions – a prominent band centered at 440 nm (Sa) and the beginnings of a broad absorption at 630 nm (Ta). During the first 10 ps, the 440 nm feature decays completely as the red band reaches a maximum in amplitude. The evolution of this band is followed on longer time scales using ns-TA spectroscopy; the TA spectrum observed at 10 ns is shown

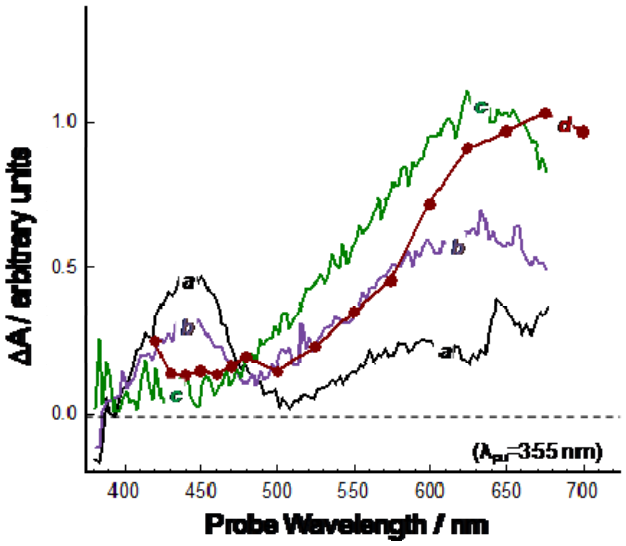

Figure S3: Transient absorption spectra for nitrophenyl-phenol in 1,2-dicholorethane (DCE) obtained at 1 ps (a), 3 ps (b), 20 ps (c) and 10 ns (d). The 450 nm band observed at early times converts into the 650 nm band with a time constant of 3 ps, which then decays with a 2.4 μs lifetime. The magnitude of the high energy band is typically in the range of 10-15 mOD for both fsTA and nsTA at early observation times.

superimposed on fs-TA data in the figure. The 630 nm band is observed to decay without a change in shape on a 2.5 μs timescale. This long lifetime and isosbestic behavior between the two absorptions suggests that (1) the 440 nm band initially observed arises from the optically prepared singlet excited state and (2) that the 630 nm band corresponds to absorption from a triplet excited state. The decay at 440 nm and concurrent growth at 650 nm reflect a rapid (3 ps) intersystem crossing (ISC) in nitrophenyl-phenol in DCE.

The presence of a long-lived triplet is confirmed by time-resolved EPR experiments (vide infra). Rapid formation of a triplet excited state, as well as red and blue bands in the transient absorption spectrum has been reported in previous studies involving alkyl substituted nitrobenzenes.[7]

C.2: Nitrophenyl-phenol with tert-butylamine in DCE:

Figure S2 depicts the transient spectra from the hydrogen-bonded adduct observed following 355 nm and 388 nm excitation. Both spectra are qualitatively similar to the two-band nitrophenyl-phenol spectrum discussed in Section C.1; however there are some differences. For example, while the low-energy band (T_b) resulting from 355 nm excitation has a position similar to that of T_a, the higher-energy feature appears blue-shifted with λ_{max}=410 nm. The spectrum observed following 388 nm excitation shows both absorption bands to be shifted to shorter wavelengths relative to their 355 nm counterparts, appearing at 395 nm (S_c) and 575 nm (T_c).

Figure S4 shows the TA signal as a function of pump probe delay at three different detection wavelengths (395 nm, 440 nm and 600 nm) for 355 nm excitation and at 395 nm for 388 nm excitation. There are several notable features about the pump-

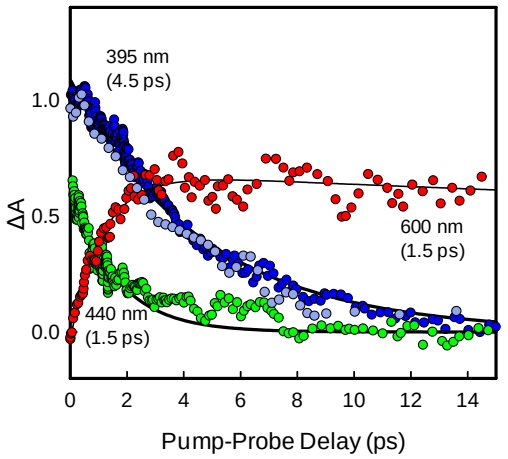

Figure S4: Kinetic data for the nitrophenyl-phenol/tert-butylamine adduct in DCE. Blue points represent the decay in the transient absorption signal at 395 nm; green points show the decay of the low energy side at 440 nm. Non-linear least squares analysis reveals time constants of 4.5 ps and 1.5 ps for the 395 nm and 440 nm decays, respectively. The red points show the kinetic growth of the 600 nm absorption band, which appears with a 1.5 ps time constant. All transients except light blue correspond to 355 nm excitation; light blue corresponds to 388 nm excitation. The similarity between the time scales for the decay of the low-energy side and the growth of the red absorption band indicate that they correspond to the same dynamical process, namely singlet-triplet inter-conversion. The magnitude of the high energy band is typically in the range of 10-15 mOD for the fsTA measurements at early delays.

probe kinetics. (1) The high- and low-energy sides of the blue absorption band observed following 355 nm excitation decay with different rates, with the higher energy side (395 nm) decaying more slowly than the low-energy side. (2) With 355 nm excitation, the decay at 440 nm is concurrent with the growth at 600 nm ($\tau \sim 1.5$ ps), indicating that the appearance of the triplet population is correlated with the loss of the *low-energy side* of this band. And (3), the transients observed at 395 nm show identical decay kinetics for both the 355 nm and 388 nm excitation wavelengths. Note that, unlike the singlet band observed at 355 nm excitation, at 388 nm this band decays without a change in shape or spectral position, i.e. all probe wavelengths throughout this band exhibit identical kinetics.

The first two observations indicate that the singlet absorption band in the 355 nm spectrum is actually composed of two overlapping bands. Because these two absorptions are not resolved in the 355 nm spectrum, deconvolution based on this spectrum alone is impossible. However, recognizing that the high-energy side of that band decays with the same kinetics as the singlet absorption in the 388 nm spectrum, we are led to conclude that one of these two unresolved absorptions in the 355 nm spectrum resembles the band labeled S_c in the 388 nm spectrum, Figure S2. Taking the higher-energy feature to have the same position and width as S_c (λ_{max}=395 nm), enables us to then determine the location of the lower-energy feature (S_b, λ_{max}=420 nm) in the 355 nm spectrum. These two components are depicted as the dashed lines in Figure S2.

The physical process corresponding to the decay of S_c at 395 nm is at the moment unclear. Although, unlike S_b, the decay of S_c at 395 nm does not appear to be correlated with a growth in the triplet band observed following 388 nm excitation, suggesting it is not due to intersystem crossing. While it may simply be relaxation to the ground state, following the dynamics of the bleach is difficult due to scatter from the pump pulse at the same wavelength.

In contrast to the free nitrophenyl phenol, the triplet absorption of the hydrogen-bonded adduct at 355 nm shows complex evolution (Figure S5), exhibiting a time-dependent blue shift from its initial position of 620 nm to ~530 nm at 10 ns after excitation. The blue shift occurs in a biphasic manner with an initial fast shift ($\tau \sim$ 5-20 ps) followed by a slower shift ($\tau \sim$ 100's ps). Between 10 ns and 40 ns this band decays and is replaced by the growth of a new band at 460 nm, with a clear isosbestic point. The 460 nm band then decays with second order equal concentration kinetics on a single microsecond timescale.

Spectral Assignments: Our assignments for both the singlet and triplet absorptions are summarized in Figure 3 of the manuscript.

We assign the final absorption band at 460 nm in the triplet evolution to ground state absorption from the deprotonated nitrophenyl phenol anion, ($A–O^- + {}^+H–B$), which implies that the 530 nm band (denoted T_d) originates from its triplet excited state, ${}^3(^{-\cdot}A–O^{\cdot} + {}^+H–B)^*$. Since the absorption at early times (620 nm, T_b) likely corresponds to the triplet absorption of the hydrogen bonded adduct, ${}^3(^{-\cdot}A–O^{\cdot}–H^+\cdots:B)^*$, the systematic shift from 620 nm to 530 nm is assigned to the continual weakening of the OH bond from the hydrogen-bonded form, ${}^3(^{-\cdot}A–O^{\cdot}–H^+\cdots:B)^*$, T_b, through proton transfer to the base, ${}^3(^{-\cdot}A–O^{\cdot}\cdots{}^+H–B)^*$, which is denoted by T_c, and ultimately deprotonation,

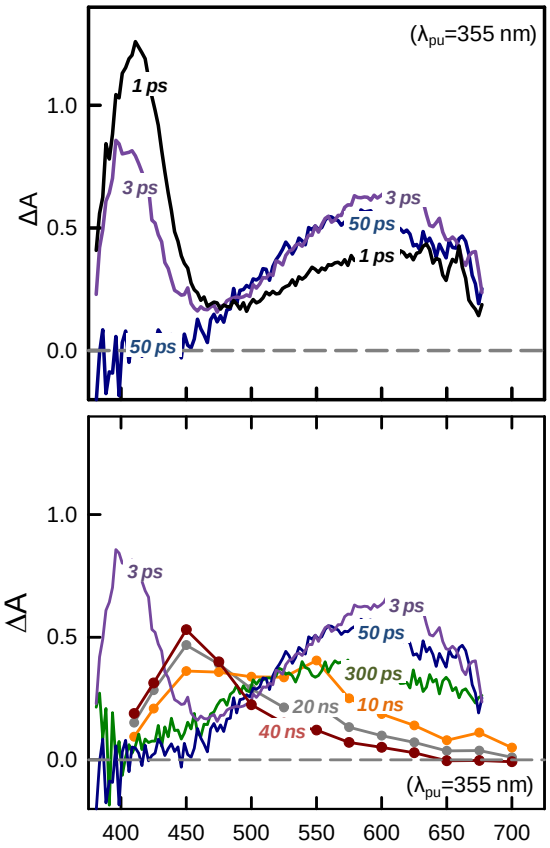

Figure S5: Transient absorption spectra for nitrophenyl-phenol hydrogen bonded adduct in 1,2-dicholorethane (DCE). Top panel shows spectra obtained at early time (1-50 ps) and lower panel shows spectra from 3 ps-40 ns. The magnitude of the high energy band is typically in the range of 10-15 mOD for both fsTA and nsTA at early observation times.

$^3(^{-\cdot}A–O^{\cdot} + {}^{+}H–B)^*$, T_d. Our data thus indicate that, like the ground state absorption, the triplet excited state absorption is sensitive to the position of the proton.

The time-dependent spectral shift reflects the proton first shifting to the base ($\tau \sim$ 5-20 ps) while still hydrogen bound to the nitrophenyl-phenol, followed by the dissociation of the hydrogen-bonded adduct ($\tau \sim$ 100's ps) to create a triplet nitrophenyl-phenol radical anion and a protonated base complex. The decay of the 550 nm band reflects relaxation of the triplet species to its ground state (450 nm band), which in turn decays as the anion and protonated base complex recombine on a microsecond time scale.

While the correlation between decay at 420 nm and corresponding growth at 600 nm, indicates that the S_b feature be assigned to absorption from the singlet ICT state in the hydrogen-bonded adduct, i.e. $^1(^{-\cdot}A–O^{\cdot}–H^{+}\cdots B)^*$, the question arises as to the origin of the higher energy band at 395 nm (S_c). The shift of the triplet band to higher energy with OH bond weakening, as well as, the blue shift of the singlet band upon hydrogen bonding (S_a vs S_b), suggest that the 395 nm band arises from absorption from the singlet ICT state in which the proton has transferred to the base, i.e. $^1(^{-\cdot}A–O^{\cdot}\cdots H^{+}–B)^*$. The implications of this assignment are central to the discussion presented in the manuscript.

D. Time-Resolved EPR Spectroscopy

Continuous wave time-resolved electron paramagnetic resonance (TREPR) experiments were performed as previously described.[8] Briefly, all experiments were performed on a JEOL USA Inc. JES-RE1X X-band (9.5 GHz) EPR spectrometer equipped with a wide bandwidth preamplifier and a low-noise GaAs FET microwave amplifier. A sample of nitrophenyl-phenol dissolved in toluene (10 mM) was placed in a cylindrical quartz EPR tube (4 mm OD). The sample tube was fitted with a vacuum line adapter and subjected to 5 consecutive freeze-pump-thaw cycles. The sample was then placed in a liquid N_2 dewar insert positioned in the center of a Varian TE_{103} optical transmission cavity. After the temperature inside the insert had equilibrated to 120 K by flowing regulated cold N_2 gas, the frozen samples were photolyzed using a Lambda Physik LPX 100i excimer laser (308 nm, XeCl) running at 60 Hz with a pulse energy of 100 mJ (~ 20 mJ per pulse hitting the sample) and a pulse width, accounting for jitter, of 25 ns. Spectra were collected in the absence of field modulation at a fixed delay time after the laser flash using a two-gate boxcar integrator (Stanford, 100 ns gates), while the external magnetic field was swept, typically over 4 minutes.

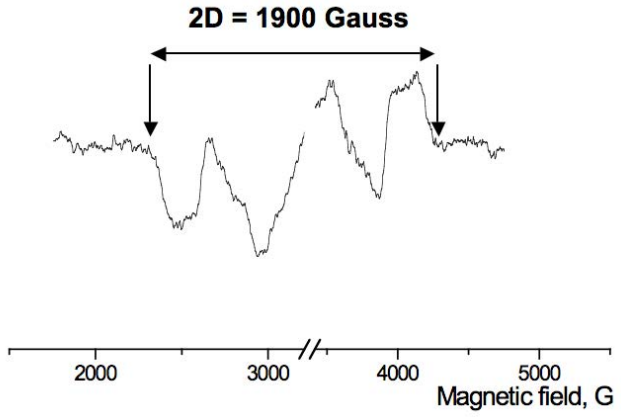

Figure S6: TREPR spectrum of nitrophenyl-phenol triplet in toluene glass at 120 K, aquired 500 ns after 308 nm excitation (35 ns pulse). The TREPR spectrum is spin–polarized EAEAEA (E = emission, A = absorption) as predicted from CIDEP theory. The measured zero field splitting D of 950 Gauss (1/2 the spectral width) is typical for n,π* states of aromatic phenols.

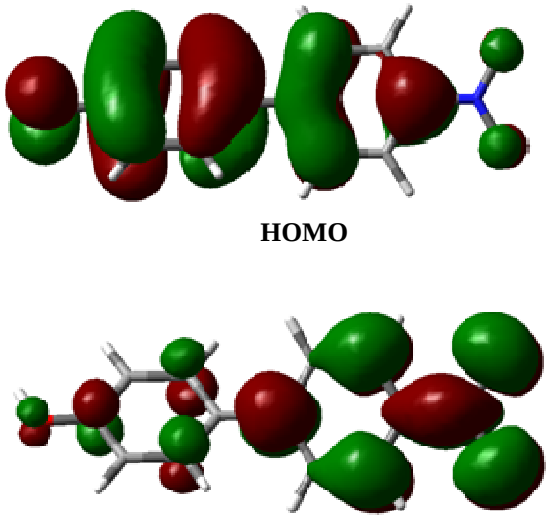

Figure S7: Molecular orbitals involved in the lowest energy transition for para nitrophenyl phenol, A–O–H.

E. Theoretical Calculations.

Theoretical calculations were carried out by using Density Functional Theory (DFT) as implemented in Gaussian03, revision D.02. Becke's three-parameter hybrid functional[9-11] with the LYP correlation functional[12] (B3LYP) was used with the 6-31g split-valence basis set. Franck-Condon vertical excitation energies and oscillator strengths were obtained with non-equilibrium Time-Dependent Density Functional Theory (TD-DFT)[13-15] as implemented in Gaussian03. The solvent (1,2--dichloroethane) was modeled by means of the Integral Equation Formalism Polarizable Continuum Model (IEF-PCM),[16-18] as implemented in Gaussian03. The geometries of the free nitrophenyl phenol (A–O–H), its hydrogen-bonded adduct (A–O–H···:B), and the deprotonated anion ($A–O^{-}$) were fully optimized (B3LYP, 6-31g, gas phase). Similarly, the geometry of ($A–O^{-}\cdots{}^{+}H–B$) was optimized but keeping the O-H distance fixed at 1.621 Å. This distance was selected from a full optimization using water as the solvent (IEF-PCM). The intense lowest energy transition in each case corresponds to the ICT band and therefore determines the energy of the ICT excited state above the ground state for each particular species. Figure S7 shows isodensity surfaces for the two orbitals involved in the lowest energy transition for A–O–H (HOMO and LUMO).

DFT calculations also reveal that the inter-ring torsional angle decreases from 34.5° in A–O–H to 26.6° in $A–O^{-}\cdots{}^{+}H–B$ to 12.6° in the anion ($A–O^{-}$). This is consistent with enhanced electronic delocalization between the aromatic rings, further supporting an

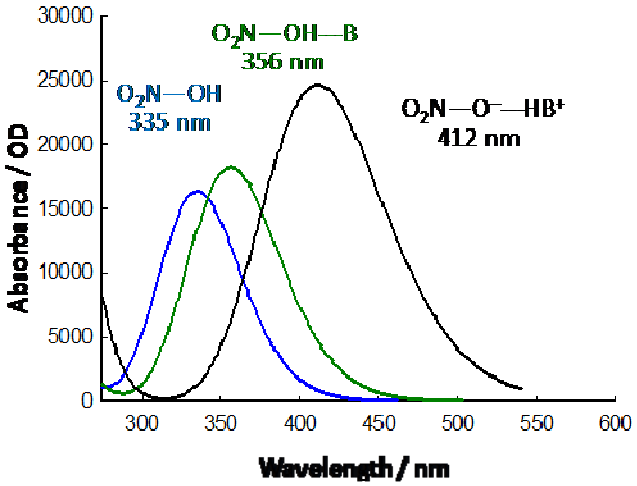

Figure S8: Calculated absorption spectra for A–O–H, A–O–H···:B and A–O$^-$···$^+$H–B in 1,2-dichloroethane. The peak half-width at half-height (HWHH) was chosen as 2685.83 cm^{-1} in all cases.

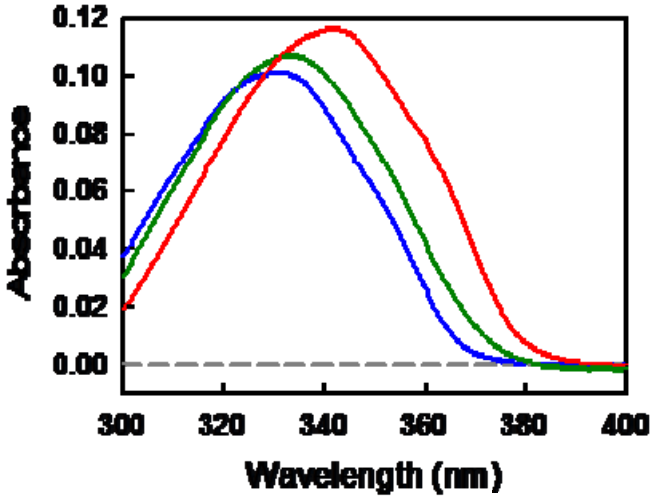

Figure S9. UV-Vis absorption measurements for 0.34 mM coumarin with 0 mM (blue line), 0.01 mM (green line), and 0.1 mM (red line) 1 MeId in toluene.

excited state twisting mechanism that facilitates ISC.[19] Figure S8 shows the calculated absorption spectra for A–O–H, A–O–H···:B and A–O$^-$···$^+$H–B. The spectra have been corrected by adding 7389 cm^{-1} to match the absorption maximum for the lowest energy absorption for A–O–H in 1,2-dichloroethane (335 nm). The calculated spectra for A–O–H···:B and A–O$^-$···$^+$H–B have absorption maxima at λ_{max} = 356 nm and λ_{max} = 412 nm, respectively.

II. HYDROXY COUMARIN/METHYL IMIDAZOLE

A. Materials

7-hydroxy-4-(trifluoromethyl)-1-coumarin (coumarin) (98%), 1-methylimidazole (1-MeId) (99%), and toluene (Chromasolv Plus for HPLC, >99.9%) were all purchased from Sigma-Aldrich and used as received. Solutions for femtosecond transient absorption experiments were prepared with 0.34 mM coumarin and 2 mM 1-MeIm base in toluene. Solutions for UV-Vis and steady state emission measurements were made at a range of base concentrations. Prior to time resolved emission measurements, the samples were deaerated by bubbling Argon gas through the sample for ~30 minutes. The Argon gas was first bubbled through neat solvent before passing through the sample solution such that solvent evaporation from the sample was minimized.

B. Ground State Absorption Spectroscopy

UV-Vis absorption measurements were done using an Agilent Technologies Model 8453 diode-array spectrophotometer. Initial absorption measurements were done in a 1 cm cuvette and then repeated in a 2 mm cuvette to recreate the path length and concentration conditions used in the femtosecond transient absorption measurements.

Ground state absorption spectra are shown in Figure S9. The intramolecular charge transfer (ICT) absorption band of coumarin in toluene absorbs at λ_{max} = 330 nm. With the addition of 1-MeId base, the absorption maximum shifts to λ_{max} = 342 nm. This red shift is evidence of hydrogen bonding in the ground state between coumarin and 1-MeId.

C. Steady State Emission Spectroscopy

Steady state emission measurements were taken using a PTI QuantaMaster 4SE-NIR Emission Spectrometer. Samples were excited at 355 nm with sample emission detected from 360 nm to 700 nm using background correction. Emission collected using the 2 mm cuvette required it be placed 45° relative to both the excitation light and emission slits in the spectrometer. Slit widths were set to achieve 1.4nm bandwidth.

Room temperature steady state emission measurements show coumarin's base concentration dependent emission, Figure S10. Without base in toluene solvent, coumarin is very weakly

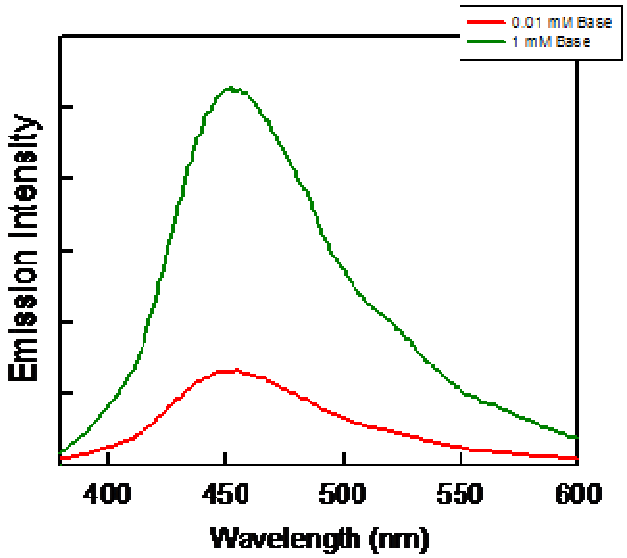

Figure S10. Room temperature steady state emission data for 0.34 mM coumarin with 0.01 mM and 1 mM 1-MeId in toluene. Samples were excited at 355 nm.

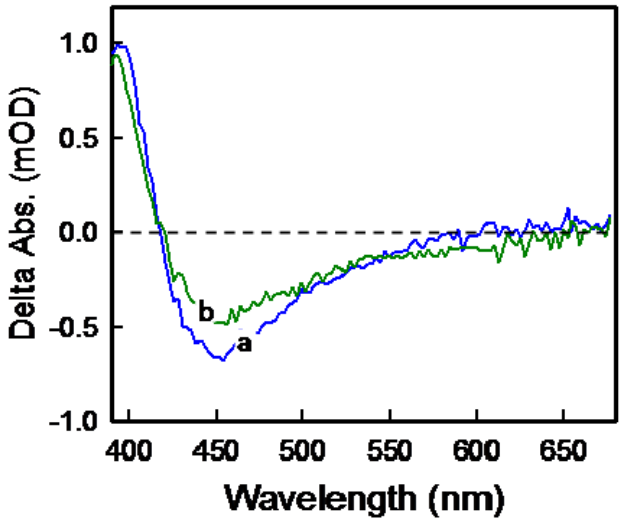

Figure S11. Femtosecond Spectra. A) Transient absorption difference spectra for coumarin with low base concentration (4 mM) or the 1:1 adduct, following 355 nm excitation obtained at 10 ps (a) and 600 ps (b).

emissive at 406 nm. Upon addition of small amounts of base, a blue emission band at 460 nm appears and grows in intensity with increasing base concentration. From this data and studies in the literature[20], we assign the blue 460 nm emission band to the coumarin anion still hydrogen bonded to the protonated base.

D. Femtosecond Transient Absorption:

Femtosecond transient absorption measurements were done using a pump probe technique which has been described previously in detail.[1-5] Briefly, the excitation source is a chirped pulse Ti:Sapphire regenative amplification laser system (Clark CPA 2001) which outputs a 800 mW, 775 nm pulse at a 1 kHz rep rate, with an autocorrelation full width half max of 250 fs. The probe pulse was generated by focusing a small portion of the beam into a CaF_2 window to generate a white light continuum from 380-700 nm. The spot size at the sample was ~ 280 μm. The 355 nm pump pulse was created with a tunable Clark Optical Parametric Amplifier (OPA) (1420 nm) followed by second harmonic generation (710 nm) and fourth (355 nm) harmonic generation by focusing the respective beams through beta barium borate (BBO) crystals. The data was collected at magic angle polarization (54.7 degrees) with pump beam focused to ~ 1400 μm spot size and power of 0.60 mW. Samples with concentrations of 0.34 mM coumarin with 2 mM 1-MeId base were prepared. Samples were placed in a 2 mm quartz cuvette and degassed with Ar gas for 30 minutes prior to data collection. The chirp in the white light was accounted for using an optical gating technique described elsewhere.

Further studies of the proton transfer properties of coumarin were studied utilizing ultrafast transient absorbance techniques. Experiments were done on 0.34 mM coumarin with 2 mM 1-MeId in toluene. Immediately within our earliest instrument capabilities (~ 1 ps), a bleach appears at 460 nm, Figure S11. This bleach corresponds to stimulated emission of the anion with the blue shift due to a ground state stabilization from the H-bond interaction with the base. This band provides evidence of a hydrogen-bound emissive state. Figure 1A of the communication shows the transient at 460 nm overlaid with the signal of the toluene solvent nuclear response to the excitation laser pulse. Over the next hundreds of picoseconds the band begins to decay, but does not completely decay within our instruments time scale.

III. COHERENT RAMAN

This section summarizes the experimental details and signal generation mechanisms associated with the coherent Raman measurements. The experiment is essentially a vibrational analogue of the electronic spectroscopy presented in a previous publication,[21] where we describe how control over arrival times of the three applied fields can be used to isolate the Raman response. For example, Figure S12, demonstrates the suppression of undesired broadband signal components originating in improperly ordered field-matter interactions (e.g., pump-probe signals in absorptive sample). Below we present an analysis of all signal generation mechanisms to support the interpretation given in the main paper. The essential information is summarized by Equation (S8).

A. Experimental Details

The experiments are conducted with the interferometer described previously.[21] The two narrowband pulses are 500 fs in duration with spectra centered at 400 nm. The 355 nm broadband pulse has a duration of 45 fs. The pulses are focused to 120 um FWHM spot size at the sample and possess energies of 50-100 nJ. To suppress the Raman response of toluene, polarizations of the signal and broadband pulse are set orthogonal to those of the narrowband pulses (i.e., ZXZX tensor element). Signals are detected by spectral interferometry using a back-illuminated CCD array (Princeton Instruments PIXIS 100B) mounted on a 0.3 meter spectrograph. Integration times are 3 seconds. To eliminate contributions from scattered light, a mechanical shutter placed in the path of the broadband pulses to obtain differences in which the narrowband pulses are “on” and “off”. All spectra represent an average of 75 differences. Interferograms are processed using a Fourier transform algorithm. The real (absorptive) part of the signal field is defined

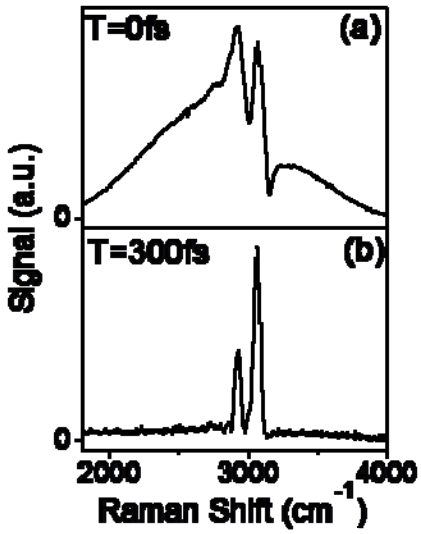

Figure S12. Measurements showing suppression of undesired signal components. Raman spectra of toluene measured with (a) T=0 fs and (b) T=300 fs. The measurement uses 550 nm, 210 fs narrowband pulses and a 650 nm, 20 fs broadband pulse. Proper field-matter interactions sequences are enforced when T is greater than the duration of the narrowband pulse.

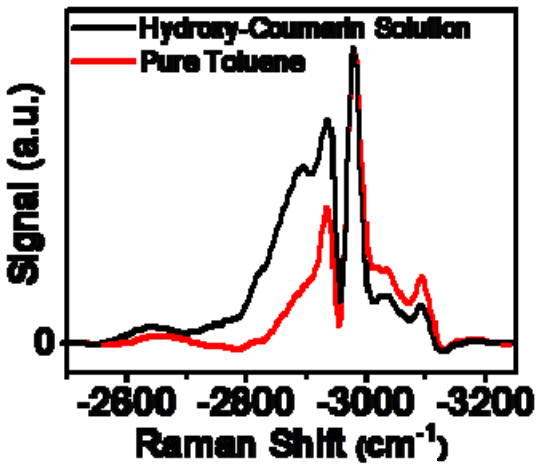

Figure S13. Real (absorptive) part of coherent Raman signal measured for (red) pure toluene and (black) a solution of coumarin in toluene. The difference in these two signals is displayed in Figure 5b in the main paper. The Raman shift is negative because the signal field frequency is larger than that of the narrowband pulse (i.e., detection is on anti-Stokes side of narrowband pulse).

using the vibrational resonances of toluene as a reference (i.e., an internal standard). The experiments were performed multiple times to confirm reproducibility of the results. Coherent Raman spectra measured with pure toluene and the coumarin/1-MeId solution are shown in Figure S13.

B. Nonlinear Response Function

The Raman response reflects an interference between two classes of terms. The R1, R2, R3, and R4 terms in Figure S14 radiate signal fields that are 180 degrees out-of-phase with R1* and R2*; spectra shown in the main paper use a convention in which R1* and R2* have negative signs. Figure S14 shows that the (third-order) nonlinear polarization consists of six signal components

$$P^{(3)}_{Total}(t) = P^{(3)}_{R1}(t) + P^{(3)}_{R2}(t) + P^{(3)}_{R3}(t) + P^{(3)}_{R4}(t) - P^{(3)}_{R1^*}(t) - P^{(3)}_{R2^*}(t) \quad \text{(S1)}$$

Following the approximations that lead to Equation (10) in Reference [21] it is readily shown that

$$P^{(3)}_{Total}(t) = \sum_{ab} \xi_{ab}(t)\Phi^{1}_{abcd} + \sum_{cd} \xi_{cd}(t)\left[\Phi^{2}_{abcd} - \Phi^{3}_{abcde}\right] \quad \text{(S2)}$$

$$\Phi^{1}_{abcd} = \left(\frac{i}{\hbar}\right)^3 \sum_{cd} \mu_{ac}\mu_{cb}\mu_{da}\mu_{bd}\left[P(a)\sigma_{ac}(-\omega_{NB}) + P(b)\sigma_{cb}(\omega_{BB})\right]\sigma_{db}(\omega_{BB}) \quad \text{(S3)}$$

$$\Phi^{2}_{abcd} = 2\left(\frac{i}{\hbar}\right)^3 \sum_{ab} P(a)\mu_{ca}\mu_{ad}\mu_{db}\mu_{bc}\left[\sigma_{ca}(\omega_{BB}) + \sigma_{ad}(-\omega_{NB})\right]\sigma_{cb}(\omega_{BB}) \quad \text{(S4)}$$

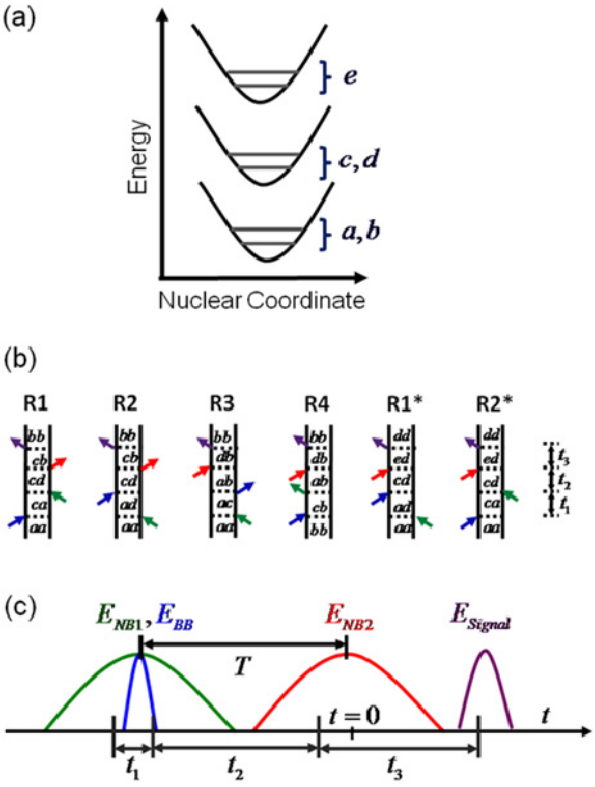

Figure S14. (a) Notation used in Equations (S1)-(S8). Three electronic states participate in the coherent Raman process. This notation assigns the dummy indices for vibronic states a and b to the ground electronic state; c and d to the excited electronic state with intermediate energy; e to the highest energy excited electronic state. (b) Feynman diagrams for the six classes of terms in the response function. (c) Pulse sequence in which NB denotes a narrowband (500 fs) pulse at 400 nm and BB represents a broadband (45 fs pulse at 355 nm). Color codes for the electric fields are consistent with panel (b). The experimentally controlled delay, T, is set equal to 700 fs. Time intervals between field-matter interactions are given by t1, t2, and t3.

$$\Phi^{3}_{abcde} = 2\left(\frac{i}{\hbar}\right)^3 \sum_{abe} P(a)\mu_{ad}\mu_{ca}\mu_{ec}\mu_{de}\left[\sigma_{ad}(-\omega_{NB}) + \sigma_{ca}(\omega_{BB})\right]\sigma_{ed}(\omega_{BB}) \quad \text{(S5)}$$

where

$$\sigma_{ab}(\omega) = \left(\frac{1}{i\omega - i\omega_{ab} - \Gamma_{ab}}\right) \quad \text{(S6)}$$

and

$$\xi_{ab}(t) = \theta(t+T)\exp\left[-i\omega_{ab}T - i(\omega_{NB} + \omega_{ab})t - \Gamma_{ab}(t+T) - \Lambda_{NB}|t|\right] \quad \text{(S7)}$$

Here, P(a) is the equilibrium population of state a, ω_{NB}, and ω_{BB} are carrier frequencies of the narrowband and broadband pulses, Γ_{ab} is a dephasing rate, and Λ_{NB} is the bandwidth of the narrowband pulse assuming a Lorentzian spectrum.

As shown in Reference [21] , the frequency domain representation of $P^{(3)}_{Total}(t)$ (i.e., Raman spectrum) is given by

$$\int_{-T}^{\infty} P^{(3)}_{Total}(t)\exp(i\omega_t t)dt \approx i\left\{\sum_{ab}\frac{\Phi^1_{abcd}}{\omega_{RS}-\omega_{ab}+i(\Lambda_{NB}-\Gamma_{ab})}+\sum_{cd}\frac{\Phi^2_{abcd}-\Phi^3_{abcde}}{\omega_{RS}-\omega_{cd}+i(\Lambda_{NB}-\Gamma_{cd})}\right\}\exp(i\omega_{RS}T-\Lambda_{RS}T) \quad \text{(S8)}$$

where the Raman shift is $\omega_{RS}=\omega_{NB}-\omega_t$. Equation (S8) suggests that the negative amplitude near 3050 cm^{-1} in Figure 5b originates in an interference between Φ^2_{abcd} and Φ^3_{abcde}, where $\Phi^3_{abcde}>\Phi^2_{abcd}$. The interpretation that $\Phi^3_{abcde}>\Phi^2_{abcd}$ is consistent with the sign of the transient absorption signals shown in the main paper (i.e., net photoinduced absorption). Similarly, the positive amplitude near 2900 cm^{-1} reflects the first term in Equation (S8), which possesses resonances at vibrational frequencies in the ground electronic state, ω_{ab}.

Equation (S8) makes clear an important advantage to the present pulse configuration: the spectral resolution is enhanced by a cancellation between the material dephasing rates, Γ_{ab} or Γ_{cd}, and the bandwidth of the narrow band pulse, Λ_{NB}. By contrast, the conventional Raman gain technique does not possess this enhancement in spectral resolution and must also contend with undesired nonlinearities such as those responsible for the broadband response in Figure S12a.

References

1. Shaw GB, Brown CL, and Papanikolas JM (2002) Investigation of interligand electron transfer in polypyridyl complexes of Os(II) using femtosecond polarization anisotropy methods: Examination of Os(bpy)32+ and Os(bpy)2(mab)2+. *J. Phys. Chem. A* 106(8):1483-1495.
2. Shaw GB and Papanikolas JM (2002) Triplet-triplet annihilation of excited states of polypyridyl Ru(II) complexes bound to polystyrene. *J. Phys. Chem. B* 106(24):6156-6162.
3. Shaw GB, Styers-Barnett DJ, Gannon EZ, Granger JC, and Papanikolas JM (2004) Interligand electron transfer dynamics in [Os(bpy)3]2+ : Exploring the excited state potential surfaces with femtosecond spectroscopy. *J. Phys. Chem. A* 108(23):4998-5006.
4. Styers-Barnett DJ, Ellison SP, Mehl BP, Westlake BC, House RL, Park C, Wise KE, and Papanikolas JM (2008) Exciton dynamics and biexciton formation in single-walled darbon nanotubes studied with femtosecond transient absorption spectroscopy. *Journal of Physical Chemistry C* 112:4507-4516.
5. Styers-Barnett DJ, Ellison SP, Park C, Wise KE, and Papanikolas JM (2005) Ultrafast dynamics of single-walled carbon nanotubes dispersed in polymer films. *J. Phys. Chem. A* 109(2):289-292.
6. Maxwell KA, Sykora M, DeSimone JM, and Meyer TJ (2000) One-pot synthesis and characterization of a chromophore-donor-acceptor assembly. *Inorg Chem* 39(1):71-75.
7. Yip R, Sharma D, Giasson R, and Gravel D (1984) Picosecond excited-state absorption of alkyl nitrobenzenes in solution. *J. Phys. Chem.*:5770-5772.
8. Forbes MDE (1997) *Photochem. Photobiol.* 65:73.
9. Becke AD (1988) Density-functional exchange-energy approximation with correct asymptotic behavior. *Phys Rev A* 38(6):3098-3100.
10. Becke AD (1993) Density-functional thermochemistry 3. The role of exact exchange. *J. Chem. Phys.* 98(7):5648-5652.
11. Becke AD (1993) A new mixing of hartree-fock and local density-functional theories. *J. Chem. Phys.* 98(2):1372-1377.
12. Lee CT, Yang WT, and Parr RG (1988) Development of the Colle-Salvetti correlation-energy formula into a functional of the electron-density. *Phys Rev B* 37(2):785-789.
13. Bauernschmitt R and Ahlrichs R (1996) Treatment of electronic excitations within the adiabatic approximation of time dependent density functional theory. *Chem. Phys. Lett.* 256(4-5):454-464.
14. Casida ME, Jamorski C, Casida KC, and Salahub DR (1998) Molecular excitation energies to high-lying bound states from time-dependent density-functional response theory: Characterization and correction of the time-dependent local density approximation ionization threshold. *J. Chem. Phys.* 108(11):4439-4449.
15. Stratmann RE, Scuseria GE, and Frisch MJ (1998) An efficient implementation of time-dependent density-functional theory for the calculation of excitation energies of large molecules. *J. Chem. Phys.* 109(19):8218-8224.
16. Cances E, Mennucci B, and Tomasi J (1997) A new integral equation formalism for the polarizable continuum model: Theoretical background and applications to isotropic and anisotropic dielectrics. *J. Chem. Phys.* 107(8):3032-3041.
17. Mennucci B, Cances E, and Tomasi J (1997) Evaluation of solvent effects in isotropic and anisotropic dielectrics and in ionic solutions with a unified integral equation method: Theoretical bases, computational implementation, and numerical applications. *J. Phys. Chem. B* 101(49):10506-10517.
18. Tomasi J, Mennucci B, and Cammi R (2005) Quantum mechanical continuum solvation models. *Chem. Rev.* 105(8):2999-3093.
19. McCusker JK (2003) Femtosecond absorption spectroscopy of transition metal charge-transfer complexes. *Acc Chem Res* 36(12):876-887.
20. Shank CV, Dienes A, Trozzolo AM, and Myer JA (1970) Near UV to yellow tunable laser emission from an organic dye. *Appl. Phys. Lett.* 16(10):405-407.
21. Womick JM and Moran AM (2009) Exciton coherence and energy transport in the light-harvesting dimers of allophycocyanin. *J. Phys. Chem. B* 113(48):15747-15759.

THE JOURNAL OF PHYSICAL CHEMISTRY B

Article

pubs.acs.org/JPCB

Base-Induced Phototautomerization in 7-Hydroxy-4-(trifluoromethyl)coumarin

Brittany C. Westlake,[†] Jared J. Paul,[‡] Stephanie E. Bettis,[†] Shaun D. Hampton,[†] Brian P. Mehl,[†] Thomas J. Meyer,*[,†] and John M. Papanikolas*[,†]

[†]Department of Chemistry, University of North Carolina at Chapel Hill, Chapel Hill, North Carolina 27599-3290, United States

[‡]Department of Chemistry, Villanova University, Villanova, Pennsylvania 19085, United States

ABSTRACT: Excited-state proton-transfer dynamics between 7-hydroxy-4-(trifluoromethyl)coumarin and 1-methylimidazole base in toluene were studied using ultrafast pump−probe and time-resolved emission methods. Charge-transfer excitation of the hydroxycoumarin shifts electron density from the hydroxyl group to the carbonyl, resulting in an excited state where proton transfer to the base is highly favored. In addition to its the photoacid characteristics, the shift in the hydroxycoumarin electronic distribution gives it characteristics of a photobase as well. The result is a tautomerization process occurring on the picosecond time scale in which the 1-methylimidazole base acts as a proton-transfer shuttle from the hydroxyl group to the carbonyl.

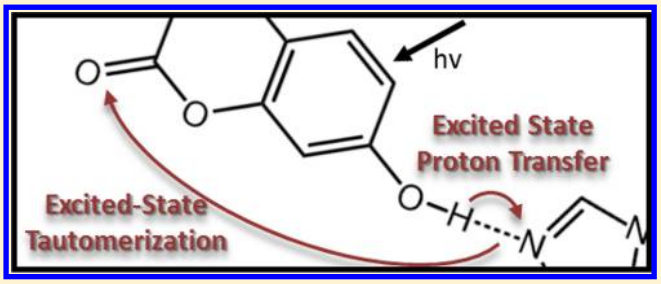

1. INTRODUCTION

Proton-coupled electron-transfer (PCET) reactions and half reactions in which both an electron and proton are transferred have been widely studied.[1−8] They play a special role in biology and in energy conversion reactions in chemistry. The mechanistic details of how PCET reactions occur have been elucidated in considerable detail.[1,8] Clearly defined pathways have been identified in which proton transfer is followed by electron transfer (PT−ET) and in which electron transfer is followed by proton transfer (ET−PT). Although more complex microscopically, pathways have also been identified in which concerted electron−proton transfer (EPT) occurs simultaneously. The combined motion of protons and electrons are also observed in excited states, where intramolecular excitations result in changes in electron density that, for example, can enhance the acidity of a dissociable proton.[7] This effect provides the basis for excited-state proton transfer (ESPT).[9,10]

ESPT occurs in a class of molecules that can undergo dramatic increases in pK_a upon electronic excitation.[11] Enhanced acidity accompanying changes in electronic structure dramatically influence reaction dynamics of proton-transfer events. On the basis of the Förster equation, eq 1, intramolecular charge transfer (ICT) excitation can result in increased acidities of up to 6−8 pK_a units.[11] As an example, excited 2-naphthol demonstrates an increase in acidity of 6.6 pK_a units for the phenolic proton when compared to the ground state.[12] In the Förster equation, $h\nu_1$ is the absorbance energy maxima of the protonated excited state, and $h\nu_2$ is the absorbance energy maxima for the corresponding deprotonated form.

$$pK_a^* = pK_a - \left[\frac{h\nu_1 - h\nu_2}{2.3RT}\right] \quad (1)$$

Time scales for proton transfer are of importance in potential applications. For example, in most applications, an ideal photoacid in water should have a ground-state pK_a of 8 and a pK_a* < 2, below pK_a(H_3O^+) = −1.74, and deprotonates in a few nanoseconds following electronic excitation in aqueous solution, followed by slow reprotonation.[11] The converse of superacids, superbases, has also been observed in excited states in which charge-transfer excitation creates a basic site. Chen et al. found evidence for superbase formation following excitation of an arginine amide-containing peptide where the amide becomes a superbase following electronic excitation.[13] For molecules that contain preformed intramolecular hydrogen bonds without a requirement for diffusion, proton transfer is more readily in competition with excited-state decay.

Coumarins are highly emissive compounds that are commonly utilized as laser dyes. In particular, 7-hydroxycoumarin derivatives have well-characterized emission spectra and have been investigated for their ESPT properties.[14,15] Three emitting states have been observed for these types of compounds, Figure 1. One is the weakly emitting acid that is observable in

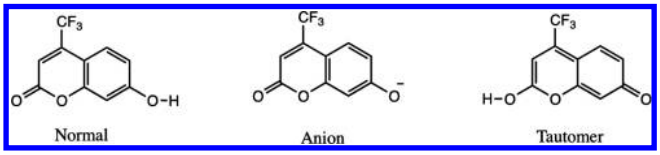

Figure 1. Emitting forms of 7-hydroxy-4-(trifluoromethyl)coumarin (CouOH).

Received: August 27, 2012
Revised: November 21, 2012
Published: November 28, 2012

non-hydrogen-bonding, low dielectric solvents, such as chloroform.[14] The other two emissions are significantly enhanced and occur at lower energy. They occur from the deprotonated anion and from a tautomer emission that is reached by proton transfer to the carbonyl group of the chromophore. The tautomer form becomes favored in the excited state because ICT excitation of 7-hydroxycoumarin derivatives (CouOH) shift electron density from the hydroxyl group to the carbonyl, leading to an electronic configuration in which proton transfer to the carbonyl is favored. A key for tautomer formation is a proton-transfer solvent, such as water, which can donate a proton to the carbonyl in the excited state.[16]

Ultrafast transient techniques have been used to investigate ESPT to the solvent.[17,18] We recently reported a photoinduced electron−proton transfer (photo-EPT) process in the 4-hydroxy-4′-nitro-biphenyl molecule in which instantaneous, concerted proton transfer in the excited state occurs to an external H-bonded base. It was noted that this was due to instantaneous formation of an excited state with an elongated proton−base bond and not a violation of the Franck−Condon principle.[19] A similar conclusion was reached for the ESPT mechanism following excitation of the hydrogen-bonded adduct formed between 7-hydroxy-4-(trifluoromethyl)coumarin and 1-methylimidazole (Scheme 1) in the nonpolar, non-hydrogen-bonding solvent

Scheme 1

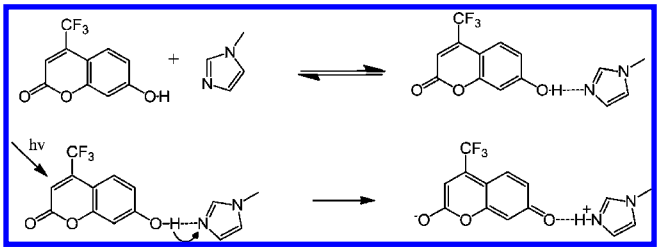

toluene with proton transfer to the external base 1-methylimidazole being highly favored.

Here, we expand on the earlier work with 7-hydroxy-4-(trifluoromethyl)coumarin to examine the excited-state dynamics that occur subsequent to the initial ultrafast proton-transfer event. In its excited state, the coumarin dye is not only a photoacid, but the shift in electron density toward the carbonyl group causes it to also act as an intramolecular excited-state photobase.

We apply time-resolved absorption and emission measurements to reveal a novel tautomerization in which an intra-assembly proton translation of the proton occurs kinetically induced by H-bonding to a second base molecule.

2. EXPERIMENTAL SECTION

A. Materials and Preparation. 7-Hydroxy-4-(trifluoromethyl)-1-coumarin (CouOH) (98%), 1-methylimidazole (1-MeId) (99%), and toluene (Chromasolv Plus for HPLC, >99.9%) were all purchased from Sigma-Aldrich and used as received. Solutions for femtosecond transient absorption and time-correlated single-photon counting (TCSPC) were prepared with 0.34 mM CouOH and 2 mM 1-MeIm base in toluene. Solutions for UV−vis and steady-state emission measurements were made at a range of base concentrations. Prior to time-resolved emission measurements, the samples were deaerated by bubbling argon gas through the sample for ∼30 min.

B. UV−Vis. UV−vis absorption measurements were carried out by using an Agilent Technologies Model 8453 diode array spectrophotometer. Initial absorption measurements were conducted in a 1 cm cuvette and then repeated in a 2 mm cuvette to recreate the path length and concentration conditions used in the femtosecond transient absorption measurements.

C. Steady-State Emission. Steady-state emission measurements were obtained by using a PTI QuantaMaster emission spectrometer. Samples were excited with 355 nm light, and the sample emission was scanned from 360 to 700 nm with background correction. Emission collected using the 2 mm cuvette required that it be placed at a 45° angle relative to the excitation and emission collection slits in the spectrometer. Slit widths of 0.35 mm were used. For steady-state emission studies carried out at 77 K, samples were prepared in an NMR tube, degassed for 30 min with argon gas, and cooled using liquid nitrogen in a home-built dewar that was placed directly in the spectrometer.

D. Time-Correlated Single-Photon Counting (TCSPC). The apparatus consists of a frequency-doubled, mode-locked Ti:Sapphire laser, with a repetition rate adjusted by an acousto-optic modulator (AOM) used in a single-pass configuration. The femtosecond pulses selected by the AOM excite the sample, and the emitted light is collected at 90° relative to excitation, focused onto the slit of a 240 mm focal length single-grating monochromator, and delivered to a cooled, multichannel plate photomultiplier tube (MCP, Hamamatsu R3809U-51). The signal from the MCP is amplified, sent into a 200 MHz constant fraction discriminator (CFD, Tennelec 454), and then used as the start pulse for a time-to-amplitude converter (TAC, Tennelec 864). The stop pulse is obtained by focusing 10% of the excitation beam onto a Si:PIN photodiode, whose output is sent into a variable delay box, then to a CFD, and finally to the TAC. The TAC's output is sent to a multichannel analyzer that is interfaced to a PC. The instrument response of the apparatus is 80 ps at the full width at half-maximum (fwhm).

Femtosecond transient absorption measurements were conducted by using a pump−probe technique that has been described previously in detail.[19,20] Briefly, the excitation source is a chirped pulse Ti:Sapphire regenerative amplification laser system (Clark CPA 2001) that outputs a 800 mW, 775 nm pulse at a 1 kHz rep rate, with an autocorrelation fwhm of 250 fs. The probe pulse was generated by focusing a small portion of the beam into a CaF_2 window to generate a white light continuum from 380 to 700 nm. The spot size at the sample was ∼280 μm. The 355 nm pump pulse was created with a tunable Clark optical parametric amplifier (OPA) (1420 nm) followed by second-harmonic generation (710 nm) and fourth-harmonic generation (355 nm) by focusing the respective beams through beta barium borate (BBO) crystals. The data were collected at the magic angle polarization (54.7 degrees) with the pump beam focused to a ∼1400 μm spot size and power of 0.60 mW. Samples with concentrations of 0.34 mM CouOH with 2 mM 1-MeId base were prepared. Samples were placed in a 2 mm quartz cuvette and degassed with argon gas for 30 min prior to data collection. The chirp in the white light was accounted for by using an optical gating technique described elsewhere.[19,20]

3. RESULTS AND DISCUSSION

A. Steady-State Spectroscopy. *Absorption Spectroscopy.* The ground-state UV−visible spectrum of 7-hydroxy-4-(trifluoromethyl)coumarin (CouOH) in toluene is centered at 330 nm when no base is present (Figure 2). This band arises from an intramolecular charge transfer (ICT) transition that

dx.doi.org/10.1021/jp308505p | J. Phys. Chem. B 2012, 116, 14886−14891

shifts electron density from the phenolic group to the carbonyl. The addition of 1-methylimidazole as a base (:B) results in the systematic shift of the absorption maximum from 330 to 342 nm, consistent with ground-state hydrogen bond formation. The relative similarity in the pK_a values for hydroxycoumarin (−OH, 7.26) and 1-methylimidazole (N:, 7.4) implies formation of a short, tight H-bond.[21] Benesi−Hildebrand analysis of the spectral shifts observed with a series of base concentrations between 0.01 and 2000 mM (Figure 2) gave a hydrogen-bonding association constant (K_a) in the ground state of 2100 M^{-1}.[22]

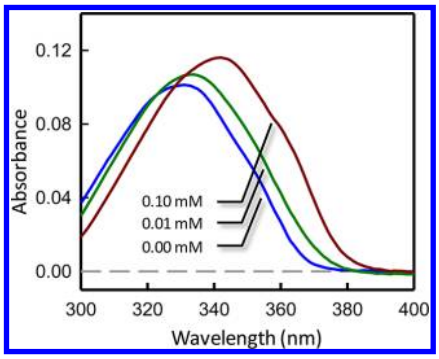

Figure 2. Ground-state UV−vis absorption spectra for 0.34 mM hydroxycoumarin with 0 (blue line), 0.01 (green line), and 0.1 mM (red line) 1-methylimidazole in toluene. The red shift in the absorption band with increasing base reflects the increase in the formation of the hydrogen-bonded adduct.

Emission Spectroscopy. When excited at 330 nm with no base, hydroxycoumarin emits weakly at 403 nm. Addition of small amounts (0.01 mM) of base to the solution dramatically increases the emission intensity (Figure 3), yielding an emission band with λ_{max} = 460 nm, whose intensity systematically increases upon continued addition of base up to 1 mM. In agreement with other studies, we have assigned the 460 nm band to emission from a configuration in which the proton is transferred to the base but remains hydrogen bonded to the hydroxycoumarin anion, that is, $(CouO^{-}\cdots H^{+}-B)^{*}$.[23−25] Complete removal of the proton by a strong base shows the hydroxycoumarin anion to be strongly emissive and further red-shifted with λ_{max} = 506 nm. Adduct emission can be viewed as arising from an anion, whose ground state is stabilized by a H-bond interaction with the protonated base. The dramatic increase in emission of the hydrogen-bonded adduct, even at low base concentrations, highlights the importance of the hydrogen bond between the base and hydroxycoumarin and its effect on the molecule's fluorescence properties. Similar observations were made by Moriya and co-workers where coumarin solutions with added water or alcohol enabled hydrogen bonding.[16,26,27]

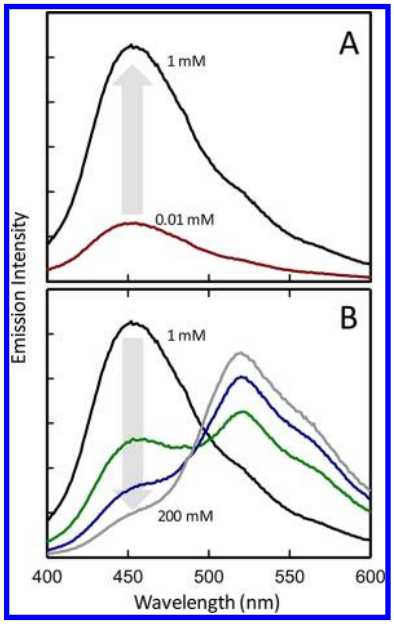

Figure 3. Room-temperature steady-state emission data for 0.34 mM hydroxycoumarin in toluene with varying amounts of 1-methylimidazole; excitation at 355 nm. (A) Low base concentrations of 0.01 (red) and 1 mM (black). The increase in emission intensity reflects the increase in concentration of the hydrogen-bonded adduct. (B) High base concentrations of 1 (black), 40 (green), 100 (blue), and 200 mM (gray).

Steady-state emission spectra at higher base concentrations (10−200 mM) are shown in Figure 3B. With continually higher base concentrations, the emission band at 460 nm decays, while a new band grows in at 520 nm. On the basis of previous reports, the band at longer wavelengths is assigned to the hydroxycoumarin tautomer where the proton is associated with the carbonyl group at the other end of the molecule.[16,26−28] Studies by Moriya described a water bridge in a similar 7-hydroxycoumarin system that enabled the site of protonation to be transferred from the photoacidic OH group to the photobasic carbonyl.[16] In the case of the hydroxycoumarin with 1-methylimidazole in toluene, there are no extra protons to be transferred, and formation of the tautomer necessitates the translation of the proton from one side of the coumarin to the other or between excited coumarin−base couples.

The emission spectra observed in a low-temperature toluene glass at 77 K (Figure 4) show a 440 nm band upon the addition of 1-methylimidazole at concentrations that yield tautomer emission at room temperature. The blue shift relative to the fluid solution is due to a lack of solvent reorganization in the rigid environment in the excited-state charge distribution. The absence of tautomer emission indicates a suppression of the mechanism for delivering the proton to the carbonyl oxygen in the frozen state and at the same time implies that tautomer formation occurs in the excited state after photon absorption occurs.

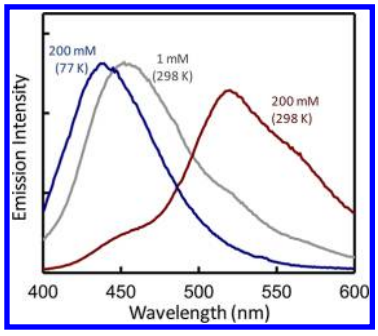

Figure 4. Steady-state emission data for 0.34 mM hydroxycoumarin with 200 mM 1-methylimidazole at 77 K (blue). Also shown are the room-temperature emission data with 1 (gray) and 200 mM (red) 1-methylimidazole. Samples were excited at 355 nm.

B. Time-Resolved Spectroscopy. The observation of emission from the H-bonded CouOH points to rapid proton transfer accompanying excitation of the ICT transition in CouOH, at least on a time scale that is short compared to the excited-state lifetime.

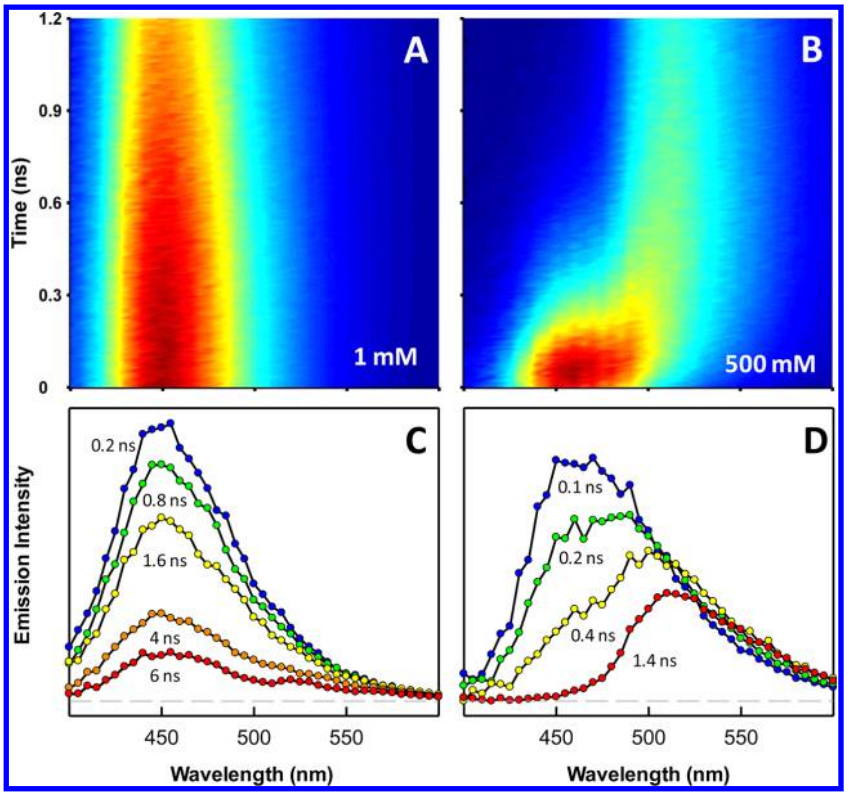

Figure 5. (A) TCSPC emission spectra for hydroxycoumarin with low base concentration (1 mM), following 360 nm excitation. (B) TCSPC emission spectra for hydroxycoumarin with excess base concentration (500 mM), following 360 nm excitation. (C) TCSPC emission spectra for hydroxycoumarin with low base concentration (1 mM), following 360 nm excitation obtained at 0.2, 0.8, 1.6, 4, and 6 ns. (D) TCSPC emission spectra for hydroxycoumarin with excess base concentration (500 mM), following 360 nm excitation obtained at 0.1, 0.2, 0.4, and 1.4 ns.

A recent report from our group examined these early time dynamics using a combination of transient absorption and coherent Raman methods.[19] The results of that work pointed to a novel photo-EPT process in which the proton is transferred to the base during the photoexcitation process, resulting in a hydroxycoumarin anion that is hydrogen bonded to a protonated methylimidiazole base. Here, we focus on the dynamics that take place following that initial proton-transfer event on longer time scales.

Transient Emission. Shown in Figure 5 is time-resolved emission data for hydroxycoumarin with low (2 mM) and high (500 mM) concentrations of added base following 360 nm excitation by an ultrafast laser pulse. Data were collected at a series of emission wavelengths, and Figure 5A and B shows intensity maps that depict the emission as both a function of detection wavelength and time. Emission spectra at a given time are obtained by taking horizontal slices through the data set. Spectra at a series of times are shown for the two base concentrations in Figure 5C and D.

For the low base concentration, the spectra observed at early times (200 ps) show a band at 459 nm that uniformly decays with a 3 ns lifetime. The spectrum agrees well with the steady-state emission spectrum observed under similar conditions and is attributed to the hydroxycoumarin anion hydrogen bound to the protonated base, that is, $CouO^{-}\cdots H^{+}-B$.

A more complicated spectral time profile is seen in the time-resolved emission data collected from hydroxycoumarin in the presence of high base concentrations. At early times, the spectrum appears with a band at 459 nm, and during the first 200–300 ps, the band red shifts to 520 nm, resembling the time-integrated spectrum. The spectral shift of the emission from 459 to 520 nm represents changes to the hydroxycoumarin emission as the protonated base is shuttled from the photoacidic side of the molecule to the photobasic side (Scheme 2),

Scheme 2

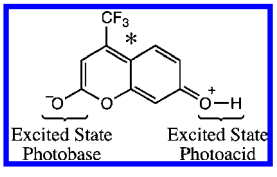

providing a direct view of the tautomerization process. The time-dependent spectral shift is also direct evidence that the tautomerization occurs in the excited state and that the base-dependent emission spectra (Figure 4) are not simply the result of ground-state equilibrium.

Femtosecond Pump–Probe. Femtosecond transient absorption spectra obtained utilizing a 355 nm excitation pulse and white light continuum probe extending from 400 to 650 nm are shown in Figure 6 for both low base and high base concentrations. At early times, the spectra show a narrow positive-going feature with $\lambda_{max} \approx 400$ nm and a broad negative-going feature centered at 465 nm. The negative-going feature is not a ground-state bleach (hydroxycoumarin does not absorb in this spectral region) but rather stimulated emission from the photoexcited state.

The stimulated emission at 465 nm is shown as a function of pump–probe delay for the low base concentration in Figure 7. A significant fraction (~75%) of the stimulated emission appears within the time resolution of our instrument (~800 fs),

dx.doi.org/10.1021/jp308505p | J. Phys. Chem. B 2012, 116, 14886–14891

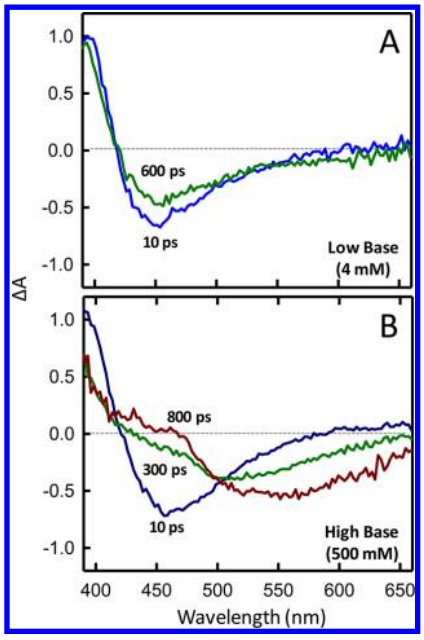

Figure 6. (A) Femtosecond transient absorption difference spectra for HFC with low base concentration (4 mM) or the 1:1 adduct, following 355 nm excitation obtained at 10 (blue line) and 600 ps (green line). (B) Femtosecond transient absorption difference spectra for hydroxycoumarin with high base concentration (500 mM), following 355 nm excitation obtained at 10 (blue line), 300 (green line), and 800 (red line). These spectra show the changes to stimulated emission as the molecule undergoes tautomerization.

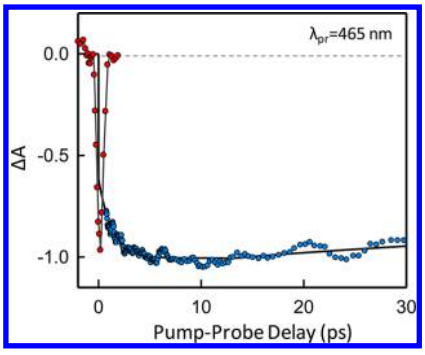

Figure 7. Femtosecond transient stimulated emission data for the hydroxycoumarin 1:1 adduct with 1-MeIm (2 mM) in toluene following 355 nm excitation and detected in a transient differential transmission mode. The red points in the figure represent the instrument response (IR) of the experiment. The IR shown is 800 fs, which is larger than the usual IR of the experiment of 250 fs. This increase in IR is due to an interaction with the pump beam. The pump excitation beam induces a nuclear response in the toluene, represented in the graph. Blue points represent the experimental data at 465 nm, and only data points outside of the instrument response are shown.

followed by a delayed growth during the first 5−10 ps after photoexcitation. The growth of this band reflects the appearance of the strongly emissive (CouO$^-$···H$^+$−B)* species. The prompt emission is attributed to an ultrafast photo-EPT process.[19] The delayed growth in the stimulated emission intensity suggests that a subset of the ensemble undergoes delayed proton transfer to the hydrogen-bonded base, perhaps due to a distribution of different configurations at the moment of photon absorption.

The dynamical shift in the emission is also observed in the pump−probe spectra obtained with high base concentrations. Figure 8 shows pump−probe transients monitored at 465 and

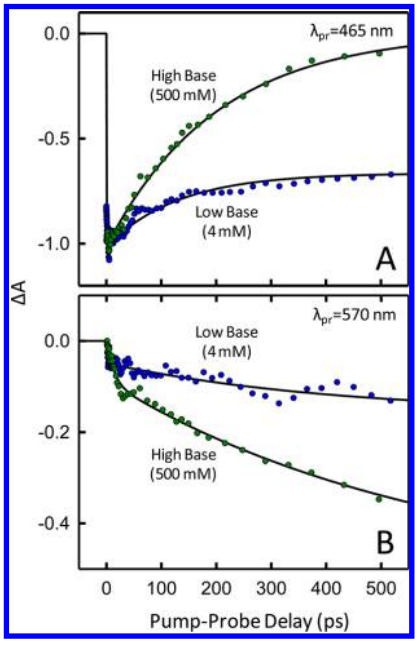

Figure 8. Femtosecond pump−probe kinetics of hydroxycoumarin under high base (500 mM) and low base (4 mM) concentrations for probe detection wavelengths of (A) 465 and (B) 570 nm.

570 nm for two different base concentrations. The transient spectrum at early time (10 ps) is the same for low and high base concentrations. On a time scale of 100s of picoseconds, the decay of the band at 465 nm occurs concurrently with the growth of a band at 570 nm, which is attributed to the green emission of the tautomer.

The kinetics associated with tautomerization depend on the base concentration. For the lower base concentration, there is a decay of only 15−20% of the total pump−probe signal at 465 nm during the first 800 ps after photoexcitation and a slight increase in signal at 570 nm. At this concentration, ∼90% of the hydroxycoumarin is present as a hydrogen-bonded adduct, yet a relatively small fraction of the systems undergo tautomerization. This is in contrast to the kinetics observed with 500 mM added base, where a complete loss of the 465 nm signal and significant growth at 570 nm is observed during this same time period.

This dependence on base concentration indicates that the mechanism for shuttling the proton from one side of the hydroxycoumarin to the other involves more than one base molecule. In aqueous solutions, it has been suggested that this occurs via a hydrogen-bonding bridge formed by a chain of water molecules.[16,27] In this configuration, the proton that leaves the photoacid site need not be the same proton that appears at the photobase side. Because 1-methylimidazole does not contain an acidic proton and the solvent is toluene, a hydrogen-bonding network does not exist, and the proton that is eventually shuttled to the photobase must come from the hydroxyl group.

The involvement of more than one base suggests that proton shuttling is not simply by diffusion of the protonated base. A possible mechanism, consistent with the observed base dependence, is illustrated in Scheme 3. In that mechanism, proton shuttling occurs by formation of the proton adduct, MeIm···$^+$HImMe, which

dx.doi.org/10.1021/jp308505p | J. Phys. Chem. B 2012, 116, 14886−14891

Scheme 3

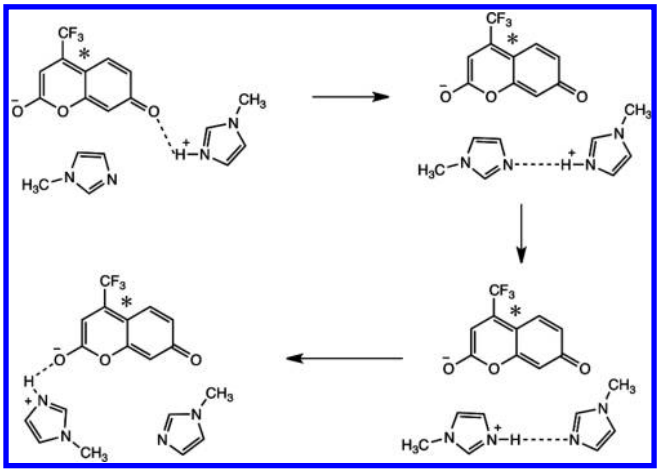

"shuttles" the proton to the more basic Cou−O$^-$ site on the dye through a configuration in which the proton "hops" from one methylimidazole to another in close proximity.

4. CONCLUSIONS

We report here the ESPT dynamics between 7-hydroxy-4-(trifluoromethyl)coumarin and 1-methylimidazole base in toluene. The toluene solvent is nonpolar and lacks the ability to act as a proton-transfer medium without utilizing the 1-methylimidazole as a shuttle. Protonated hydroxycoumarin is a weak emitter; however, ICT in hydroxycoumarin upon electronic excitation results in an excited state where proton transfer to base is highly favored. The deprotonated anion emits intensely. In addition to its characteristics as a photoacid, the ICT event in hydroxycoumarin shifts the electronic distribution in the molecule to give it characteristics of a photobase as well. The carbonyl component becomes more electron rich, and a tautomerization event is favored provided a mechanism for proton delivery is in place. In a fluid state, the 1-methylimidazole base can act as a proton-transfer shuttle and favor tautomerization at higher base concentrations. However, in the frozen state at 77 K, the mobile delivery system is shut off, and only emission from the anion at 439 nm is observed with no tautomer emission. The excited-state dynamics of proton transfer are also base-concentration-dependent. In all cases, proton transfer occurs rapidly, with a majority of the events taking place within the time resolution of the experiment. At higher base concentrations, the tautomer emission grows in over the course of 100s of picoseconds as the proton is shuttled to the photobasic site in the hydroxycoumarin from the mobile 1-methylimidazole base.

AUTHOR INFORMATION

Corresponding Author

*E-mail: john_papanikolas@unc.edu (J.M.P.); tjmeyer@unc.edu (T.J.M.).

Notes

The authors declare no competing financial interest.

ACKNOWLEDGMENTS

Support from the National Science Foundation through Grants CHE-0957215 (T.J.M.) and CHE-0809045 and later CHE-1213379 (J.M.P.) is gratefully acknowledged.

REFERENCES

(1) Weinberg, D. R.; Gagliardi, C. J.; Hull, J. F.; Murphy, C. F.; Kent, C. A.; Westlake, B. C.; Paul, A.; Ess, D. H.; McCafferty, D. G.; Meyer, T. J. *Chem. Rev.* **2012**, *112*, 4016−4093.
(2) Meyer, T. J.; Huynh, M. H. V.; Thorp, H. H. *Angew. Chem., Int. Ed.* **2007**, *46*, 5284−5304.
(3) Huynh, M. H. V.; Meyer, T. J. *Chem. Rev.* **2007**, *107*, 5004−5064.
(4) Cukier, R. I.; Nocera, D. G. *Annu. Rev. Phys. Chem.* **1998**, *49*, 337−369.
(5) Reece, S. Y.; Nocera, D. G. *Annu. Rev. Biochem.* **2007**, *78*, 673−699.
(6) Mayer, J. M. *Annu. Rev. Phys. Chem.* **2004**, *55*, 363−390.
(7) Tolbert, L. M.; Solntsev, K. M. *Acc. Chem. Res.* **2002**, *35*, 19−27.
(8) Gagliardi, C. J.; Vannucci, A. K.; Concepcion, J. J.; Chen, Z.; Meyer, T. J. *Energy Environ. Sci.* **2012**, *5*, 7704−7717.
(9) Hsieh, C.-C.; Jiang, C.-M.; Chou, P.-T. *Acc. Chem. Res.* **2010**, *43*, 1364−1374.
(10) Gagliardi, C. J.; Westlake, B. C.; Kent, C. A.; Paul, J. J.; Papanikolas, J. M.; Meyer, T. J. *Coord. Chem. Rev.* **2010**, *254*, 2459−2471.
(11) Nunes, R. M. D.; Pineiro, M.; Arnaut, L. G. *J. Am. Chem. Soc.* **2009**, *131*, 9456−9462.
(12) Tolbert, L. M.; Haubrich, J. E. *J. Am. Chem. Soc.* **1994**, *116*, 10593−10600.
(13) Chen, X.; Turecek, F. *J. Am. Chem. Soc.* **2006**, *128*, 12520−12530.
(14) Yakatan, G. J.; Juneau, R. J.; Schulman, S. G. *Anal. Chem.* **1972**, *44*, 1044−1046.
(15) Zinsli, P. E. *J. Photochem.* **1974/75**, *3*, 55−69.
(16) Moriya, T. *Bull. Chem. Soc. Jpn.* **1983**, *56*, 6−14.
(17) Rini, M.; Magnes, B.-Z.; Pines, E.; Nibbering, E. T. J. *Science* **2003**, *301*, 349−352.
(18) Mohammed, O. F.; Pines, D.; Dreyer, J.; Pines, E.; Nibbering, E. T. J. *Science* **2005**, *310*, 83−86.
(19) Westlake, B. C.; Brennaman, M. K.; Concepcion, J. J.; Paul, J. J.; Bettis, S. E.; Hampton, S. D.; Miller, S. A.; Lebedeva, N. V.; Forbes, M. D. E.; Moran, A. M.; et al. *Proc. Natl. Acad. Sci. U.S.A.* **2011**, *108*, 8554−8558.
(20) Shaw, G. B.; Brown, C. L.; Papanikolas, J. M. *J. Phys. Chem. A* **2002**, *106*, 1483−1495.
(21) Habeeb, M. M. *App. Spec. Rev.* **1997**, *32*, 103−140.
(22) Concepcion, J. J.; Brennaman, M. K.; Deyton, J. R.; Lebedeva, N. V.; Forbes, M. D. E.; Papanikolas, J. M.; Meyer, T. J. *J. Am. Chem. Soc.* **2007**, *129*, 6968−6969.
(23) Shank, C. V.; Dienes, A.; Trozzolo, A. M.; Myer, J. A. *Appl. Phys. Lett.* **1970**, *16*, 405−407.
(24) Choudhury, S. D.; Pal, H. *J. Phys. Chem. B* **2009**, *113*, 6736−6744.
(25) Choudhury, S. D.; Nath, S.; Pal, H. *J. Phys. Chem. B* **2008**, *112*, 7748−7753.
(26) Moriya, T. *Bull. Chem. Soc. Jpn.* **1988**, *61*, 753−759.
(27) Moriya, T. *Bull. Chem. Soc. Jpn.* **1988**, *61*, 1873−1886.
(28) Schulman, S. G.; Rosenberg, L. S. *J. Phys. Chem.* **1979**, *83*, 447−451.

Ultrafast Energy Transfer between the ^{3}MLCT State of $[Ru^{II}(dmb)_2(bpy\text{-}an)]^{2+}$ and the Covalently Appended Anthracene

Jon R. Schoonover, Dana M. Dattelbaum, Anton Malko, Victor I. Klimov, and Thomas J. Meyer*

Los Alamos National Laboratories, Los Alamos, New Mexico 87545

David J. Styers-Barnett, Erika Z. Gannon, Jeremy C. Granger, W. Steven Aldridge, III, and John M. Papanikolas*

Department of Chemistry, University of North Carolina, Chapel Hill, North Carolina 27599

Received: December 7, 2004

The time scale for triplet−triplet energy transfer (EnT) between a Ru(II) chromophore and a ligand bound anthracene acceptor in $[Ru^{II}(dmb)_2(bpy\text{-}an)]^{2+}$ (dmb = 4,4′-dimethyl-2,2-bipyridine; bpy-an = 4-(9-anthrylethylene), 4-methyl-2,2-bipyridine) has been measured using femtosecond transient absorption spectroscopy. The appearance of the anthracene excited state is monitored following photoexcitation to a metal-to-ligand charge transfer (MLCT) state via the $\pi\pi^*$ absorption of the triplet excited state of anthracene. Our time-resolved experiments show the presence of fast, sub-100 ps energy transfer to the anthracene occurring on two characteristic time scales of 23 and 72 ps.

I. Introduction

The combined optical properties and photostability of Ru(II) and Os(II) trispolypyridyl compounds make them attractive building blocks for molecular devices.[1−6] However, to rationally design molecular architectures based on chromophores that have specific functionalities we must understand in detail how energy and charge flow within molecular building blocks as well as between adjacent components. Time-resolved studies performed in our lab and others indicate that many of the photoinduced processes, including internal conversion (IC), vibrational cooling (VC), interligand electron transfer (ILET), and energy transfer (EnT), happen on similar time scales.[4−7] These studies have focused on primarily the dynamics within a single photoexcited complex. Our attention now turns to the dynamics of energy transport between covalently attached components. In this paper, we describe femtosecond transient absorption studies of energy transfer between a Ru(II) polypyridyl chromophore with a covalently appended anthracene acceptor.

Energy transfer has been studied between Ru(II) polypyridyl complexes and unbound aromatics, as well as covalently appended aromatics, using steady state and nanosecond time-resolved emission spectroscopies,[8−16] and several trends have been identified. When naphthalene is the acceptor, energy transfer from the lowest metal-to-ligand charge-transfer triplet (^{3}MLCT) state[17] is not observed because the aromatic triplet excited state is higher in energy, and thus the luminescence from the ^{3}MLCT is unaltered. Pyrene's excited state is isoergic with the ^{3}MLCT state ($\Delta G° \sim 0$) and equilibrium between the two triplet states is established through forward and reverse energy transfer. In this system, the long lifetime of the $^3\pi\pi^*$ state extends the MLCT luminescence lifetime, which can be as long as 145 μs.[14] Anthracene, however, has an excited triplet state that is lower in energy, and therefore ^{3}MLCT luminescence is quenched via efficient energy transfer.

While energy transfer in these bichromophoric systems has been widely researched, many questions still remain. For example, although it is known that Ru(II)polypyridyl−anthracene complexes undergo energy transfer with near unit efficiency, both the time scale of this process and its relationship to other excited-state processes (e.g., VC, IC, ILET) are unknown. The experiments presented here use femtosecond transient absorption spectroscopy to measure energy transfer rate constants from the ^{3}MLCT state of the metal complex to a $^3\pi\pi^*$ state on the anthracene in $[Ru^{II}(dmb)_2(bpy\text{-}an)]^{2+}$, where dmb = 4,4′-dimethyl,2,2′-bipyridine and bpy-an = 4-(9-anthrylethyl),4′-methyl-2,2′-bipyridine (**1**).

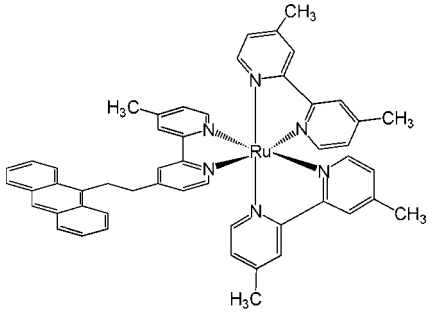

(1)

We observe fast, ^{3}MLCT → An energy transfer that occurs with two characteristic time components of 23 and 72 ps. These components could reflect the presence of two different ground state conformations (e.g., with the An folded in near the bypyridine or with the An extended out at the end of its tether) or the flow of MLCT excitation among the three polypyridyl ligands prior to energy transfer to the anthracene. Regardless of the mechanism, this result does establish that energy transfer is essentially complete on a sub-100 ps time scale with approximately 60% of the total excited-state population transferred to the ligand-bound anthracene in about 70 ps.

10.1021/jp044444j CCC: $30.25
Published on Web 03/02/2005

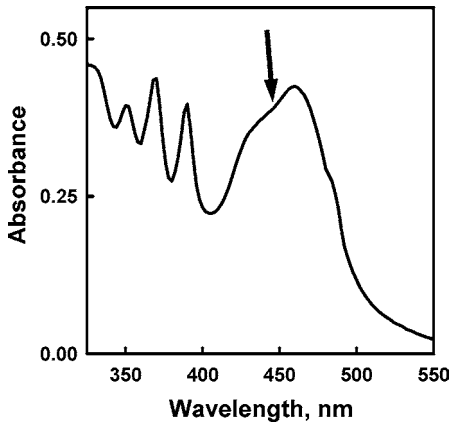

Figure 1. Absorption spectrum of $[Ru^{II}(dmb)_2(bpy\text{-}an)]^{2+}$. The arrow indicates the excitation wavelength.

II. Experimental Description

The femtosecond transient absorption spectrometer is based on a commercially available ultrafast laser system (Clark CPA-2001) consisting of an erbium-doped fiber ring oscillator and a chirped pulse Ti:sapphire regenerative amplifier that is pumped by a frequency doubled, Q-switched Nd:YAG laser. The amplifier produces 120 fs laser pulses at 775 nm with a 1 kHz repetition rate and a pulse energy of approximately 950 μJ/pulse. The majority of this laser output is sent into an optical parametric amplifier (OPA) to provide tunable femtosecond excitation laser pulses (pump beam). The remainder of the laser output is focused at a CaF_2 window to generate the white light continuum used as the probe beam. Further details of the experimental apparatus have been described elsewhere.[5] For the experiments presented in this paper, the OPA was tuned to produce 450 nm pump pulses ($\sim$1 μJ/pulse) focused to a 500 μm spot size and overlapped with the probe beam at the sample. Transient absorption spectra were collected between 350 and 430 nm. The polarization angle between the pump and probe beams was set to the magic angle (54.7°) to eliminate polarization effects in the collected spectra.

The salt of $[Ru^{II}(dmb)_2(bpy\text{-}an)](PF_6)_2$ was prepared and characterized as described previously.[18] Dilute solutions were prepared in distilled, dried acetonitrile, placed in a 2 mm path length cuvette, and flowed using a peristaltic pump. All solutions were deoxygenated by sparging with argon for 1 h and were kept under argon for the duration of the spectroscopic measurements. Efforts were made to eliminate all unnecessary light to prevent photodegradation of the sample. Photodegradation occurs as endoperoxide formation across the center ring of the anthracene. This destroys the acceptor and shuts down the pathway for energy transfer in the complex. All experiments were conducted at room temperature (20 °C).

III. Results and Disscussion

The ground-state absorption spectrum of $[Ru(dmb)_2(bpy\text{-}an)]^{2+}$ in acetonitrile (Figure 1) exhibits several prominent features. The absorptions between 340 and 400 nm arise from $\pi\pi^*$ transitions of ground-state anthracene, and the broad transition centered at 450 nm arises from the promotion of an electron from a dπ orbital on the metal center to a π^* orbital on one of the three polypyridyl ligands to form a ^{1}MLCT state. Bands due to direct excitation to the lowest ^{3}MLCT states occur in the low energy tail of the absorption spectrum. The MLCT absorption band in the functionalized complex is identical in shape to the spectrum of $[Ru(dmb)_3]^{2+}$, indicating that the electronic structure of the Ru core is not altered by the presence of the anthracene moiety. Thus, excitation at 450 nm exclusively excites the metal polypyridyl core.

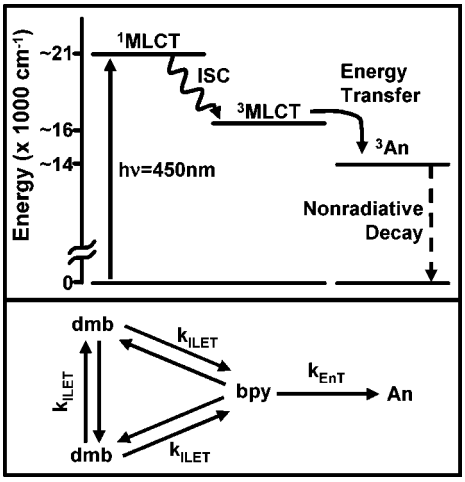

Figure 2. Upper panel: Energy level diagram for $[Ru^{II}(dmb)_2(bpy\text{-}an)]^{2+}$. Lower panel: Kinetic scheme for interligand electron transfer and energy transfer in the molecule. Initial excitation can occur on any of the polypyridyl ligands (dmb or bpy) with the final fate for excited-state energy on the anthracene (An).

An energy level diagram depicting the dynamic processes that occur in the complex is displayed in the upper portion of Figure 2. Transient absorption studies on $[Ru^{II}(bpy)_3]^{2+}$ have shown[6] that photoexcitation of the ^{1}MLCT state is followed by relaxation into a manifold of ^{3}MLCT states within 300 fs. As noted in Figure 2, there are three degenerate (or nearly degenerate) MLCT states. Two are based on the dmb liand, and one is based on the polypyridyl fragment of the bpy-an ligand.

Because this relaxation takes place within the time resolution of our instrument, the ^{3}MLCT is the earliest discernible state in these experiments. The driving force for energy transfer[19] from the ^{3}MLCT state to the lowest $\pi\pi^*$ triplet state of anthracene is 2200 cm^{-1} and is sufficiently rapid that EnT occurs with near unit efficiency. As a result, all luminescence from the Ru(II) core is quenched. The anthracene excited state decays back to the ground state through primarily nonradiative pathways with a lifetime well outside the time scale of these experiments ($\gg$1 ns).[18]

Excited state absorption spectra of the Ru-bpy-an complex at a series of times after photoexcitation are shown in Figure 3. At early times, the spectrum shows a broad absorption centered at 370 nm arising from the ^{3}MLCT states of the $[Ru^{II}(dmb)_3]^{2+}$ core. As time evolves this feature decays away and a strong absorption appears at 425 nm. This new band corresponds to the $^3\pi\pi^*$ excited state of anthracene. The isosbestic point at 395 nm is evidence of a simple D $\rightarrow$ A energy transfer process. The kinetics associated with the appearance of the $^3\pi\pi^*$ state are depicted in Figure 3B, which shows that approximately 60% of the total MLCT excited-state population is transferred to the ligand-bound anthracene in about 70 ps.

This time scale is comparable to triplet−triplet energy transfer rates observed between polypyridylmetal complexes and ligand bound acceptors when the two are linked via a conjugated bridge. Castellano et al.[14] have reported $\tau_{EnT} = 35$ ps in a Ru(polypyridyl) complex covalently attached to a pyrene molecule through a single bond. Harriman et al.[9] measured τ_{EnT} for Ru and Os complexes covalently attached to a pyrene molecule through a triple bond, as well as through a Pt spacer. In the conjugated system $\tau_{EnT} = 7$ ps while the nonconjugated Pt bridge slowed transfer down to the nanosecond time scale. Juris

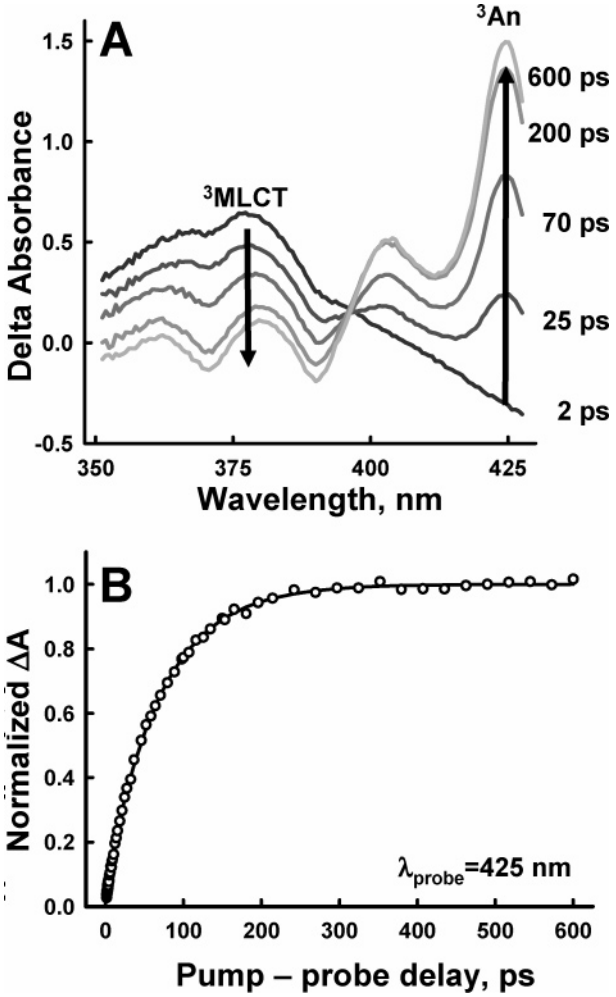

Figure 3. (A) Excited-state absorption spectra at a series of pump−probe delays. Decay of the ^{3}MLCT absorption at 375 nm corresponds with the growth of the intense ^{3}An absorption at 425 nm. (B) Transient signal for ^{3}An excited-state growth. The solid line shows the best-fit results of the model.

and Prodi[20] have also measured energy transfer in nonconjugated metal trispolypyridyl−pyrene supermolecular systems, and found that energy transfer occurs in nanoseconds as well. While the connective bridges in these systems are relatively dissimilar to ours, a general trend of reduced rate constants in nonconjugated systems for triplet energy transfer has been observed elsewhere. Our system exhibits transfer times that resemble the conjugated systems, despite the fact that there is no conjugation present in our bridge. A possible explanation for the fast rate of energy transfer in our complex could be that the ethyl linkage allows adequate mobility for the anthracene to position itself so that the molecular orbitals of the bpy and the anthracene could achieve good electronic communication.

Closer inspection of the absorption transient shows the presence of two time components in the growth of the anthracene excited-state absorption. A nonlinear least-squares fit to a biexponential growth reveals fast and slow components of 23 (10%) and 72 ps (90%), respectively. Biphasic kinetics implies that two pathways to energy transfer exist.

One simple explanation of this biphasic growth behavior is that it stems from two different donor−acceptor ground state conformations due to the flexible coupling between the metal complex and the anthracene. The fast component (23 ps) would then correspond to a geometry with the anthracene folded close to the bipyridine ligand (in), and a slow energy-transfer time (72 ps) would result when the anthracene was extended away from the metal complex (out). The observed amplitudes (10% and 90%) would then reflect the relative populations of the two states.

A second explanation for this biphasic behavior is that it stems from the flow of MLCT excitation among the three ligands *prior* to energy transfer to the anthracene. Biphasic growth kinetics arise in this model (Figure 2) because photoabsorption has *equal* probability of placing the MLCT excitation on any one of the three ligands, resulting in equal populations on each ligand. Excited states formed on the bpy-an ligand undergo direct energy transfer to the appended anthracene (An) with a rate constant k_{EnT}. MLCT states formed on one of the dmb ligands first require energy migration to the bpy-an ligand (i.e. interligand electron transfer, ILET) *before* energy transfer to the anthracene occurs. The rate of the anthracene excited-state growth observed in the experiment is a superposition of these two pathways.

We have to fit the growth of the anthracene excited state to this kinetic model in order to extract rate constants for ILET, k_{ILET}, and energy transfer, k_{EnT}. In $[Ru(dmb)_2(bpy\text{-}an)]^{2+}$ the polypyridyl fragments of all the ligands are nearly energetically equivalent. The driving force for internal energy transfer from dmb to bpy-an ligand is estimated to be only $\sim$150 cm^{-1} from electrochemical data. Given the small driving force, we approximate $k_{ILET} = k_{ILET}^{-1}$ in the analysis. Following photon absorption, the excited state population, which is initially distributed equally among the three ligands, evolves though ILET and energy transfer until it resides solely on the anthracene. The result of a nonlinear least-squares fit to the model is the solid line in Figure 3B. This analysis yields a lifetime for energy transfer of 16 ps ($k_{EnT} = 6.25 \times 10^{-14}$ s^{-1}), and an ILET lifetime of 27 ps ($k_{ILET} = 3.70 \times 10^{-14}$ s^{-1}). The latter value is similar to that reported by Malone and Kelley for $Ru(bpy)_3^{2+}$ (47 ps),[21] but three times slower than the ILET rate constant measured in our lab for $Os(bpy)_3^{2+}$ (8.7 ps in acetonitrile).[5] The slower rate constant for Ru compared to Os is consistent with its lower spin−orbit constant ($\sim$1000 vs $\sim$3000 cm^{-1}) and a lesser degree of mixing between the nearly degenerate ^{3}MLCT excited states.

The amplitudes of the fast and slow components of this model are determined by relative magnitudes of k_{ILET} and k_{EnT}. When ILET is fast compared to energy transfer ($k_{ILET} \gg k_{EnT}$), the excited state population will off-load slowly to anthracene. Because energy transfer is the rate-limiting step, the fast amplitude will become zero and a single slow component will be observed. On the other hand, when energy transfer is significantly faster that ILET ($k_{EnT} \gg k_{ILET}$), one-third of the population will transfer to anthracene promptly, while the other two-thirds will be delayed due to the ILET step. The result is that both fast and slow components will be observed, and their amplitudes will be 33% and 66%, respectively. When the two rates are comparable, a fast component will be observed, but its amplitude will be less than 33% of the total. In this kinetic scheme, the relative amplitudes of the two components are constrained by the magnitudes of the rate constants themselves, and the relative amplitudes that are observed in the experiment are consistent with those predicted by the model given the two time scales. Although this observation does not confirm this energy flow model, it does lend support to its validity. Regardless of the origin of this biphasic behavior, the experiments presented in this publication have identified that energy transfer occurs on a sub-100 ps time scale.

Acknowledgment. Funding for this project was provided by the Petroleum Research Fund (grant 36385-G6), Research Corporation Award RI0048, the National Science Foundation (CHE-0301266), the United States Department of Energy (grant DE-FG02-96ER 14607), Los Alamos National Laboratories' Laboratory Directed Research and Development Program (project 20020222ER), and the University of North Carolina.

References and Notes

(1) Creutz, C.; Chou, M.; Netzel, T. L.; Okumura, M.; Sutin, N. *J. Am. Chem. Soc*. **1980**, *120*, 1309−1319.

(2) Meyer, T. J. *Pure Appl. Chem.* **1986**, *58*, 1193.

(3) Vlcek, A., Jr. *Coord. Chem. Rev.* **2000**, *200*−*202*, 933−977.

(4) Damrauer, N. H.; McCusker, J. K. *J. Phys. Chem. A* **1999**, *103*, 8440−8446.

(5) Shaw, G. B.; Brown, C. L.; Papanikolas, J. M. *J. Phys. Chem. A* **2002**, *106*, 1483−1495.

(6) Damrauer, N. H.; Cerullo, G.; Yeh, A.; Boussie, T. R.; Shank, C. V.; McCusker, J. K. *Science* **1997**, *275*, 54−57.

(7) Monat, J. E.; McCusker, J. K. *J. Am. Chem. Soc.* **2000**, *122*, 4092−4097.

(8) Olmsted, J.; Meyer, T. J. *J. Phys. Chem.* **1987**, *91*, 1649−1655.

(9) Hissler, M.; Harriman, A.; Khatyr, A.; Ziessel, R. *Chemistry*: *A Eur. J.l* **1999**, *5*, 3366−3381.

(10) Belser, P.; Dux, R.; Baak, M.; De Cola, L.; Balzani, V. *Angew. Chem. Int. Ed. Engl.* **1995**, *34*, 595−598.

(11) Wilson, G. J.; Sasse, W. H. F.; Mau, A. W. H. *Chem. Phys. Lett.* **1996**, *250*, 583−588.

(12) Simon, J. A.; Curry, S. L.; Schmehl, R. H.; Schatz, T. R.; Piotrowiak, P.; Jin, X.; Thummel, R. P. *J. Am. Chem. Soc.* **1997**, *119*, 11012−11022.

(13) El-ghayoury, A.; Harriman, A.; Khatyr, A.; Ziessel, R. *J. Phys. Chem. A* **2000**, *104*, 1512−1523.

(14) Tyson, D. S.; Henbest, K. B.; Bialecki, J.; Castellano, F. N. *J. Phys. Chem. A* **2001**, *105*, 8154−8161.

(15) McClenaghan, N. D.; Barigelletti, F.; Maubert, B.; Campagna, S. *Chem. Commun.* **2002**, 602−603.

(16) Maubert, B.; McClenaghan, N. D.; Indelli, M. T.; Campagna, S. *J. Phys. Chem. A* **2003**, *107*, 447−455.

(17) The lowest ^{3}MLCT state is actually a manifold of three closely spaced states split in the parent triplet by low symmetry and spin−orbit coupling.

(18) Weinheimer, C.; Choi, Y.; Caldwell, T.; Gresham, P.; Olmsted, J., III *J. Photochem. Photobiol. A*: *Chemistry* **1994**, *78*, 119−126.

(19) Aldridge, W. S., III *Design and Synthesis of Chromophore-Quencher Molecular Assemblies*; University of North Carolina, 2000.

(20) Juris, A.; Prodi, L. *New J. Chem.* **2001**, *25*, 1132−1135.

(21) Malone, R. A.; Kelley, D. F. *J. Chem. Phys.* **1991**, *95*, 8970−8976.

J|A|C|S
ARTICLES
Published on Web 11/20/2002

Turning the $[Ru(bpy)_2dppz]^{2+}$ Light-Switch On and Off with Temperature

Matthew K. Brennaman, James H. Alstrum-Acevedo, Cavan N. Fleming, Paul Jang, Thomas J. Meyer,*,† and John M. Papanikolas*

Contribution from the Venable and Kenan Laboratories, Department of Chemistry, University of North Carolina at Chapel Hill, Chapel Hill, North Carolina 27599

Received July 29, 2002

Abstract: We report temperature-dependent excited-state lifetime measurements on $[Ru(bpy)_2dppz]^{2+}$ in both protic and aprotic solvents. These experiments yield a unifying picture of the excited-state photophysics that accounts for observations in both types of solvent. Our measurements support the notion of bpy-like and phz-like states associated with the dppz ligand and show that the ligand orbital associated with the bright state is similar in size to the corresponding orbital in the ^{3}MLCT state of $[Ru(bpy)_3]^{2+}$. In contrast to the current thinking, the experiments presented here indicate that the light-switch effect is not driven by a state reversal. Rather, they suggest that the dark state is always lowest in energy, even in aprotic solvents, and that the light-switch behavior is the result of a competition between energetic factors that favor the dark state and entropic factors that favor the bright (bpy) state.

I. Introduction

There has been intense interest in $[Ru(bpy)_2dppz]^{2+}$ (Figure 1) as a luminescent probe of DNA. In particular, this complex is brightly luminescent when bound to DNA, but is nonemissive in aqueous solution.[1−3] The "light-switch" effect stems from hydrogen bond formation with water, which quenches the excited-state luminescence and reduces the quantum yield by 2−3 orders of magnitude. In the bound form, the dppz ligand is intercalated into the DNA strand. Intercalation shields the phenazine nitrogens from the solvent and results in a luminescent excited state. The stark contrast between the dark and bright states of this molecule makes this complex useful for the study of DNA and other nonpolar microenvironments.[4−11]

The light-switch property does not require DNA for activation, and luminescence is observed in a number of aprotic environments. Consequently, this complex has been studied in a wide variety of solvents in an attempt to understand the origin of the light-switch mechanism.[12−14] The photophysical factors that govern this function are thought to arise from the presence of two metal-to-ligand charge-transfer (MLCT) states on the dppz ligand: a bright, luminescent state associated with the bipyridine (bpy) fragment of the dppz ligand and a dark, nonluminescent state localized largely on the phenazine (phz) portion. It has been suggested that in aprotic environments, the bright state is the lower energy state, and thus luminescence is observed. The light-switch is activated in protic solvents by hydrogen bond formation at the phz nitrogens, which lowers the energy of the dark state below the bright state. Because of

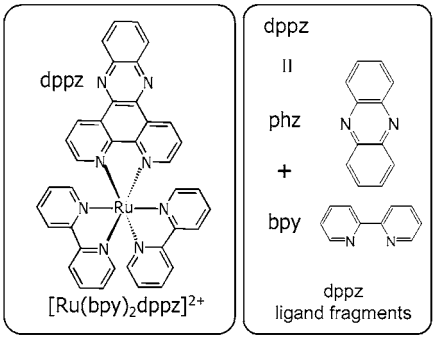

Figure 1. Chemical structure of the light-switch complex, $[Ru(bpy)_2dppz]^{2+}$, and ligand fragments discussed in the text.

* To whom correspondence should be addressed. E-mail: john_papanikolas@unc.edu.
† Present address: Los Alamos National Laboratory MS A127, Los Alamos, NM 87545.

(1) Friedman, A. E.; Chambron, J. C.; Sauvage, J. P.; Turro, N. J.; Barton, J. K. *J. Am. Chem. Soc.* **1990**, *112*, 4960−4962.
(2) Jenkins, Y.; Friedman, A. E.; Turro, N. J.; Barton, J. K. *Biochemistry* **1992**, *31*, 10809−10816.
(3) Turro, C.; Bossmann, S. H.; Jenkins, Y.; Barton, J. K.; Turro, N. J. *J. Am. Chem. Soc.* **1995**, *117*, 9026−9032.
(4) Holmlin, R. E.; Stemp, E. D. A.; Barton, J. K. *Inorg. Chem.* **1998**, *37*, 29−34.
(5) Sabatani, E.; Nikol, H. D.; Gray, H. B.; Anson, F. C. *J. Am. Chem. Soc.* **1996**, *118*, 1158−1163.
(6) Chang, Q.; Murtaza, Z.; Lakowicz, J. R.; Rao, G. *Anal. Chim. Acta* **1997**, *350*, 97−104.
(7) Guo, X. Q.; Castellano, F. N.; Li, L.; Lakowicz, J. R. *Biophys. Chem.* **1998**, *71*, 51−62.
(8) Ling, L. S.; He, Z. K.; Song, G. W.; Han, H. Y.; Zhang, H. S.; Zeng, Y. E. *Mikrochim. Acta* **2000**, *134*, 57−62.
(9) Ling, L. S.; He, Z. K.; Song, G. W.; Zeng, Y. E.; Wang, C.; Bai, C. L.; Chen, X. D.; Shen, P. *Anal. Chim. Acta* **2001**, *436*, 207−214.
(10) Ling, L. S.; Song, G. W.; He, Z. K.; Liu, H. Z.; Zeng, Y. *Microchem. J.* **1999**, *63*, 356−364.
(11) Chambron, J. C.; Sauvage, J. P. *Chem. Phys. Lett.* **1991**, *182*, 603−607.
(12) Nair, R. B.; Cullum, B. M.; Murphy, C. J. *Inorg. Chem.* **1997**, *36*, 962−965.
(13) Olson, E. J. C.; Hu, D.; Hormann, A.; Jonkman, A. M.; Arkin, M. R.; Stemp, E. D. A.; Barton, J. K.; Barbara, P. F. *J. Am. Chem. Soc.* **1997**, *119*, 11458−11467.
(14) Coates, C. G.; Callaghan, P. L.; Mcgarvey, J. J.; Kelly, J. M.; Kruger, P. E.; Higgins, M. E. *J. Raman Spectrosc.* **2000**, *31*, 283−288.

10.1021/ja0279139 CCC: $22.00

this state reversal, excited-state relaxation is believed to progress rapidly through these two states to produce a quasi charge-separated state from which fast nonradiative relaxation back to the ground state occurs. The presence of two distinct states on the dppz ligand is supported by low-level molecular orbital calculations, electrochemical measurements on the ground-state complex, and recent ultrafast experiments.[13,15−21] While there is some evidence indicating that the dark state is localized primarily on the phz portion of the ligand, the connection of the bright state with the bpy fragment has not been experimentally confirmed, and a detailed description of the mechanism that leads to the light-switch behavior has remained elusive.

In this report, we describe temperature-dependent excited-state lifetime measurements on $[Ru(bpy)_2dppz]^{2+}$ in both protic and aprotic solvents. These experiments yield a unifying picture of the excited-state photophysics that accounts for observations in both types of solvent. Not only do our measurements support the notion of bpy-like and phz-like states associated with the dppz ligand, but they also suggest that the bpy-like state is photophysically similar to the ^{3}MLCT state in $[Ru(bpy)_3]^{2+}$. In contrast to the current thinking, the experiments presented here suggest that the dark (phz) state is always lowest in energy (even in aprotic solvents) and that the light-switch behavior is not driven by a state reversal but is governed by a competition between energetic factors that favor the dark (phz) state and entropic factors that favor the bright (bpy) state. These results also speak to the control of charge flow in molecular systems and point out that the excited-state charge distribution is dictated not just by excited-state energetics, but also by entropic factors. Such issues may become important in the design of functional electronic materials based on molecular systems, where the location of excited-state charge must be controlled.

II. Experimental Section

Time-resolved measurements were conducted by time-correlated single photon counting (TCSPC). Picosecond laser pulses are produced by a mode-locked Ti:Sapphire laser whose output is frequency doubled to 423 nm. The repetition rate is selected to be at least 5 times the natural lifetime of the sample (190 kHz) using an acoustooptic modulator (AOM). After the AOM, the beam passes through an iris and illuminates, without focusing, a 10 mm quartz cuvette containing the sample. The emitted light is collected at 90° and focused onto the slit of a 240 mm focal length, single grating monochromator and subsequently delivered to a cooled, multichannel plate-photomultiplier tube (MCP, Hamamatsu R3809U-51). The intensity of the detected luminescence is varied by use of neutral density filters mounted before the monochromator. The signal from the MCP is amplified prior to sending it into a 200 MHz constant fraction discriminator (CFD, Tennelec 454) whose output serves as the start pulse for a time-to-amplitude converter (TAC, Tennelec 864). The stop pulse is obtained by focusing 10% of the excitation beam onto a Si:PIN photodiode, whose output is sent into a variable delay box, then to a CFD, and finally to the TAC. The TAC's output is sent to a multichannel analyzer that is interfaced to a PC. The instrument response of the apparatus is 80 ps at the fwhm.

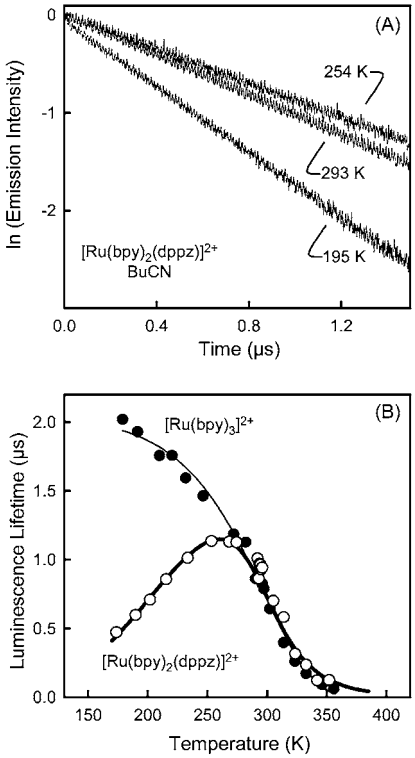

Figure 2. (a) Decay in luminescence intensity at 620 nm for $[Ru(bpy)_2dppz]^{2+}$ in butyronitrile (BuCN) at three different temperatures. Excitation was at 423 nm. (b) Compilation of luminescence lifetimes as a function of temperature for $[Ru(bpy)_2dppz]^{2+}$ (○) and $[Ru(bpy)_3]^{2+}$ (●), also in BuCN. At all temperatures, BuCN presented is a liquid. The solid line through the $[Ru(bpy)_2dppz]^{2+}$ data is the result of a fit to the equilibrium model described in the text.

The sample temperature was varied using a homemade cryostat. The sample cuvette was placed in a quartz dewar. To cool the sample, nitrogen gas was passed through a coil submersed in liquid nitrogen and then into the dewar. The temperature of the sample was varied by altering the flow rate of the gaseous nitrogen and monitored using a thermocouple attached to the cuvette. Above 298 K, the sample temperature was controlled using a circulating water bath that warmed the cuvette holder.

The $[Ru(bpy)_2dppz](PF_6)_2$ and $[Ru(dppz)_3](PF_6)_2$ compounds were synthesized using methods described previously.[17,22] All solvents were distilled prior to use, and the samples were Ar sparged to remove dissolved oxygen. Sample concentrations used in the emission experiments were $\sim 10^{-5}$ M, as determined by absorbance measurements.

III. Results and Discussion

In room-temperature nitrile solvents, $[Ru(bpy)_2dppz]^{2+}$ is brightly luminescent with a steady-state emission spectrum centered around 620 nm. The luminescent state is ^{3}MLCT in character and localized on the dppz ligand. This paper focuses on the emission lifetime as a function of temperature.

The decay in the luminescence intensity of $[Ru(bpy)_2dppz]^{2+}$ in liquid butyronitrile (BuCN) is displayed in Figure 2A. Three transients are shown,[23] each corresponding to a different temperature. All are single exponential. The excited-state

(15) Fees, J.; Ketterle, M.; Klein, A.; Fiedler, J.; Kaim, W. *J. Chem. Soc., Dalton Trans.* **1999**, *15*, 2595−2599.
(16) Fees, J.; Kaim, W.; Moscherosch, M.; Matheis, W.; Klima, J.; Krejcik, M.; Zalis, S. *Inorg. Chem.* **1993**, *32*, 166−174.
(17) Amouyal, E.; Homsi, A.; Chambron, J. C.; Sauvage, J. P. *J. Chem. Soc., Dalton Trans.* **1990**, *6*, 1841−1845.
(18) Coates, C. G.; Olofsson, J.; Coletti, M.; Mcgarvey, J. J.; Onfelt, B.; Lincoln, P.; Norden, B.; Tuite, E.; Matousek, P.; Parker, A. W. *J. Phys. Chem. B* **2001**, *105*, 12653−12664.
(19) Coates, C. G.; Callaghan, P.; Mcgarvey, J. J.; Kelly, J. M.; Jacquet, L.; Mesmaeker, A. K. *J. Mol. Struct.* **2001**, *598*, 15−25.
(20) Ujj, L.; Coates, C. G.; Kelly, J. M.; Kruger, P. E.; Mcgarvey, J. J.; Atkinson, G. H. *J. Phys. Chem. B* **2002**, *106*, 4854−4862.
(21) Onfelt, B.; Lincoln, P.; Norden, B.; Baskin, J. S.; Zewail, A. H. *Proc. Natl. Acad. Sci. U.S.A.* **2000**, *97*, 5708−5713.
(22) Ackermann, M. N.; Interrante, L. V. *Inorg. Chem.* **1984**, *23*, 3904.
(23) Fleming, C. N.; Maxwell, K. A.; Meyer, T. J.; Papanikolas, J. M. *J. Am. Chem. Soc.* **2001**, *123*, 10336−10347.

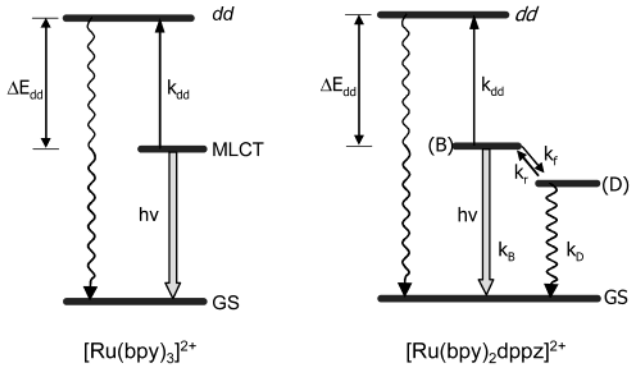

Figure 3. Energy level diagrams depicting excited states of $[Ru(bpy)_3]^{2+}$ and $[Ru(bpy)_2dppz]^{2+}$. (B) and (D) refer to the bright and dark states described in the text. Both are MLCT states associated with the dppz ligand. The bright state, (B), is entropically favored and thus is populated at high temperatures. The dark state, (D), is energetically favored and is therefore populated at low temperatures. In this scheme, k_B is the total relaxation rate, which reflects both radiative and nonradiative deactivation pathways. While k_D is taken to be largely nonradiative, it may have a small radiative component, as is evidenced by the observation of a short-lived red-shifted emission band in water.[13]

lifetime has a clear dependence on the sample temperature, increasing from 970 to 1130 ns as the system is cooled from 293 to 254 K. This increase is consistent with a large number of Ru(II) complexes (including $[Ru(bpy)_3]^{2+}$) that show similar behavior. However, unlike other Ru(II) compounds, a rollover in lifetime is observed as the system is cooled below 254 K, and by 195 K, the lifetime is only 595 ns.

As a benchmark for comparison, we have performed a similar series of measurements on $[Ru(bpy)_3]^{2+}$ (Figure 2B). At high temperatures, the excited-state lifetimes for $[Ru(bpy)_3]^{2+}$ and $[Ru(bpy)_2dppz]^{2+}$ are nearly identical. This is not the case below 250 K. While the $[Ru(bpy)_2dppz]^{2+}$ lifetime decreases, the $[Ru(bpy)_3]^{2+}$ lifetimes show a continual increase. These observations are inconsistent with the current photophysical model for $[Ru(bpy)_2dppz]^{2+}$, which has the dark state higher in energy than the bright state in aprotic solvents. If this were the case, then the photophysical behavior of $[Ru(bpy)_2dppz]^{2+}$ should be more like $[Ru(bpy)_3]^{2+}$ at *low* temperatures, not high temperatures as is observed. In short, our data indicate that the dark state is lowest in energy, even in aprotic solvents.

To decipher the temperature dependence observed in the $[Ru(bpy)_2dppz]^{2+}$ complex, we must first understand the photophysical factors that give rise to the temperature dependence in $[Ru(bpy)_3]^{2+}$. These factors are well documented.[24−27] At elevated temperatures, the lifetime is influenced by metal-centered dd states situated 3000−3500 cm^{-1} above the ^{3}MLCT state (Figure 3). Thermal population of these states leads to rapid nonradiative decay to the ground state. The presence of this additional deactivation pathway causes the lifetime to decrease as the temperature is increased above room temperature. At low temperatures, where thermal activation of the dd states is insignificant, the natural lifetime is determined by the population distribution in a manifold of low-energy ^{3}MLCT states.[28,29] Change in the population of these states with temperature leads to a gradual increase in the excited-state lifetime as the temperature is decreased. As a result of these factors, at both high and low temperatures the lifetime of $[Ru(bpy)_3]^{2+}$ increases as the temperature is decreased. This is true not only for $[Ru(bpy)_3]^{2+}$, but for a large number of polypyridyl Ru(II) compounds.

The rollover in the $[Ru(bpy)_2dppz]^{2+}$ lifetimes (Figure 2B) is attributed to a dynamical interaction between a bright state (B) and a lower energy dark state (D). A diagram depicting these states is illustrated in Figure 3. Single-exponential decay kinetics are observed at all temperatures, consistent with a constant equilibrium between B and D. Recent ultrafast experiments support the notion of a rapid interconversion between these two states.[13,18] In particular, they show a fast (<20 ps) kinetic component that could correspond to the time it takes to establish the equilibrium populations. Although the kinetics of this equilibrium are certainly relevant to the photophysics, the light-switch mechanism itself is dictated by the thermodynamics of this equilibrium.

We have modeled the $[Ru(bpy)_2dppz]^{2+}$ lifetime data using the kinetic scheme depicted in Figure 3. Our goal is not to extract exact values for the various rate constants − there are too many unknowns, and the model is too simple[30] − but rather to demonstrate that this kinetic model accounts (at least qualitatively) for the general features of the data. If the bright and dark states are in constant equilibrium, then the observed lifetime ($1/k_{obs}$) can be written as a population-weighted average of the decay rates for the two excited states:

$$k_{obs} = \rho_B(k_B + k_{dd}(T)) + \rho_D k_D \qquad (1)$$

where ρ_B and ρ_D are the relative populations in the bright and dark states, k_B and k_D are their relaxation rates back to the ground state, and k_{dd} is the rate constant for deactivation via the dd state. The emission lifetimes of $[Ru(bpy)_2dppz]^{2+}$ and $[Ru(bpy)_3]^{2+}$ above 300 K are nearly indistinguishable. This suggests that the bright state in $[Ru(bpy)_2dppz]^{2+}$ and the MLCT state in $[Ru(bpy)_3]^{2+}$ are photophysically similar. (This is discussed in more detail later.) It also suggests that the excited-state population in $[Ru(bpy)_2dppz]^{2+}$ is completely shifted toward the bright state at high temperatures, that is, $\rho_B \gg \rho_D$.

The relative populations can be expressed in terms of the B ⇔ D equilibrium constant, that is

$$K_{EQ} = \frac{\rho_D}{\rho_B} = \exp\left(-\frac{\Delta G}{k_B T}\right) = \exp\left(-\frac{\Delta H - T\Delta S}{k_B T}\right) \qquad (2)$$

where ΔH and ΔS are the enthalpy and entropy changes for the B → D process. The dark state is enthalpically favored (ΔH

(24) Lumpkin, R. S.; Kober, E. M.; Worl, L. A.; Murtaza, Z.; Meyer, T. J. *J. Phys. Chem.* **1990**, *94*, 239−243.
(25) Durham, B.; Caspar, J. V.; Nagle, J. K.; Meyer, T. J. *J. Am. Chem. Soc.* **1982**, *104*, 4803−4810.
(26) Barigelletti, F.; Juris, A.; Balzani, V.; Belser, P.; Zelewsky, A. *Inorg. Chem.* **1983**, *22*, 3335−3339.
(27) Van Houten, J.; Watts, R. J. *J. Am. Chem. Soc.* **1976**, *98*, 4853−4858.

(28) There are four low-lying triplet states lying within 500 cm^{-1} of each other. The amount of singlet character increases from 0% for the lowest state to about 40% for the highest, and thus the higher energy states have shorter radiative lifetimes. Because the four ^{3}MLCT states are in rapid equilibrium, the emission intensity decays with single-exponential kinetics, and the lifetime is a Boltzmann-weighted average of the lifetimes of the different states. Therefore, as the temperature is decreased and the distribution shifts to lower energy, the excited-state lifetime increases.

(29) Kober, E. M.; Meyer, T. J. *Inorg. Chem.* **1984**, *23*, 3877−3887.

(30) The kinetic model shown in Figure 3 does not include low-lying triplets such as those found in $[Ru(bpy)_3]^{2+}$, but instead treats the bright state (B) as a single MLCT state. Although the lowest three MLCT states in $[Ru(bpy)_3]^{2+}$ can be treated as a single state at these temperatures, the presence of the fourth MLCT state does contribute to the temperature dependence. Complications arising from additional low-lying states in the MLCT manifold of $[Ru(bpy)_2dppz]^{2+}$ could be present, and they are not accounted for in the model.

< 0), even in aprotic solvents, and at low temperatures the population resides in that state (i.e., $K_{EQ} \gg 1$). As the temperature is increased, the population in the bright state increases, corresponding to a decrease in K_{EQ}. If ΔS is *positive*, the population in the dark state will always be larger than the bright state (i.e., $\rho_D > \rho_B$), and thus a complete shift in the population will not occur. To shift the entire population to the bright state, ΔS must be *negative*. Thus, while the dark state is always energetically preferred, the bright state is entropically favored and thus dominates at high temperatures. Lower entropy might be expected for the dark state because the greater amount of charge separation could induce more order in the surrounding solvent. We must point out that, in principle, our observations could stem from the temperature dependence of ΔH. This would arise from a difference in heat capacities between the reactants and products, ΔC_p. Because the "reaction" corresponds to the motion of charge from one portion of the dppz ligand to another, ΔC_p is most likely small, and, for this reason, we dismiss it as the source of the observed temperature dependence.

We have used eqs 1 and 2 to model our data numerically. In this analysis, the relaxation rates, k_B and k_D, are approximated to be temperature independent,[31,32] and k_{dd} is written using the usual Arrhenius type expression, that is, $k_{dd}(T) = A \exp(-\Delta E_{dd}/k_B T)$. The values for A and ΔE_{dd} are obtained from an analysis of the high-temperature lifetime data. They were determined from the $[Ru(bpy)_3]^{2+}$ data to be 6.0×10^{12} s^{-1} and 3200 cm^{-1}, respectively; both agree well with values measured by other groups.[24,33,34] The solid line shown in Figure 2B corresponds to the lifetimes (k_{obs}^{-1}) calculated[35] using eqs 1 and 2 with $\Delta H = -790$ cm^{-1}, $\Delta S = -5$ cm^{-1}/K, $k_B = (1800 \text{ ns})^{-1}$, and $k_D = (160 \text{ ns})^{-1}$.

As a further test of this model, we have examined the excited-state photophysics of the $[Ru(bpy)_2(dppz)]^{2+}$ complex in other solvents. Figure 4A shows lifetime data obtained in BuCN, MeCN (acetonitrile), and MeOH (methanol). The excited-state lifetime in methanol is greatly reduced, consistent with observations made by other groups.[1,12] Interestingly, in the alcohol solvent the lifetime increases with temperature between 230 and 308 K. In the case of methanol, and probably other protic solvents as well, it appears that the preferential stabilization of the dark state is so great that the temperature needed to shift the population to the bright state lies above room temperature and, in this case, above the boiling point of the solvent too.

The relative population of the bright and dark states (i.e., the light-switch) is the result of a competition between enthalpic (ΔH) and entropic ($-T\Delta S$) contributions to the total free energy, ΔG. To illustrate this, the equilibrium constant, K_{EQ}, is shown as a function of temperature in Figure 5 for different values of ΔH. Because ΔS is *negative*, K_{EQ} changes from values that exceed unity at low temperatures (dark state populated) to values that are less than 1 at high temperatures (bright state populated).

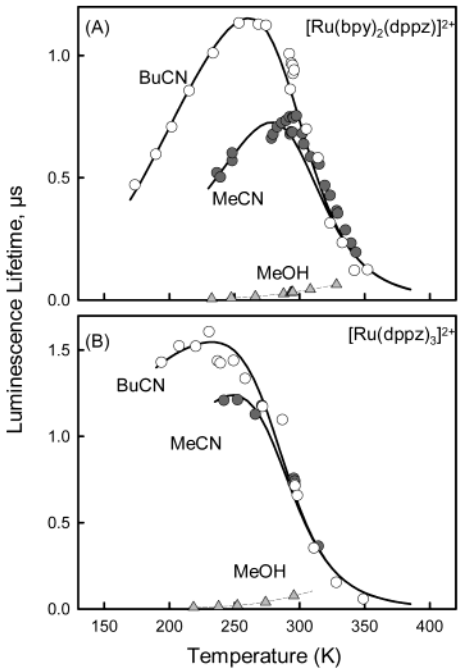

Figure 4. Excited-state lifetimes as a function of temperature in butyronitrile (BuCN), acetonitrile (MeCN), and methanol (MeOH). Panels A and B contain data for $[Ru(bpy)_2dppz]^{2+}$ and $[Ru(dppz)_3]^{2+}$, respectively. The solid lines drawn through the nitrile data are from eqs 1 and 2.

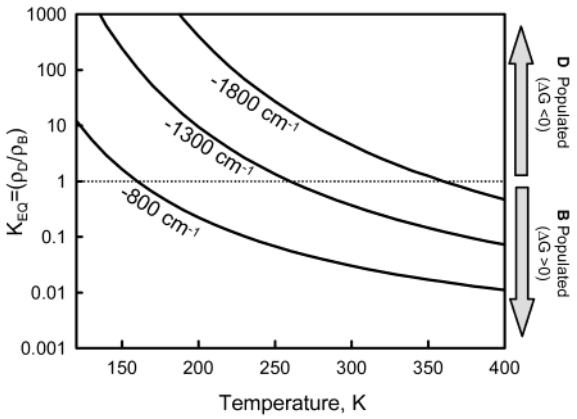

Figure 5. Equilibrium constant (K_{EQ}) as a function of temperature for different values of ΔH. K_{EQ} was calculated using $\Delta H = -1800$ cm^{-1} and -800 cm^{-1} and $\Delta S = -5$ cm^{-1}. The smaller ΔH value approximates that obtained from the analysis of our data in BuCN, an aprotic solvent. The larger values are likely comparable to those obtained in protic solvents.

If ΔS were positive, K_{EQ} would be greater than 1 at all temperatures. In aprotic environments, the energy gap is small, and the minimum temperature needed to drive the equilibrium toward the bright state lies *below* room temperature. In protic solvents, the preferential stabilization of the dark state increases the energy gap and shifts the inversion point *above* room temperature. The light-switch effect is observed at room temperature, where the vast majority of measurements have been performed, because the entropy term dominates in aprotic solvents, and the energetic term dominates in protic ones.

The effect of solvent polarity on the light-switch mechanism can also be understood in the context of this equilibrium model. The luminescence lifetimes obtained in MeCN show an inversion temperature at approximately 290 K, as compared to 260 K in BuCN, suggesting that the energy gap in MeCN is greater

(31) There is some justification for this approximation based on earlier work (ref 32) showing that the nonradiative rate constant is relatively temperature independent.
(32) Claude, J. P.; Meyer, T. J. *J. Phys. Chem.* **1995**, *99*, 51−54.
(33) Cherry, W. R.; Henderson, L. J., Jr. *Inorg. Chem.* **1984**, *23*, 983.
(34) Wacholtz, W. F.; Auerbach, R. A.; Schmehl, R. H. *Inorg. Chem.* **1986**, *25*, 227.
(35) A nonlinear least-squares fit to eqs 1 and 2 was not possible due to a high correlation between several of the parameters. This problem could be solved by collecting data at lower temperatures, where the lifetime should approach a limiting value of $1/k_D$. However, we are prevented from doing this because of the freezing of the solvent. The solid lines in Figures 2 and 4 represent the best fits to the experimental data as determined by visual inspection.

than that in BuCN. Our model shows that a small change in the energy gap can have a profound effect on the equilibrium. The solid line drawn through the MeCN data was obtained from eqs 1 and 2 simply by increasing the energy gap from −790 cm^{-1} (the value used for the BuCN data) to −1010 cm^{-1}. The values for all other parameters were held constant.

The origin of the electrostatic stabilization most likely stems from the differences in the charge distribution for the bright and dark states. If the charge distribution in the dark state is located primarily on the phz portion of the ligand, then it will have a greater excited-state dipole moment than the bright state. Thus, when the polarity of the solvent is increased, the dark state will experience greater stabilization and lead to a larger energy gap. The notion of an extended charge distribution in the dark state and a more compact charge distribution in the bright state has been proposed before.[15−17] However, our experiments go a step further and suggest that the excited-state charge distribution in the bright state is similar in size to that present in the ^{3}MLCT state of $[Ru(bpy)_3]^{2+}$.

The similarity in photophysical behavior at high temperatures places the bright state in $[Ru(bpy)_2dppz]^{2+}$ at an energy similar to that of the ^{3}MLCT state in $[Ru(bpy)_3]^{2+}$, at least with respect to its location relative to the dd states. Analysis of the high-temperature data suggests that the energy gap between the ^{3}MLCT and dd states is about 3100 cm^{-1} in $[Ru(bpy)_2dppz]^{2+}$ and about 3200 cm^{-1} in $[Ru(bpy)_3]^{2+}$. The energy gaps are remarkably similar, especially when compared to other substituted polypyridyl Ru(II) compounds.[24,33,34] Subtle differences in the chemical structure of the polypyridyl ligand can have a substantial effect on the excited-state energetics, and energy gaps ranging from 2740 cm^{-1} in $[Ru(dmb)_3]^{2+}$ to 4230 cm^{-1} in the carboxylic acid functionalized complex, $[Ru(dcb)_3]^{2+}$, have been observed.[33,34,36] In this context, the similarity in ^{3}MLCT/dd energy gaps for $[Ru(bpy)_2dppz]^{2+}$ and $[Ru(bpy)_3]^{2+}$ is rather remarkable given the vastly different chemical structures of the two ligands. The logical conclusion is that the electron distribution in the bright state is similar to that in the ^{3}MLCT state of $[Ru(bpy)_3]^{2+}$.

On the basis of the $[Ru(bpy)_2dppz]^{2+}$ and $[Ru(bpy)_3]^{2+}$ data alone, the simplest interpretation of this observation is that the bright state is localized on one of the two bpy ligands and the dark state is associated with the dppz ligand. If this were true, however, then qualitatively different photophysical behavior would be expected for $[Ru(dppz)_3]^{2+}$, which has no bpy ligands and hence cannot support such an equilibrium. Lifetime measurements for $[Ru(dppz)_3]^{2+}$ are shown in Figure 4B. The $[Ru(bpy)_2dppz]^{2+}$ and $[Ru(dppz)_3]^{2+}$ complexes exhibit similar trends in all three solvents, indicating that the same dynamical process is occurring in both complexes. In other words, both the bright and the dark states must be associated with the dppz ligand, implying that the $[Ru(bpy)_2dppz]^{2+}$ complex could be described as a $[Ru(bpy)_3]^{2+}$ core and a phz charge acceptor.

Acknowledgment. This project was supported by DOE grant DE-FG02-96ER 14607, Research Corp. Award RI0048, and Petroleum Research Fund grant 36385-G6. We also thank Dr. Dan Allen Myers from Kinston, North Carolina, whose gift to the UNC-CH Faculty Partners Fund also provided support.

JA0279139

(36) dmb = (4,4′-dimethyl-2,2′-bipyridine); dcb = (4,4′-dicarboxylate-2,2′-bipyridine).

$[Ru(bpy)_2dppz]^{2+}$ Light-Switch Mechanism in Protic Solvents as Studied through Temperature-Dependent Lifetime Measurements†

Matthew K. Brennaman, Thomas J. Meyer, and John M. Papanikolas*

The Venable and Kenan Laboratories, Department of Chemistry, University of North Carolina at Chapel Hill, Chapel Hill, North Carolina 27599

Received: May 12, 2004; In Final Form: July 16, 2004

Temperature-dependent excited-state lifetime measurements have been performed on four different Ru(II)-based dppz compounds in protic and aprotic solvents. This work supports the existence of a dynamic equilibrium between two MLCT states associated with the dppz ligand: one is a bright state with a ligand orbital similar in size to that associated with the ^{3}MLCT state of $[Ru(bpy)_3]^{2+}$, and the other is a dark phz-like state. Our results are consistent with a light-switch mechanism involving a competition between energetic factors that favor the dark (phz) state and entropic factors that favor the bright (bpy) state. This paper explores the photophysics of these light-switch compounds through a systematic variation of the equilibrium energetics. This is accomplished by (1) varying the dielectric strength of the solvent and (2) making chemical substitutions on the dppz ligand. Observations obtained from all four compounds in six different solvents can be explained using this equilibrium model.

I. Introduction

The polypyridyl Ru(II) compound $[Ru(bpy)_2dppz]^{2+}$ (Figure 1) has been identified as a luminescent probe of many aprotic environments,[1−3] including polymer films, micelles, and DNA. In aqueous solution, $[Ru(bpy)_2dppz]^{2+}$ is essentially nonemissive; however, in the presence of DNA, the molecule intercalates between adjacent base pairs in the double helix and becomes brightly luminescent.[4−9] This behavior, called the "light-switch" effect, is the basis for use of this compound as a probe of nonpolar microenvironments. As it turns out, DNA is not the only environment in which $[Ru(bpy)_2dppz]^{2+}$ emits, and luminescent excited states are observed in many protic and aprotic solvents. Because of their useful applications and unique photophysical properties, dppz-containing molecules have been studied in a range of solvents with the goal of understanding the origin of their emission.[10−15]

The light-switch mechanism has been attributed to the presence of two metal-to-ligand charge-transfer (MLCT) states on the dppz ligand: a bright (luminescent) state associated with the bipyridine (bpy) fragment and a dark (nonluminescent) state localized largely on the phenazine (phz) portion.[16] According to this model, the bright state is lowest in energy for aprotic solvents resulting in an emissive excited state. Protic solvents, on the other hand, hydrogen bond to the phz nitrogens, lower the energy of the dark state below that of the bright state, and shut off the luminescence. Although this environment-induced state reversal has been suggested as the basis for the light-switch property, direct confirmation has been elusive.

Our research effort concurs with the existence of two states associated with the dppz ligand: a dark phenazine-based state and a luminescent $[Ru(bpy)_3]^{2+}$-like ^{3}MLCT state. However, our data are inconsistent with the state reversal description of the light-switch behavior. Instead, the results of temperature dependence measurements show that, in $[Ru(bpy)_2dppz]^{2+}$, the dark state is always lowest in energy and the light-switch behavior is the result of a dynamic equilibrium between an enthalpically favored dark state and an entropically favored bright state.[17,18] A diagram depicting these states is presented in Figure 2. Lifetime data obtained at high temperatures indicate

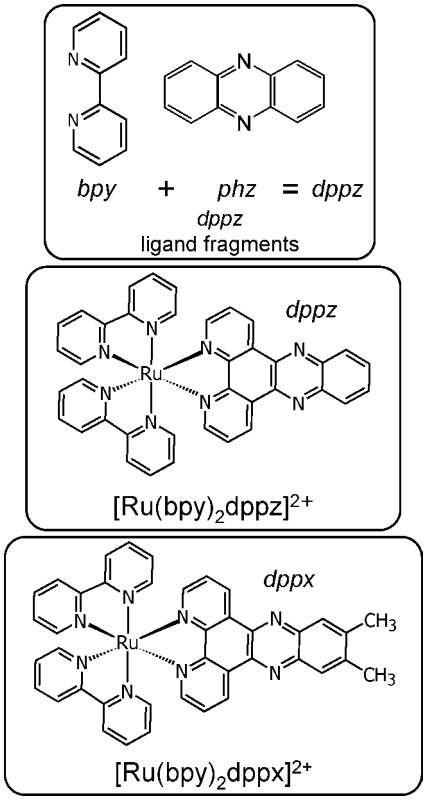

Figure 1. Chemical structures of light-switch complexes $[Ru(bpy)_2dppz]^{2+}$ and $[Ru(bpy)_2dppx]^{2+}$ and ligand fragments discussed in the text.

† Part of the special issue "Tomas Baer Festschrift".

* To whom correspondence should be addressed. E-mail: John_Papanikolas@unc.edu.

10.1021/jp0479670 CCC: $27.50
Published on Web 10/05/2004

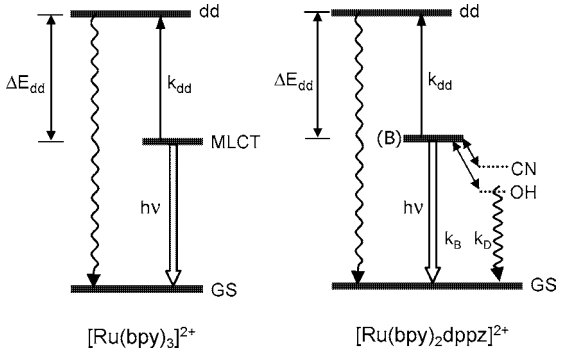

Figure 2. Energy level diagrams depicting the excited states of [Ru(bpy)$_2$dppz]$^{2+}$ and [Ru(bpy)$_3$]$^{2+}$. The bright state described in the text is denoted by B, and both OH and CN refer to the dark state. The dark state for protic solvents is represented by OH, whereas CN corresponds to the dark state in aprotic solvents. All three are MLCT states associated with the dppz ligand. The bright state, B, is entropically favored and is populated at high temperatures. The dark state is enthalpically favored and is therefore populated at low temperatures. In this scheme, k_B is the relaxation rate from the bright state, and k_D is the relaxation rate from the dark state.

that the bright state is an MLCT state in which the photoexcited electron is located on the bpy fragment of the dppz ligand. Measurements performed in different solvents provide an indication as to the nature of the dark state. They suggest that it has a greater degree of charge-transfer character than the bright state. On this basis, we assign it to an MLCT state in which the electron is localized more on the phz portion of the dppz ligand. Thus, the equilibrium corresponds to the transfer of the photoexcited electron between the inner and outer portions of the dppz ligand. Qualitatively speaking, our model describes the [Ru(bpy)$_2$dppz]$^{2+}$ complex as consisting of a [Ru(bpy)$_3$]$^{2+}$ core and a phz charge-acceptor.

This paper expands upon our previous work in two ways. We examine the luminescent properties of [Ru(bpy)$_2$dppz]$^{2+}$ in a series of linear alcohols. As observed in nitrile solvents, the photophysics in alcohols also appears to be governed by an excited-state equilibrium. Experiments performed in a range of solvents (protic and aprotic) suggest that several properties connected with the dark state correlate with the degree of solvent polarity. In particular, increasing the solvent polarity preferentially stabilizes the dark-state energy and increases the rate of nonradiative relaxation, the latter being consistent with observations made by Murphy and co-workers.[13] This correlation with the solvent dielectric strength strongly supports our contention that the dark state has significant charge-transfer character, in contrast to a recent theoretical calculation that the dark state is a ligand-centered $^3\pi\pi^*$ state.[19] We also examine a complex with a chemically modified dppz ligand, i.e., [Ru(bpy)$_2$dppx]$^{2+}$, where the addition of electron-donating methyl substituents destabilizes the π^* orbitals and pushes the phz state higher in energy. The effect of this substitution is clear in the experimental data. This equilibrium description of the light-switch mechanism accounts for a wide range of observations across multiple dppz-containing Ru(II) compounds in a series of solvents with differing chemical character and polarity.

II. Experimental Description

The time-resolved emission experiments were conducted by time-correlated single photon counting (TCSPC). Briefly, the 846-nm output from a mode-locked Ti:sapphire oscillator (Spectra Physics Tsunami) is frequency doubled in a BBO crystal to produce ~1-ps pulses at 423 nm with a pulse energy of ~0.2 nJ/pulse. The repetition rate of the 76-MHz pulse train is reduced using an acoustooptic modulator such that the time between excitation pulses is at least 5 times the natural lifetime of the sample (usually between 5 and 10 μs). Emission is collected at 90° with respect to excitation, passed through a 0.25-m monochromator and is directed onto a microchannel plate photomultiplier tube (MCP−PMT). The details regarding the TCSPC electronics are described elsewhere.[17,20] The instrument response is measured to be approximately 80 ps, fwhm.

Emission measurements were performed at a series of temperatures. Control over the sample temperature was achieved in one of two ways. Below 273 K, the temperature was maintained using a liquid-nitrogen-cooled cryostat (Janis 6NDT) with feedback controlling electronics that kept temperatures within ±0.1 K of the desired temperature. Above 273 K, a circulating water bath was used. The [Ru(bpy)$_2$dppz]$^{2+}$, [Ru(dppz)$_3$]$^{2+}$, [Ru(bpy)$_2$dppx]$^{2+}$, and [Ru(dppx)$_3$]$^{2+}$ complexes were synthesized per previous methods by our laboratory.[10,21] The (PF_6^-) salt of each complex was used for nitrile solvents, whereas the (Cl^-) salt was used for the alcohols.

III. Results and Discussion

This part of the paper is divided into four sections. In section A, we present steady-state spectroscopic data on [Ru(bpy)$_2$dppz]$^{2+}$ in ethanol (EtOH) at and below 298 K. Section B examines the temperature dependence of the luminescence lifetime in fluid solution. These experiments reveal the presence of a temperature-dependent equilibrium between a bright state (B) and a dark state (D). Both the high-temperature transients and the steady-state spectra at room temperature and in the low-temperature glass show that the bright state in [Ru(bpy)$_2$dppz]$^{2+}$ is photophysically similar to the ^{3}MLCT state in [Ru(bpy)$_3$]$^{2+}$. Section C extends the temperature dependence studies to other alcohol solvents and reveals that the luminescence properties correlate with the solvent polarity, suggesting that the dark state has significant charge-transfer character. Finally, section D examines the chemically modified compound [Ru(bpy)$_2$dppx]$^{2+}$, demonstrating that the equilibrium energetics can be tuned through chemical substitution.

A. [Ru(bpy)$_2$dppz]$^{2+}$ Steady-State Spectroscopy. There are at least three low-lying electronic states in [Ru(bpy)$_2$dppz]$^{2+}$ that have been postulated to play a role in determining its excited-state photophysical properties. Two are ^{3}MLCT states that correspond to the electron being localized separately on the bpy and phz fragments of the dppz ligand and the third is a long-lived, ligand-centered $^3\pi\pi^*$ state. In protic solvents, both the $^3\pi\pi^*$ and MLCT states have been observed in the *fac*-[Re(dppz)(CO)$_3$(Cl)] complex.[11] The state ordering in that complex depends on the rigidity of the solvent, with the emissive ^{3}MLCT state being lowest in fluid solutions and the $^3\pi\pi^*$ state being lowest in low-temperature glasses. The origin of this emission behavior is easily explained. In rigid environments (e.g., a 77 K glass), the solvent is frozen in a configuration appropriate for the ground electronic state, and the $^3\pi\pi^*$ state is lowest in energy. The state ordering is reversed in fluid solution, where the solvent reorganizes to stabilize the ^{3}MLCT state below the $^3\pi\pi^*$ state. Our observations indicate that, unlike *fac*-[Re(dppz)(CO)$_3$(Cl)], the luminescence in [Ru(bpy)$_2$dppz]$^{2+}$ originates from an MLCT state, both in fluid solution and in the low-temperature glass.

The basis for this conclusion comes from the steady-state emission properties, which are remarkably similar for [Ru(bpy)$_3$]$^{2+}$ and [Ru(bpy)$_2$dppz]$^{2+}$, especially given the significant

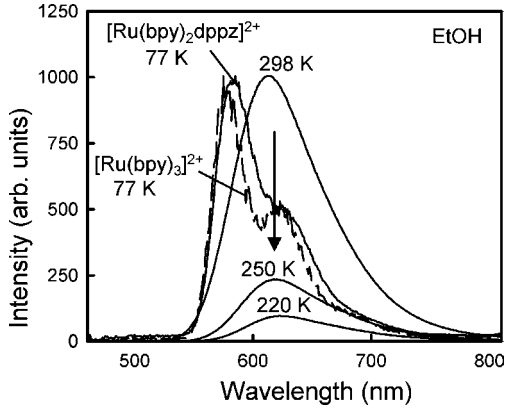

Figure 3. Steady-state emission spectra of $[Ru(bpy)_2dppz]^{2+}$ (—) in ethanol (EtOH) are shown for 77, 220, 250, and 298 K. A spectrum of $[Ru(bpy)_3]^{2+}$ (— — —) in EtOH at 77 K is also displayed for comparison.

differences in the chemical structures of the two complexes. Displayed in Figure 3 are emission spectra of $[Ru(bpy)_2dppz]^{2+}$ and $[Ru(bpy)_3]^{2+}$ in EtOH. $[Ru(bpy)_3]^{2+}$ and $[Ru(bpy)_2dppz]^{2+}$ exhibit emission spectra with similar shapes and positions at both 77 and 298 K. At 298 K, they have broad, structureless emission bands that peak at 610 nm, consistent with the assertion that both compounds are ^{3}MLCT emitters at room temperature. At 77 K, both emission bands are blue shifted to 580 nm, show vibronic structure, and exhibit similar luminescence lifetimes (5.1 and 4.8 μs for $[Ru(bpy)_3]^{2+}$ and $[Ru(bpy)_2dppz]^{2+}$, respectively). These observations indicate that the emission at 77 K does not originate from a $^3\pi\pi^*$ state, for $^3\pi\pi^*$ emission in dppz complexes occurs near 540 nm with a lifetime on the order of tens of microseconds. Instead, our data indicate that emission in $[Ru(bpy)_2dppz]^{2+}$ is from a ^{3}MLCT state that is photophysically similar to the $[Ru(bpy)_3]^{2+}$ ^{3}MLCT state, even in the low-temperature glass, and that the $^3\pi\pi^*$ state does not play a significant role.

As the temperature is decreased from room temperature, the intensity of the $[Ru(bpy)_2dppz]^{2+}$ emission band drops and continues to do so as long as the solvent remains fluid. This drop in emission intensity is the result of an excited-state equilibrium between two ^{3}MLCT states: an entropically favored *bright* state (B) localized on the bpy-fragment of the dppz ligand and an enthalpically favored *dark* state (D) localized primarily on the phz fragment. As the temperature is lowered, the entropic contribution to the free energy is diminished, and as a consequence, the population shifts from the bright state into the enthalpically favored dark state, and the emission intensity drops. Upon further cooling to 77 K, $[Ru(bpy)_2dppz]^{2+}$ becomes brightly luminescent. This reemergence of the emission stems from the rigid environment. In a 77 K glass, the solvent surrounding $[Ru(bpy)_2dppz]^{2+}$ is frozen in a configuration appropriate for the ground electronic state and is unable to reorganize structurally to solvate the charge-transfer state. In the absence of this energetic stabilization, the bright state, with its smaller excited-state dipole, is energetically favored. Because of these rigidity effects, we have chosen to focus on temperatures for which the solvent is clearly a fluid.

In fluid solution, there is no significant change in the band shape of the emission spectrum with decreasing temperature; however, there does appear to be a slight red shift (~9 nm) in the emission maximum at lower temperatures. Red shifts of this magnitude have been observed in the emission spectra of $[Ru(bpy)_3]^{2+}$ upon sample cooling for temperatures above the glass−fluid transition[22] and are attributed to the redistribution of population among the low-lying MLCT states in the triplet

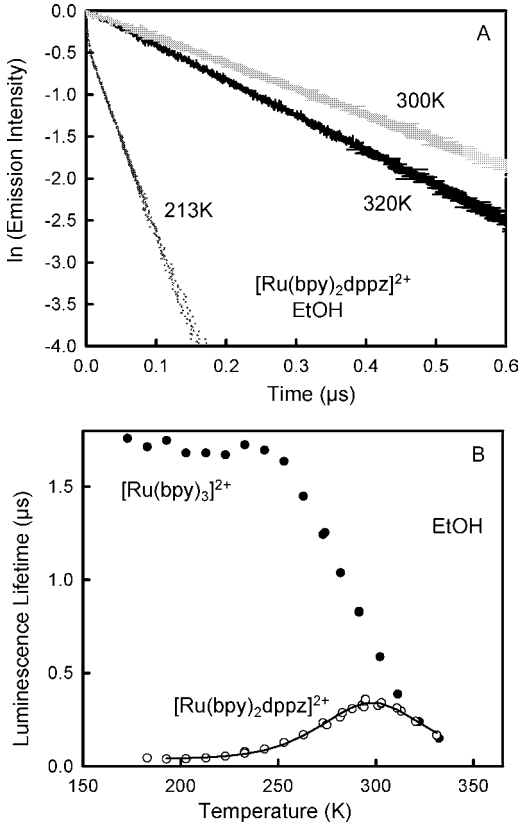

Figure 4. (A) Decay in luminescence intensity at 610 nm for $[Ru(bpy)_2dppz]^{2+}$ in EtOH at three different temperatures. Excitation was at 423 nm. (B) Compilation of luminescence lifetimes as a function of temperature for $[Ru(bpy)_2dppz]^{2+}$ (○) and $[Ru(bpy)_3]^{2+}$ (●) in EtOH. The solid line through the $[Ru(bpy)_2dppz]^{2+}$ data is the result of a fit to the equilibrium model described in the text.

manifold. Observation of a shift of the emission band in $[Ru(bpy)_2dppz]^{2+}$ might suggest that, like $[Ru(bpy)_3]^{2+}$, the bright state is composed of a set of low-lying triplet states. This would be another indicator of its photophysical similarity with the $[Ru(bpy)_3]^{2+}$ ^{3}MLCT state. We note, however, that this explanation cannot account for the substantially larger shifts (40−75 nm) recently reported[15] for $[Ru(phen)_2dppz]^{2+}$ in more viscous solvents (e.g., glycerol), thereby suggesting that (at least in some cases) multiple factors could contribute to the spectral shift. The observations made in partially frozen environments notwithstanding, the steady-state emission spectra observed in fluid solvents suggest that the luminescent state in $[Ru(bpy)_2dppz]^{2+}$ is photophysically similar to that in $[Ru(bpy)_3]^{2+}$.

B. Temperature Dependence of the Luminescence Lifetime. The presence of an excited-state equilibrium between two MLCT states is evident from the temperature dependence of the emission. The luminescence decay for $[Ru(bpy)_2dppz]^{2+}$ in EtOH is displayed at three different temperatures in Figure 4A. Just as was observed in the nitriles, the $[Ru(bpy)_2dppz]^{2+}$ emission decay obeys a single exponential; the fast component present in the data originates from a solvent impurity. The longest decay time is observed at the intermediate temperature (300 K), and at both higher and lower temperatures, the excited-state lifetime decreases.

We have made similar measurements at a series of temperatures, and the resulting lifetimes are displayed in Figure 4B. The experiments discussed in this section focus on the photophysics in the absence of rigid media effects, and thus, they are conducted at temperatures for which the solvent is a fluid.[23] Cooling the sample from 330 to 300 K increases the emission

lifetime, as expected for most Ru(II) complexes. However, just as in nitrile solvents,[17] an unexpected rollover in the excited-state lifetime is observed at 300 K, and by 180 K, the lifetime of [Ru(bpy)$_2$dppz]$^{2+}$ shortens to 40 ns. Although the details differ, this general form of temperature dependence has been observed in all solvents (alcohols and nitriles) studied to date. Önfelt et al.[14] observed a similar trend in the temperature dependence of the [Ru(phen)$_2$dppz]$^{2+}$ lifetimes in glycerol. Their data however also showed a time-dependent shift of the emission spectrum to the red that is not apparent in our data,[24] possibly due to the faster solvent reorganization time for EtOH compared to glycerol. To describe the origin of the temperature-dependent behavior in [Ru(bpy)$_2$dppz]$^{2+}$, we must first understand the effect of temperature on [Ru(bpy)$_3$]$^{2+}$.

The temperature-dependent excited-state lifetimes of [Ru(bpy)$_3$]$^{2+}$ in EtOH are shown for comparison in Figure 4B. The lifetime of [Ru(bpy)$_3$]$^{2+}$ increases as the sample is cooled over the entire temperature range studied here. This temperature dependence is well understood and arises from two different sources.[25−33] One is metal-centered dd states situated 3000−3500 cm^{-1} above the ^{3}MLCT manifold. These states provide a rapid nonradiative decay pathway to the ground state when thermally populated and, therefore, are involved primarily at elevated temperatures. At low temperatures, where the dd states are thermally inaccessible, the observed lifetime is influenced by population redistribution among the manifold of low-energy ^{3}MLCT states. As temperature decreases, the population shifts toward the lowest-energy ^{3}MLCT, which has the highest degree of triplet character and the slowest radiative relaxation rate. This redistribution leads to a gradual increase in the excited-state lifetime as the temperature is decreased. Therefore, at both high and low temperatures, the lifetime of [Ru(bpy)$_3$]$^{2+}$ increases as the temperature is decreased. These observations are typical of a large number of polypyridyl Ru(II) compounds.[28,32,34,35]

At high temperatures, the emission lifetimes of [Ru(bpy)$_2$dppz]$^{2+}$ are nearly identical to those of [Ru(bpy)$_3$]$^{2+}$; however, at temperatures below 300 K, these lifetimes decrease, whereas those for [Ru(bpy)$_3$]$^{2+}$ increase. [This rollover in lifetimes is also observed in nitriles (i.e., aprotic solvents), although the maximum lifetime in that case is observed at a slightly lower temperature.] We attribute this lifetime rollover behavior to an excited-state equilibrium between a bright state (B) and a lower energy dark state (D). A diagram representing these states is illustrated in Figure 2.

The high-temperature data provide insight into the physical nature of the bright state (B). In particular, the similarity in the lifetimes observed at high temperatures for these two compounds suggests that the bright state in [Ru(bpy)$_2$dppz]$^{2+}$ and the ^{3}MLCT state in [Ru(bpy)$_3$]$^{2+}$ are photophysically similar. Although the simplest interpretation of this statement puts the bright state on one of the two bpy ligands in the [Ru(bpy)$_2$dppz]$^{2+}$ complex, this is not the case. If it were, then qualitatively different photophysical behavior would be expected for [Ru(bpy)$_2$dppz]$^{2+}$ than for [Ru(dppz)$_3$]$^{2+}$, which has no bpy ligands and hence cannot support such an equilibrium. The lifetimes measured for the [Ru(dppz)$_3$]$^{2+}$ complex also exhibit this rollover behavior at low temperatures (Figure 5B), suggesting that the bright state is confined to the bpy fragment of the dppz ligand and is not just simply localized on one of the two ancillary bpy ligands.

We have modeled [Ru(bpy)$_2$dppz]$^{2+}$ using the kinetic scheme depicted in Figure 2. Our goal is not to extract exact values for the various rate constants—there are too many unknowns, and the model is too simple—but rather to demonstrate that this

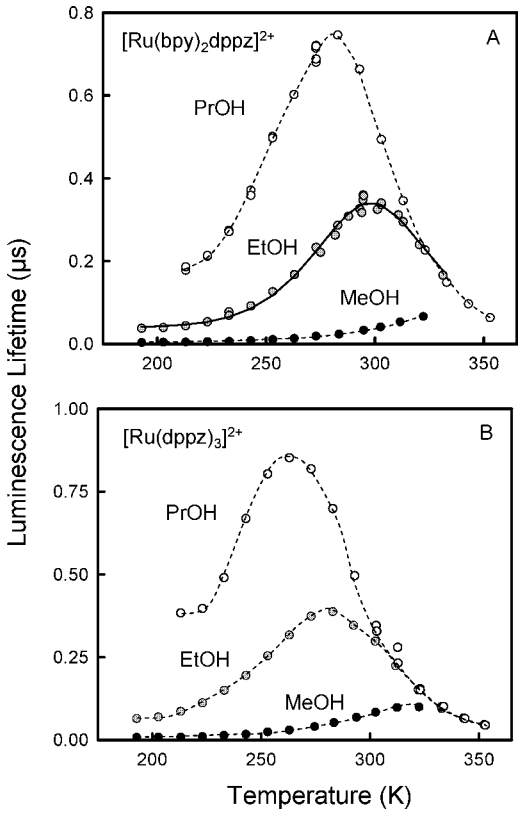

Figure 5. Excited-state lifetimes as a function of temperature in PrOH, EtOH, and MeOH for (A) [Ru(bpy)$_2$dppz]$^{2+}$ and (B) [Ru(dppz)$_3$]$^{2+}$. The solid line drawn through the EtOH data is from eqs 1 and 2; the dashed lines are included merely to guide the eye.

kinetic scheme accounts for the general features of the data. This will provide a framework from which we can predict how alterations of different system properties affect the observed signals.

If the bright and dark states are in constant equilibrium, then the observed lifetime ($1/k_{obs}$) can be written as a population-weighted average of the decay rates of the two excited states

$$k_{obs} = \rho_B[k_B + k_{dd}(T)] + \rho_D k_D \quad (1)$$

where ρ_B and ρ_D are the relative populations in the bright and dark states, respectively, and k_B and k_D are their relaxation rates back to the ground state. The rate constant for deactivation via the dd state is k_{dd}. The relative populations can be expressed in terms of the B ⇔ D equilibrium constant

$$K_{EQ} = \frac{\rho_D}{\rho_B} = \exp\left(-\frac{\Delta G^\circ}{kT}\right) = \exp\left(-\frac{\Delta H^\circ - T\Delta S^\circ}{kT}\right) \quad (2)$$

where ΔH° and ΔS° are the enthalpy and entropy changes for the B ⇔ D process.

The similarity between the [Ru(bpy)$_2$dppz]$^{2+}$ and [Ru(bpy)$_3$]$^{2+}$ photophysics indicates that, at high temperatures, there is a complete shift in the excited-state population toward the higher-energy bright state, i.e., $\rho_B \gg \rho_D$. This leads to a definitive assignment regarding the relative entropies of the two states. A complete shift in population cannot occur if ΔS° is positive because the population in the dark state would then always be larger than the population in the bright state (i.e., $\rho_D > \rho_B$); therefore, ΔS° must be negative. A more ordered solvent configuration surrounding the dark-state charge distribution is consistent with the solvent interacting with a larger dipole. Thus, whereas the dark state is enthalpically preferred (and favored

at low temperatures), the bright state is entropically favored (and dominant at high temperatures).

The temperature dependence in the lifetimes of $[Ru(bpy)_2dppz]^{2+}$ is the result of a competition between enthalpic ($\Delta H°$) and entropic ($-T\Delta S°$) contributions to the total free energy. At low temperatures, the population is shifted toward the dark state, and relaxation back to the ground state is rapid. As the temperature is increased, the entropic contribution begins to dominate, the population shifts toward the higher-energy bright state, and the photophysics shifts to mimic that of $[Ru(bpy)_3]^{2+}$.

We have used eqs 1 and 2 to model our data numerically. In this analysis, the relaxation rates, k_B and k_D, are approximated to be temperature-independent, and k_{dd} is written using the usual Arrhenius type expression, that is, $k_{dd}(T) = A \exp(-\Delta E_{dd}/kT)$. The values for A and ΔE_{dd} were obtained from $[Ru(bpy)_3]^{2+}$ data to be 5.1×10^{12} s^{-1} and 3200 cm^{-1}, respectively; both agree well with values measured by other groups.[28,30,31,34−36] The solid line in Figure 5 corresponds to the lifetimes calculated using eqs 1 and 2 with $\Delta H° = -2380$ cm^{-1}, $\Delta S° = -9.92$ cm^{-1}/K, $k_B = (1740\ \text{ns})^{-1}$, and $k_D = (40\ \text{ns})^{-1}$. A nonlinear least-squares fit of the luminescence data is not possible because of a high correlation among several of the parameters. This correlation arises partially because of the limited temperature range over which the measurements can be performed with the sample remaining as a fluid. Nevertheless, the kinetic scheme reproduces the general form of the temperature-dependent lifetimes.

The dark state appears to share some common features with the charge-separated state observed in Ru(II)-acceptor systems. In particular, it is interesting to note that relaxation to the ground state from the dark state is significantly faster than it is from the bright state. This might seem counterintuitive given that, in the dark state, the photoexcited electron is farther away from the metal center than it is in the bright state. However, it is consistent with the back-electron-transfer times observed in a number of Ru(II)-based charge-separated states. Photoexcitation of Ru(II) compounds with ligand bound acceptors can lead to the formation of a charge-separated state, i.e., $[Ru^+(L)_3\cdots(A\bullet)^-]^{2+}$. The back electron-transfer times for a number of dyads of this type have been measured to be in the *subnanosecond* regime, which are far faster than the electron−hole recombination times observed from the ^{3}MLCT excited state of $[Ru(L)_3]^{2+}$ ($\sim 1\ \mu$s).[37−39] Schanze and co-workers[40] have postulated that this fast back electron transfer is facilitated by a rapid triplet → singlet spin conversion process in the $[Ru^+(L)_3\cdots(A\bullet)^-]^{2+}$ charge-separated state. Regardless of the mechanism, the presence of a fast back electron transfer appears to be a typical feature of the charge-separated systems. A relaxation rate (k_D) that is higher than that of ^{3}MLCT state decay but lower than that of back electron transfer in Ru(II)-acceptor systems suggests that the dark state of $[Ru(bpy)_2dppz]^{2+}$ can be viewed as an intermediate point along a continuum that bridges states that are truly molecular in nature (e.g., a ^{3}MLCT state) on one end and fully charge-separated (e.g., $[Ru^{\oplus}(L)_3\cdots(A\bullet)^-]^{2+}$) on the other.

C. Solvent Tuning of the Equilibrium Energetics. We have examined the temperature dependence of the emission lifetimes for $[Ru(bpy)_2dppz]^{2+}$ and $[Ru(dppz)_3]^{2+}$ in both linear alcohols and linear nitriles.[17] Displayed in Figure 5 are the luminescence lifetimes for $[Ru(bpy)_2dppz]^{2+}$ and $[Ru(dppz)_3]^{2+}$ in 1-propanol (PrOH), EtOH, and methanol (MeOH). For both complexes, the temperature corresponding to the maximum lifetime (T_{max}) continuously shifts toward higher temperatures as the solvent polarity is increased. For $[Ru(bpy)_2dppz]^{2+}$, T_{max} increases from PrOH (280 K) to EtOH (300 K). A rollover does not appear in the MeOH data probably because the solvent boils before the shift in excited-state population to the bright state occurs; however, we estimate using eqs 1 and 2 that the maximum would appear at about 350 K. The similar temperature dependence seen between $[Ru(bpy)_2dppz]^{2+}$ and $[Ru(dppz)_3]^{2+}$ supports the notion that the excited-state population is shared between fragments of dppz and not between separate ligands. For a given solvent, T_{max} for $[Ru(dppz)_3]^{2+}$ is shifted to a lower temperature compared to T_{max} for $[Ru(bpy)_2dppz]^{2+}$. The origin of this difference is unclear, but it could be a difference in the packing of the solvent around the two chromophores.

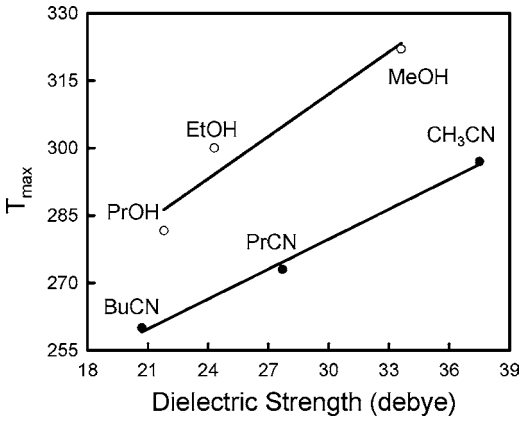

Figure 6. Temperature of maximum emission lifetime (T_{max}) of $[Ru(bpy)_2dppz]^{2+}$ as a function of solvent dielectric strength (ϵ). Both the alcohol and nitrile series are included. The correlation of dielectric strength with T_{max} suggests that the dark state has charge-separated character, not $^3\pi\pi^*$.

The temperature of the maximum lifetime (T_{max}) is displayed as a function of the solvent dielectric strength for $[Ru(bpy)_2dppz]^{2+}$ in both the nitriles and alcohols in Figure 6. There is a clear correlation between T_{max} and the solvent dielectric constant within each individual solvent series. The increase in T_{max} with increasing solvent polarity is consistent with a greater stabilization of the dark state in more polar solvents. If the charge distribution in the dark state is located primarily on the phz portion of the ligand (as was stated in section B), then it will have a greater dipole moment than the bright state. Dark-state stabilization could increase T_{max} in two ways. When the dark state is stabilized relative to the bright state, the larger energy gap (i.e., more negative $\Delta H°$) pushes the temperature at which the entropic term overcomes the enthalpic term to a higher value. Stabilization of the dark state would also decrease the energy gap between it and the ground state. On the basis of the energy gap law, one would then expect that this should *increase* the rate of nonradiative decay from the dark state (k_D), which, in turn, would shift T_{max} to higher temperatures. We do, in fact, observe larger k_D values in the more polar solvents. As seen in Figure 5, the lifetime at low temperature, which provides a direct measure of $(k_D)^{-1}$, decreases from MeOH to PrOH. Thus, the correlation of T_{max} and k_D with the solvent polarity indicates that there is a greater degree of charge separation in the dark state, suggesting that the dark state has charge-separated character and is not a ligand-centered $\pi\pi^*$ state.

The alcohol and nitrile series separate into two groups, with the nitriles having their maximum lifetimes at lower temperatures. The difference between the two series most likely stems from the ability of the alcohols to hydrogen bond to phz nitrogens, which would further stabilize the dark state more than electrostatic solvation alone.

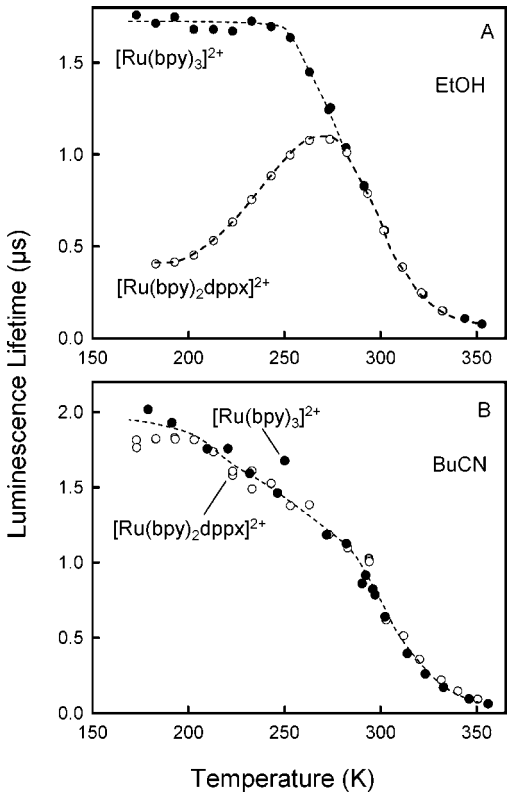

Figure 7. (A) Compilation of luminescence lifetimes as a function of temperature for [Ru(bpy)$_2$dppx]$^{2+}$ (○) and [Ru(bpy)$_3$]$^{2+}$ (●) in EtOH. (B) Luminescence lifetimes as a function of temperature for [Ru(bpy)$_2$dppx]$^{2+}$ (○) and [Ru(bpy)$_3$]$^{2+}$ (●) in butyronitrile (BuCN). The dashed lines are included to guide the eye.

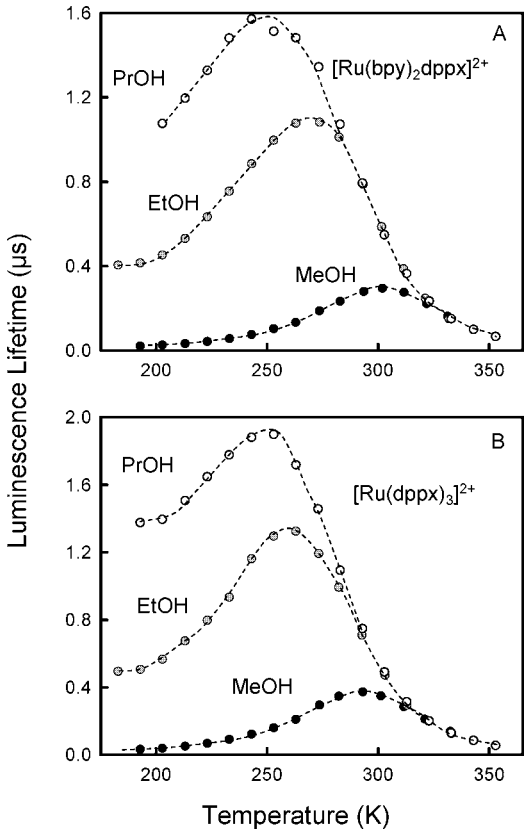

Figure 8. Excited-state lifetimes as a function of temperature in PrOH, EtOH, and MeOH for (A) [Ru(bpy)$_2$dppx]$^{2+}$ and (B) [Ru(dppx)$_3$]$^{2+}$. The dashed lines are included to guide the eye.

D. Altering the Equilibrium Energetics via Chemical Modification. We performed similar experiments on a complex (Figure 1) with a chemically modified dppz ligand, [Ru(bpy)$_2$dppx]$^{2+}$. Figure 7A shows the temperature-dependent lifetimes of [Ru(bpy)$_2$dppx]$^{2+}$ in EtOH. Between 270 and 330 K, [Ru(bpy)$_3$]$^{2+}$ and [Ru(bpy)$_2$dppx]$^{2+}$ exhibit similar luminescence. The shared photophysical behavior at high temperatures suggests that the same excited-state dynamics are responsible for the observed emission in both molecules. This also indicates that the additional methyl groups do not affect the energy of the bpy state dramatically. The decrease in lifetime below 270 K for [Ru(bpy)$_2$dppx]$^{2+}$ is evidence that the same general photophysical model can be used to describe both the substituted and unsubstituted molecules. However, there are some minor differences. The maximum lifetime for [Ru(bpy)$_2$dppx]$^{2+}$ occurs at a colder temperature than that of [Ru(bpy)$_2$dppz]$^{2+}$, which is indicative of a smaller energy gap between bright and dark states. Because the bright-state energy remains the same upon addition of the methyl groups, the energy gap must become smaller by raising the energy of the dark state. This is consistent with the expectation that the electron-donating substituents would raise the energy of the $\pi\pi^*$ orbital on the phz portion of the dppx ligand.

The luminescence lifetimes for both the [Ru(bpy)$_2$dppx]$^{2+}$ and [Ru(dppx)$_3$]$^{2+}$ complexes in the other alcohols (MeOH and PrOH) exhibit the same general trends as their unsubstituted analogues (Figure 8). Once again, this points to an excited-state equilibrium involving a bright state localized on the bpy fragment of the dppx ligand and not on one of the ancillary bpy ligands.

Although the [Ru(bpy)$_2$dppx]$^{2+}$ and [Ru(bpy)$_2$dppz]$^{2+}$ complexes show similar behavior in the alcohols, in the nitriles, they behave quite differently. Figure 7B shows the temperature-dependent emission lifetimes of [Ru(bpy)$_2$dppx]$^{2+}$ and [Ru(bpy)$_3$]$^{2+}$ in butyronitrile. Unlike in alcohols, [Ru(bpy)$_2$dppx]$^{2+}$ does not show the rollover at low temperature. The monotonic temperature dependence for [Ru(bpy)$_2$dppx]$^{2+}$ suggests that the excited-state population remains in the bright state throughout this temperature range. Perhaps the absence of a rollover arises because the energy gap has been decreased such that it can be overcome even at very low temperatures. It is also possible that the methyl groups have raised the energy of the phz state higher than that of the bpy state. Inverting the state order would make the bright state enthalpically favored. As a result, the population would remain in the bright state, and photophysics similar to that of [Ru(bpy)$_3$]$^{2+}$ would be observed at all temperatures.

IV. Conclusions

The temperature-dependent light-switch behavior observed in Ru(II)-dppz complexes results from a dynamic equilibrium between two MLCT states associated with the dppz ligand. One is a bright state with a ligand orbital similar in size to that associated with the ^{3}MLCT state of [Ru(bpy)$_3$]$^{2+}$, and the other moiety is a dark phz-like state. The light-switch mechanism stems from a competition between energetic factors that favor the dark (phz) state and entropic factors that favor the bright (bpy) state.

Acknowledgment. Funding for this project was provided by the National Science Foundation (CHE-0301266) and Los Alamos National Laboratories Laboratory Directed Research and Development Program (Project 20020222ER).

References and Notes

(1) Chambron, J. C.; Sauvage, J. P. *Chem. Phys. Lett.* **1991**, *182*, 603−607.

(2) Hartshorn, R. M.; Barton, J. K. *J. Am. Chem. Soc.* **1992**, *114*, 5919−5925.

(3) Sabatani, E.; Nikol, H. D.; Gray, H. B.; Anson, F. C. *J. Am. Chem. Soc.* **1996**, *118*, 1158−1163.

(4) Coates, C. G.; Mcgarvey, J. J.; Callaghan, P. L.; Coletti, M.; Hamilton, J. G. *J. Phys. Chem. B* **2001**, *105*, 730−735.

(5) Friedman, A. E.; Chambron, J. C.; Sauvage, J. P.; Turro, N. J.; Barton, J. K. *J. Am. Chem. Soc.* **1990**, *112*, 4960−4962.

(6) Haq, I.; Lincoln, P.; Suh, D. C.; Norden, B.; Chowdhry, B. Z.; Chaires, J. B. *J. Am. Chem. Soc.* **1995**, *117*, 4788−4796.

(7) Hiort, C.; Lincoln, P.; Norden, B. *J. Am. Chem. Soc.* **1993**, *115*, 3448−3454.

(8) Ossipov, D.; Pradeepkumar, P. I.; Holmer, M.; Chattopadhyaya, J. *J. Am. Chem. Soc.* **2001**, *123*, 3551−3562.

(9) Delaney, S.; Pascaly, M.; Bhattacharya, P. K.; Han, K.; Barton, J. K. *Inorg. Chem.* **2002**, *41*, 1966−1974.

(10) Amouyal, E.; Homsi, A.; Chambron, J. C.; Sauvage, J. P. *J. Chem. Soc., Dalton Trans.* **1990**, 1841−1845.

(11) Schoonover, J. R.; Bates, W. D.; Meyer, T. J. *Inorg. Chem.* **1995**, *34*, 6421−6422.

(12) Jenkins, Y.; Friedman, A. E.; Turro, N. J.; Barton, J. K. *Biochemistry* **1992**, *31*, 10809−10816.

(13) Nair, R. B.; Cullum, B. M.; Murphy, C. J. *Inorg. Chem.* **1997**, *36*, 962−965.

(14) Önfelt, B.; Olofsson, J.; Lincoln, P.; Nordén, B. *J. Phys. Chem. A* **2003**, *107*, 1000−1009.

(15) Olofsson, J.; Önfelt, B.; Lincoln, P. *J. Phys. Chem. A* **2004**, *108*, 4391−4398.

(16) Olson, E. J. C.; Hu, D.; Hormann, A.; Jonkman, A. M.; Arkin, M. R.; Stemp, E. D. A.; Barton, J. K.; Barbara, P. F. *J. Am. Chem. Soc.* **1997**, *119*, 11458−11467.

(17) Brennaman, M. K.; Alstrum-Acevedo, J. H.; Fleming, C. N.; Jang, P.; Meyer, T. J.; Papanikolas, J. M. *J. Am. Chem. Soc.* **2002**, *124*, 15094−15098.

(18) The dark state within our model is not required to be strictly nonemissive and, in light of a recent publication (ref 15), is probably partially emissive in certain instances. Nevertheless, because the bright and dark states of our model are in constant equilibrium, neither the analysis nor the conclusions presented in this work would be affected by this detail.

(19) Pourtois, G.; Beljonne, D.; Moucheron, C.; Schumm, S.; Kirsch-De Mesmaeker, A.; Lazzaroni, R.; Bredas, J. L. *J. Am. Chem. Soc.* **2004**, *126*, 683−692.

(20) Fleming, C. N.; Maxwell, K. A.; DeSimone, J. M.; Meyer, T. J.; Papanikolas, J. M. *J. Am. Chem. Soc.* **2001**, *123*, 10336−10347.

(21) Ackermann, M. N.; Interrante, L. V. *Inorg. Chem.* **1984**, *23*, 3904−3911.

(22) Barigelletti, F.; Belser, P.; von Zelewsky, A.; Juris, A.; Balzani, V. *J. Phys. Chem.* **1985**, *89*, 3680−3684.

(23) A number of groups have studied the photophysics of Ru(II) polypyridyl complexes in partially frozen solvents and reported on the complicated nature of the spectroscopy that arises in part from the slow solvent reorganization of these highly viscous environments. See: Chen, P.; Meyer, T. J. *J. Phys. Chem.* **1994**, *98*, 1439−1477 and references therein. Therefore, one must be careful in the assessment of any behavior near the fluid−glass transition temperature. In particular, it is unclear in a recent report by Olofsson et al. (ref15) what role the slowly reorganizing solvent plays in the photophysics.

(24) A time-dependent spectral shift to the red would manifest itself in the single-detection wavelength kinetics as (1) a transient *growth* in the emission at early times on the red edge of the emission band and (2) a fast *decay* component on the blue edge. Transients obtained at the red and blue edges of the emission spectrum decay with single-exponential kinetics after about 200 ps (earliest time with no contribution from our instrument response), indicating that there is no time-dependent shift in the emission band.

(25) Van Houten, J.; Watts, R. J. *Inorg. Chem.* **1978**, *17*, 3381−3385.

(26) Lumpkin, R. S.; Kober, E. M.; Worl, L. A.; Murtaza, Z.; Meyer, T. J. *J. Phys. Chem.* **1990**, *94*, 239−243.

(27) Kober, E. M.; Meyer, T. J. *Inorg. Chem.* **1984**, *23*, 3877−3887.

(28) Barigelletti, F.; Juris, A.; Balzani, V.; Belser, P.; von Zelewsky, A. *Inorg. Chem.* **1983**, *22*, 3335−3339.

(29) Hager, G. D.; Crosby, G. A. *J. Am. Chem. Soc.* **1975**, *97*, 7031−7041.

(30) Lytle, F. E.; Hercules, D. M. *J. Am. Chem. Soc.* **1969**, *91*, 253−257.

(31) Allsopp, S. R.; Cox, A.; Kemp, T. J.; Reed, W. J. *J. Chem. Soc., Faraday Trans.* **1978**, *1*, 1275−1289.

(32) Sykora, M.; Kincaid, J. R. *Inorg. Chem.* **1995**, *34*, 5852−5856.

(33) Mansour, M. A.; Lachicotte, R. J.; Gysling, H. J.; Eisenberg, R. *Inorg. Chem.* **1998**, *37*, 4625−4632.

(34) Cherry, W. R.; Henderson, L. J., Jr. *Inorg. Chem.* **1984**, *23*, 983−986.

(35) Wacholtz, W. F.; Auerbach, R. A.; Schmehl, R. H. *Inorg. Chem.* **1986**, *25*, 227−234.

(36) Durham, B.; Caspar, J. V.; Nagle, J. K.; Meyer, T. J. *J. Am. Chem. Soc.* **1982**, *104*, 4803−810.

(37) Schanze, K. S.; Sauer, K. *J. Am. Chem. Soc.* **1988**, *110*, 1180−1186.

(38) Yonemoto, E. H.; Riley, R. L.; Kim, Y. I.; Atherton, S. J.; Schmehl, R. H.; Mallouk, T. E. *J. Am. Chem. Soc.* **1992**, *114*, 8081−8087.

(39) Cooley, L. F.; Headford, C. E. L.; Elliott, C. M.; Kelley, D. F. *J. Am. Chem. Soc.* **1988**, *110*, 6673−6682.

(40) Schanze K. S.; Walters, K. A. *Organic and Inorganic Photochemistry*; Marcel-Dekker: New York, 1998; pp 75−127.

ARTICLES

Investigation of Interligand Electron Transfer in Polypyridyl Complexes of Os(II) Using Femtosecond Polarization Anisotropy Methods: Examination of $Os(bpy)_3^{2+}$ and $Os(bpy)_2(mab)^{2+}$

George B. Shaw, Carter L. Brown, and John M. Papanikolas*

Department of Chemistry, Venable and Kenan Laboratories, The University of North Carolina at Chapel Hill, Chapel Hill, North Carolina 27599-3290

Received: July 30, 2001; In Final Form: November 5, 2001

Femtosecond pump−probe polarization anisotropy measurements are used to investigate the interligand electron transfer (ILET) dynamics in two polypyridyl Os(II) complexes following photoexcitation to a metal-to-ligand charge transfer (MLCT) state. The two complexes studied are $Os(bpy)_3^{2+}$ (bpy = 2,2′-bipyridine) and a mixed-ligand analogue, $Os(bpy)_2(mab)^{2+}$, where *mab* is a mono-amide functionalized bipyridine ligand. In acetonitrile, the *bpy* → *bpy* ILET time is 8.7 ps in $Os(bpy)_3^{2+}$ and the *bpy* → *mab* ILET is 1.5 ps in $Os(bpy)_2(mab)^{2+}$. A solvent dependence study reveals that the ligand−ligand electron-transfer time (in both complexes) scales with the reorganization time of the solvent, suggesting that ILET in these complexes occurs in the adiabatic limit. An analysis of the anisotropy amplitudes for the excited-state absorption in $Os(bpy)_3^{2+}$ may provide evidence for the formation of a delocalized (or partially delocalized) excited state produced by optical excitation.

I. Introduction

The interest in the excited-state properties of Ru(II) and Os(II) polypyridyl coordination complexes (Figure 1) is motivated largely by their potential for use in solar energy conversion applications. To this end, the spectroscopy of these complexes has been widely investigated, and from this work has emerged a basic understanding of the excited-state properties of $Ru(bpy)_3^{2+}$, $Os(bpy)_3^{2+}$ (bpy = 2,2′-bipyridine), and their simple analogues.[1−11] The lowest energy excited states are metal-to-ligand charge-transfer (MLCT) in nature. MLCT excitation is followed by efficient intersystem crossing (ISC) to the triplet manifold. It is fairly well established that in polar solvents the electron distribution in the ^{3}MLCT state is localized by the solvent (at least at long times after photoexcitation) on a single bipyridine ligand,[6,7] and thus $[M^{III}(bpy)_2(bpy•−)]^{2+}$ is a qualitatively accurate description of the *equilibrated* excited state. While the nature of the $Ru(bpy)_3^{2+}$ and $Os(bpy)_3^{2+}$ excited states at long times after photoexcitation are generally agreed upon, many questions regarding evolution on faster time scales still persist.

In recent years, several accounts describing ultrafast experiments on $Ru(bpy)_3^{2+}$ and other homoleptic complexes have appeared in the literature.[12−14] By and large, these indicate the presence of rich excited-state relaxation phenomena taking place on the femtosecond time scale. For instance, transient absorption studies on $Ru(bpy)_3^{2+}$ suggest that relaxation to the triplet manifold occurs within a couple hundred femtoseconds after photoexcitation,[12] implying that ISC occurs in concert with other spin-allowed relaxation processes such as solvent reorganization and intramolecular vibrational redistribution (IVR). Even after relaxation into the lowest excited state has occurred, the wave function is not static, and on longer time scales the photoexcited electron can incoherently hop from one ligand to another in what amounts to an interligand electron transfer (ILET) process.

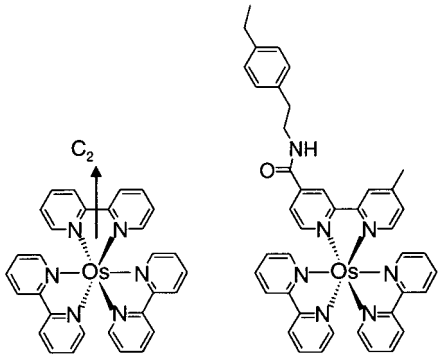

Figure 1. Chemical structures of the two Os(II) complexes discussed in this work. Os−BPY and Os−MAB refer to $Os(bpy)_3^{2+}$ and $Os(bpy)_2(mab)^{2+}$, respectively. In this notation, *bpy* and *mab* correspond to the bipyridine and mono-amide substituted bipyridine ligands, respectively. The *mab* ligand lies about 700 cm^{-1} lower in energy than *bpy*. The arrow in the Os−BPY diagram denotes one of the three C_2 symmetry axes.

ILET has received considerable attention in a variety of transition metal compounds.[15−24] We have explored this electron-transfer process in two polypyridyl Os(II) complexes using femtosecond pump−probe polarization spectroscopy. The molecular systems of interest are Os−BPY (BPY ≡ $(bpy)_3^{2+}$) and Os−MAB (MAB ≡ $(bpy)_2(mab)^{2+}$); their chemical structures

* To whom correspondence should be addressed. E-mail: John_Papanikolas@unc.edu.

10.1021/jp012924u CCC: $22.00
Published on Web 02/02/2002

are shown in Figure 1. The Kelley group[15−18] has investigated ILET in Ru−BPY and Os−BPY, also using polarization anisotropy methods. However, the enhanced time resolution of our apparatus (500 fs versus 10 ps) has yielded observations that are qualitatively inconsistent with theirs. Specifically, we measure the *bpy* → *bpy* ILET time in acetonitrile to be about 15 times faster than that reported by Kelley,[15] and through variation of the solvent we conclude that ILET takes place in the (strongly coupled) adiabatic limit.

The experiments described in this paper go beyond the symmetric Os−BPY complex and also describe observations made on a mixed-ligand complex, Os−MAB. Mixed-ligand complexes are quite common, and a large number have been synthesized. In part, this interest stems from their use as building blocks in larger arrays, where ligands with different substituents are needed to connect molecular subunits (see refs 25−27 for examples). The mixed-ligand complex used here is part of a macromolecular assembly that is currently under investigation in our laboratory for its light harvesting capability.[28] The Os−MAB complex is relatively simple when compared to the vast array of mixed-ligand complexes in existence, and thus it also serves as a model system for investigating the excited-state relaxation phenomena in a large number of complexes.

One consequence of this ligand asymmetry is that it affects the energies of the MLCT excited states. Because different ligands have different affinities for the excited electron, the MLCT states associated with different ligands have different energies. In this particular case, the electron withdrawing nature of the amide substituent allows for a larger delocalization of the π^* orbitals, and this stabilizes the *mab* MLCT state relative to the MLCT state associated with the unfunctionalized *bpy* ligand. This state ordering has been confirmed by transient infrared experiments[29] (on the ruthenium analog) that show the photoexcited electron on the *mab* ligand at long times after photoexcitation. The difference in energy between the two ligands has been established by electrochemical methods[30] to be approximately 700 cm^{-1}. Thus, there is a modest driving force for electron transfer that is not present in the Os−BPY complex, and as expected this results in faster ILET in the mixed-ligand species.

An important aspect of the discussion of the excited states is whether photoexcitation produces a localized excited state, or creates a delocalized state that then localizes due to environmental (inner- or outer-sphere) reorganization. The crucial issue is the magnitude of the ligand−ligand coupling in comparison to the nanoheterogeneity of the environment at the instant of photon absorption. The experimental evidence speaking to this point is mixed. In the past two decades there have been a variety of arguments both in favor of localized[31−35] and delocalized[14,36−40] excited states on the electronic time scale. Most of these experiments focused on the Ru−BPY complex. However, because the ruthenium and osmium analogues have different ligand−ligand couplings, the degree of delocalization in the initially prepared excited states may be quite different for Ru−BPY and Os−BPY. And so while the issues may be the same in the two complexes, the outcome may not.

Our experiments may speak to the nature of the excited-state charge distribution at the instant of photon absorption. One possible interpretation of the polarization anisotropy data presented in this paper is that the excited states (produced by excitation at the red-edge of the triplet absorption band) are partially delocalized over two or more of the ligands. In all likelihood this is a manifestation of an inhomogeneous excitation process arising from the distribution of local solvent environments at the instant of photon absorption. The observed anisotropy would then be an average over an excited-state ensemble that contains both localized and delocalized constituents. Our data is consistent with a ligand−ligand coupling that is large enough to yield adiabatic electron-transfer behavior, yet at the same time is smaller than (or comparable to) the degree of solvent inhomogeneity that is present when the complex is excited.

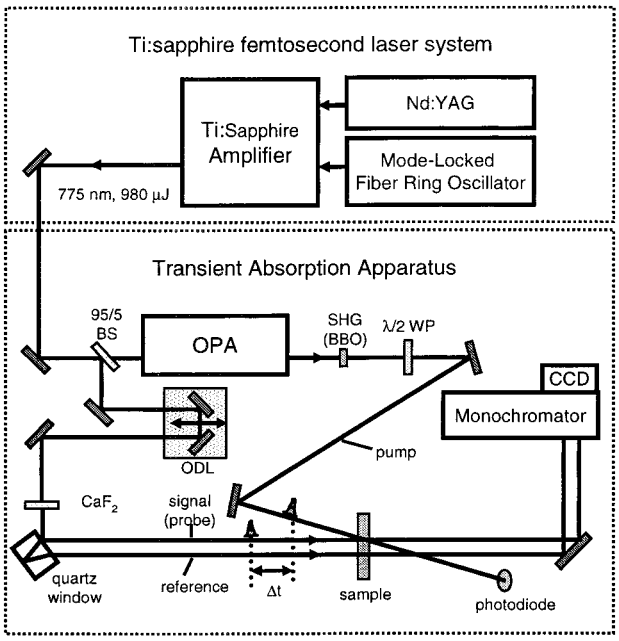

Figure 2. Schematic diagram of the femtosecond laser system and transient absorption apparatus used in this work.

II. Experimental Description

A schematic diagram of the laser system and the transient absorption apparatus is shown in Figure 2. The transient absorption spectrometer is based on a commercially available ultrafast laser system (Clark CPA-2001), consisting of an erbium-doped fiber ring oscillator and a chirped pulse Ti:sapphire regenerative amplifier that is pumped by a frequency-doubled, mode-locked, Q-switched Nd:YAG laser. The amplifier produces 120 fs laser pulses at 775 nm at 1 kHz with pulse energies of approximately 950 μJ/pulse. The amplified output is split into two beams by an uncoated glass window.

The larger, transmitted fraction (96%) pumps an optical parametric amplifier (OPA), which generates tunable femtosecond laser pulses. For the experiments described here, the output of the OPA is tuned to about 1400 nm and is frequency doubled to 700 nm to produce pulses with energies of about 10 μJ/pulse. This is the pump beam used to excite the osmium complexes in the transient absorption experiment. It is focused with a 30 cm lens to a spot size of ≈800 μm at the sample yielding a photon flux of approximately 10^{15} photons/cm^2. After passing through the sample, the pump beam is then directed into a photodiode for normalization of the transient absorption signal to changes in laser power.

The weak (4%) reflection from the front surface of the uncoated optic is used to generate the probe beam. This beam is directed into a computer-controlled translation stage that is used to vary the optical delay between pump and probe pulses. The resolution of the translation stage is 1 μm. After passing through the delay stage, it is focused with a 150 mm focal length

lens into a 6 mm thick CaF_2 window to generate a white light continuum, which is then collimated with an 80 mm focal length achromatic lens. Calcium flouride is used as the medium because the continuum it generates extends further into the UV (approximately down to 350 nm) than other substances, such as sapphire. The white light is split into two weaker beams of nearly equal intensity by taking the reflections off the front and rear surfaces of a 2.5 cm thick quartz window. The front surface reflection, denoted the signal beam, is used for the probe pulse. The rear surface reflection is used as the reference beam in the transient absorption measurement. The signal and reference beams are focused by 300 mm focal length fused silica lenses to a spot size of $\sim$150 μm at the sample. While both beams are directed through the sample, only the signal is spatially overlapped with the pump beam. The noncollinear approach of the pump and probe (signal) beams has an angle of approximately 2.5°. The signal and reference beams are simultaneously directed into a 0.27 m monochromator, dispersed with a 1200 line/mm holographic grating, and detected with a two-dimensional 1028 $\times$ 256 pixel liquid nitrogen cooled CCD array. This apparatus is capable of measuring a 77 nm segment of the transient absorption spectrum centered anywhere between 350 and 1000 nm with a sensitivity of better than 1 mOD.

The excited-state dynamics are followed through the evolution of the transient absorption spectra obtained at a series of pump−probe delay times. A typical data collection session consists of measuring transient absorption spectra at a series of 96 different pump−probe delay positions. First, the transient absorption spectrum at a given delay is measured. The intensity of the signal and reference beams are integrated during an 800 ms exposure of the CCD array and then used to calculate the excited-state/ground-state differential absorption (ΔA) spectrum. Ten exposures of the CCD camera are performed and the spectra from each are averaged together before moving on to the next pump−probe delay position. The entire set of pump−probe delay positions is repeated at least three times and the spectra obtained at like delays are averaged together. In some cases, the final spectrum represents a compilation of several different data collection sessions. Thus, each transient absorption spectrum represents an average over at least 24 000 (and in some instances as many as 150 000) laser pulses.

The frequency chirp in the while light continuum is characterized using the optical Kerr response of liquid CCl_4 to an intense laser field in a polarization gating geometry. The bottom pane in Figure 3 shows a contour plot of the Kerr signal as a function of pump−probe delay and probe wavelength. As the delay is increased the dominant frequency shifts to the red. This is a direct measure of the chirp in the white light pulse over the spectral range of interest. Between 360 and 420 nm (the spectral region of interest) the frequency chirp is approximately 2 ps. A horizontal slice through this surface is the cross-correlation at a specified probe wavelength. Several are shown in the top panel of Figure 3. Each has a fwhm of approximately 550 fs, which is about a factor of 2 greater than the pulse width of the laser. The primary source of this temporal broadening is a group velocity mismatch between the 700 nm pump beam and the 380 nm portion of the probe beam. This causes the pump and the probe pulses to travel at different speeds through the sample. By comparison, cross correlations with a portion of the continuum nearer to 600 nm are approximately 180 fs, which is closer to the durations of the individual pulses.

Both of the osmium complexes, $[Os(bpy)_3](PF_6)_2$ and $[Os(bpy)_2(mab)](PF_6)_2$, denoted Os−BPY and Os−MAB, respectively, were obtained as gifts from T. J. Meyer and used without further purification. The chloride salts of these compounds were used in experiments where ethylene glycol was the solvent. All of the solvents were spectral grade, and the acetonitrile was distilled over calcium hydride prior to use. The concentrations of all the samples used were adjusted to yield an optical density of approximately 0.25 at 450 nm in a 2 mm path length cell. All experiments were performed at room temperature.

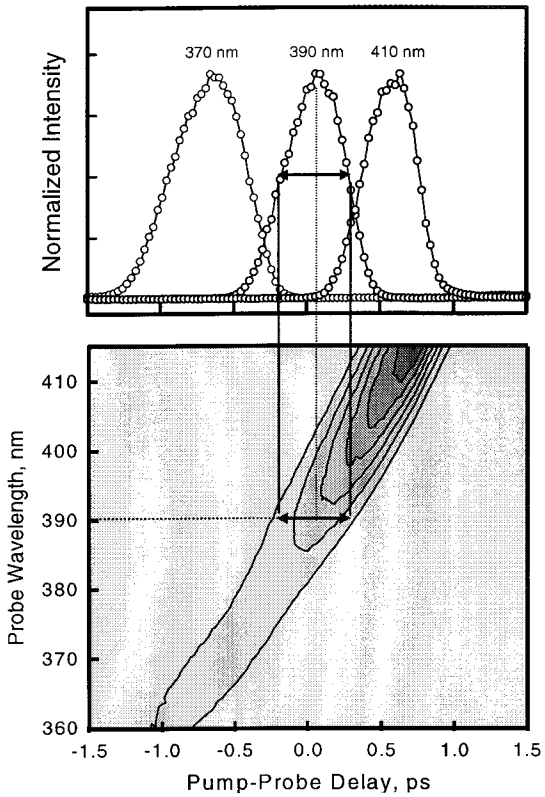

Figure 3. Bottom panel shows the intensity of the optical Kerr signal as a function of pump−probe delay and probe wavelength. The decrease in Kerr signal at the blue edge of the probe spectrum is a consequence of the lower intensity of the white light in that spectral region. The upper panel shows three time slices through this surface at different probe wavelengths. Each slice is normalized to the same intensity as the others and represents the cross correlation at the probe wavelength indicated in the figure. The fwhm of the cross correlation is $\approx$550 fs, which is broadened with respect to the laser pulse width due to group velocity mismatch between the pump and the probe pulses.

III. Results and Discussion

A comparison of the ground-state absorption spectra for Os−BPY and Os−MAB is shown in Figure 4. The primary difference between the two spectra is the presence of a slight red shift in the Os−MAB absorption features, which is consistent with a lower energy, *mab*-based MLCT state. Aside from this slight shift, the spectra are qualitatively similar; each shows an intense absorption band centered at about 450 nm and a weaker band that extends from approximately 520 nm to 700 nm. Both bands correspond to MLCT excitation. Photoexcitation within the stronger absorption feature promotes the complex to a singlet MLCT state. Afterward, the system undergoes efficient intersystem crossing to a low-lying triplet state.[41] Recent ultrafast experiments on Ru−BPY indicate that this takes place within a few hundred femtoseconds.[12] The analogous process in Os−BPY has not been fully characterized, but preliminary work in our laboratory suggests that the time scale for ISC in this complex may also be quite short.

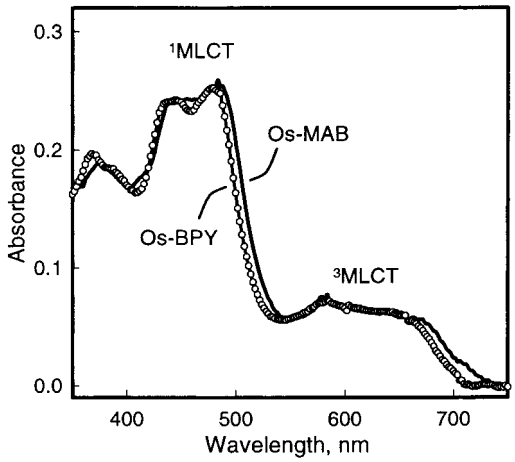

Figure 4. Ground-state absorption spectra of Os−BPY (points + line) and Os−MAB (line only) in room-temperature acetonitrile.

Photoexcitation within the weaker absorption feature corresponds to the direct population of the triplet state. There are, in fact, several ^{3}MLCT states associated with each ligand.[42−44] The lowest three states are primarily triplet in character, and lie within a hundred wavenumbers of each other. The fourth state, while still commonly described as a triplet, has a substantial amount of singlet character and resides about 300−600 cm^{-1} higher in energy.

We have performed experiments at both singlet and triplet excitation wavelengths. This paper focuses on excitation at the red edge of the triplet absorption band. For all of the experiments presented here, the Os−BPY and Os−MAB complexes were excited at 693 and 700 nm, respectively. By limiting excitation to the red edge of the triplet absorption, we promote the complex to the lowest energy excited-state accessible by optical excitation. This circumvents the singlet−triplet relaxation pathway and reduces the number of processes that contribute to the transient signals, thus simplifying the interpretation of the time-resolved data.

A. Solvated Electronic Structure. The Os−BPY complex has D_3 symmetry, and as such the electronic states of the *isolated* molecule are identified with either A or E symmetry labels. This is the case at the instant of photoexcitation, and ignoring any inner sphere reorganization effects, at long times as well. For a *solvated* molecule, the situation is somewhat different. At long times after photoexcitation, the charge is trapped by the solvent on a single ligand, thus making these symmetry labels irrelevant. Still uncertain, however, is the extent to which they are relevant for describing the MLCT excited states at the instant of photoexcitation. What is clear is that the excited-state wave function of the complex depends as much upon the details of the solvent environment as its own molecular Hamiltonian. One is thus forced to confront the electronic structure of the *solvated* species.

For a symmetric molecule like Os−BPY, the degree of charge delocalization in the MLCT state is determined by the relative magnitudes of the electronic coupling between the bipyridine ligands and the electrostatic asymmetry presented by the molecular environment. The ligand orbitals for a molecule embedded in a symmetric environment (e.g., the isolated molecule) will be degenerate, and a weak electronic coupling is sufficient to achieve complete delocalization. The situation may be quite different for an osmium complex embedded in a polar solvent. The electrostatic asymmetry presented by the local environment will lift the degeneracy of the three ligands, and

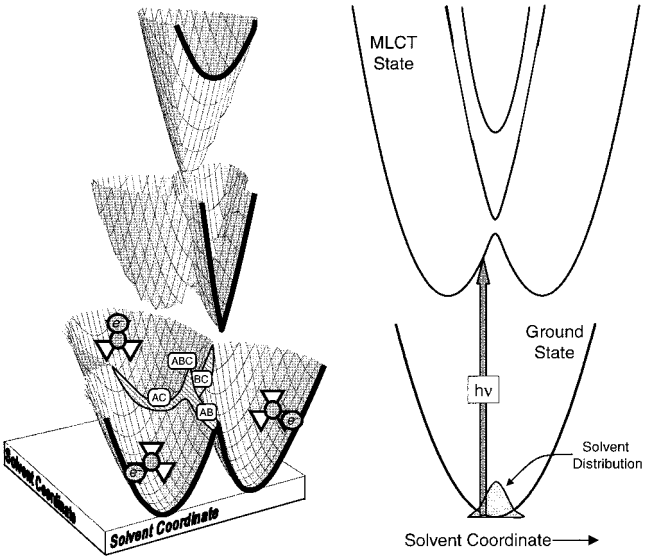

Figure 5. Illustration of the *solvated* MLCT excited-state potential surfaces for Os−BPY. The diagrams represent the extension of the classic Marcus−Hush diagram for electron transfer from a two-center to a three-center system. The diagram at the left is a 3-D representation of the three adiabatic surfaces, which are vertically offset for clarity. The minima in the lowest energy surface correspond to the localization of the charge by the solvent on a different bipyridine ligand. There is a diagram of this type associated with each MLCT excited state. The diagram at the right is a cross section through these surfaces, with the potential energy curves corresponding to the bold lines along the cut-out of the 3-D potential. The ground-state potential surface is displayed in the 2-D diagram, but is omitted from the 3-D picture.

if the asymmetry is large enough, the electronic states will have a localized charge distribution.

A schematic diagram of a potential surface illustrating these concepts is shown in Figure 5. This picture is a qualitative extension of the classic Marcus−Hush diagram from a two-center to a three-center system. The excited-state energies are displayed as a function of a two-dimensional solvent coordinate, which is necessary to describe a system with three sites for the location of the electron. As such, three diabatic surfaces are needed to describe Os−BPY, one for the localization of the electron on each of the three ligands. In keeping with Marcus−Hush theory, these diabatic states are represented by parabolic surfaces placed at the corners of an equilateral triangle within this two-dimensional solvent plane. Electronic mixing between the ligands leads to the formation of an avoided crossing at the intersections between the diabatic states, resulting in the three adiabatic surfaces depicted in Figure 5. For clarity, these surfaces are vertically offset from each other in the figure.

The lowest energy adiabatic surface has three distinct minima, each corresponding to the localization of the charge on a different bipyridine moiety. In the context of this diagram, ILET corresponds to movement from one minimum to another. Not all points on this surface correspond to localized excited states, however. Along the ridge denoted AB (which marks the intersection between the diabatic surfaces of A and B) the solvent brings ligand A into resonance with ligand B (but not C). For points along this boundary, the excited-state wave function has C_2 symmetry. There are two other two-center resonance seams, marked AC and BC. The point marked ABC corresponds to the totally symmetric solvent configuration that simultaneously brings all three ligands into resonance. This is the only point on the excited-state potential energy surface in which it is appropriate to discuss the electronic structure of Os−BPY in the context of the D_3 point group.

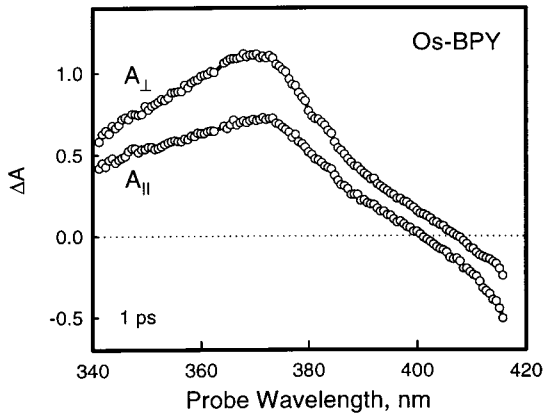

Figure 6. Transient absorption spectra observed 1 ps after photoexcitation of Os−BPY in room-temperature acetonitrile. The two spectra were obtained with pump and probe polarization vectors set to be parallel ($A_{||}$) or perpendicular ($A_{\perp}$).

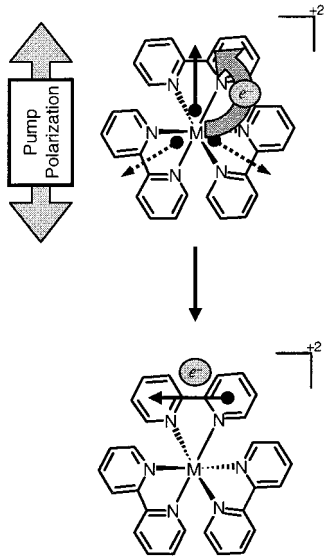

Figure 7. Illustration of the photoselection process in Os−BPY for a vertically polarized excitation laser. Arrows placed within the chemical structure depict the direction of the transition dipoles for MLCT excitation (top) and probe transition dipole (bottom). The excitation dipoles are depicted for the weak ligand−ligand coupling (i.e., localized excited-state) limit.

Strictly speaking, delocalized wave functions with C_2 or D_3 symmetry are only present for complexes that lie along one of the ridges, or at the central cusp point. This is blurred, to some extent, by the ligand−ligand coupling, and thus a region of delocalized excited states exists in the vicinity of the avoided crossings. This region is identified in the figure by the "outlined" area. Its size will depend on the magnitude of the coupling, and for a weak coupling, it will be relatively narrow. But, as the coupling increases more inhomogeneity in the solvent environment can be overcome, and the region corresponding to delocalized wave functions will broaden. It has been suggested[15,40] that the ligand−ligand coupling is about 2−20 cm^{-1}. The experiments presented in this paper suggest that this is too small, and indicate a somewhat larger value of several hundred wavenumbers.

The localized versus delocalized nature of the wave function is determined by the initial location of the system on this potential surface, which is linked to the configuration of the solvent when the photon is absorbed. Thus the relevant question is: what is the distribution of solvent configurations that surround the *ground-state* complex? The ground state has no dipole moment, and so the minimum of its potential surface, and the center of this distribution, is located directly below the central cusp point (ABC) of the excited-state potential. The excited-state ensemble will therefore be a superposition of both localized and delocalized excited states. The relative contribution of each is determined by the distribution of solvent configurations and the magnitude of the electronic coupling. It is also dependent upon the color of the excitation photon, as not every member of the ground-state ensemble will be excited at a given photon energy. At the red edge of the triplet absorption band there is a preferential excitation of the systems that lie in the wings of the distribution. This will tend to produce localized excited states, and generally speaking our data bear this out. But, in addition to this localized fraction, our data seem to suggest that a significant subset of the excited-state ensemble is initially delocalized. This would imply that there is a fairly broad region of the potential surface that corresponds to delocalized excited states, and is consistent with our finding of a large electronic coupling and rapid ILET. This is discussed in more detail in Section E.

B. Transient Absorption; General Considerations. The excited-state dynamics are followed using femtosecond transient absorption methods. Displayed in Figure 6 are transient absorption spectra observed for Os−BPY 1 ps after photoexcitation at 693 nm. Two spectra are shown—one obtained with the pump and probe polarizations parallel to each other, and the other perpendicular. Both have an intense absorption centered in the neighborhood of 370 nm that arises from a ligand-localized $\pi\pi^*$ transition on the bipyridine radical anion (bpy^-) fragment of the MLCT excited state.[45−49] The difference in magnitude between the two spectra results from a photoselection process, which is depicted schematically in Figure 7.

Photoexcitation with linearly polarized light preferentially excites those molecules whose absorption dipoles are aligned along the laser polarization vector. For Os−BPY, the low energy MLCT excitations are polarized in the plane containing the three C_2 axes, i.e., the axes that extend from the metal center and bisect the bipyridine ligands.[50] The orientation of the dipoles within this plane depends on the degree of localization in the excited-state wave function. If the excited states are localized, then the three ligands will be independent of each other. In this limit, the excitation can be regarded as a superposition of three separate transition dipoles, each directed along a C_2 symmetry axis. Photoexcitation with linearly polarized light will then promote an electron to the ligand that is most closely aligned along the laser polarization vector. The probe transition dipole is oriented along the long axis of the bipyridine ligand,[49] perpendicular to the excitation dipole. Thus, the greatest excited-state absorption is observed when the probe beam is polarized perpendicular to that of the pump beam, as is observed. The relative intensities of the parallel and perpendicular spectra are thus a measure of the anisotropy in the excited-state transition dipole distribution.

The parallel and perpendicular transient absorption spectra also carry information about the excited-state populations (as would be observed in a conventional flash photolysis experiment). The separation of the population and anisotropy contributions to the data is essential for the interpretation of the transient signals. Spectra collected at the so-called "magic angle" polarization contain only population information. These can either be obtained directly, by measuring transient spectra with the angle between the pump and probe polarizations set to 54.7°

(the magic angle), or constructed from the parallel and perpendicular data, i.e.,

$$A_{MA} = \frac{1}{3}(A_{||} + 2A_{\perp}) \quad (1)$$

The polarization anisotropy, $r(t)$, contains information regarding changes in the transition dipole direction, and is defined as:

$$r(t) = \frac{A_{||} - A_{\perp}}{A_{||} + 2A_{\perp}} \quad (2)$$

The polarization anisotropy will take on a definite value determined by the relative orientation of the pump and probe transition dipoles. For nondegenerate transitions the anisotropy at early delay times, $r(t = 0,\theta)$ is given by

$$r(t = 0,\theta) = \frac{1}{5}(3\cos^2\theta - 1) \quad (3)$$

where θ is the angle between the pump and probe excitations. In many polarization anisotropy measurements, the initial value for $r(t)$ must be between $+0.4$ and -0.2, with the limiting cases corresponding to parallel ($\theta = 0°$) and perpendicular ($\theta = 90°$) excitations, respectively. This is the case in time-resolved fluorescence measurements, for example. The situation in transient absorption spectroscopy is somewhat more complicated, and this is discussed in more detail in Section D.

Polarization anisotropy is the ideal means for studying ILET in transition metal complexes. In Os−BPY all three ligands are identical, and thus the transfer of the electron from one ligand to another will not give rise to changes in the shape or amplitude of the excited-state spectra. Thus the magic angle spectra cannot provide information about the ligand−ligand hopping process. This is not the case for polarization anisotropy. As the electron hops from one ligand to another, the direction of the $\pi\pi^*$ transition dipole changes, and this degrades the anisotropy. Thus, the decay in r(t) with time after photoexcitation provides a direct indicator of the ligand−ligand hopping.

The application of polarization anisotropy to the study of ILET hinges upon the ability of the optical excitation to create a *localized* charge distribution. If the coupling between the ligands is large enough to overcome the asymmetry in the solvent environment, the optically prepared excited state will be delocalized, and the direction of the transition dipoles for MLCT excitation will be ill defined. As a result, there will be no correlation between the polarization vector of the laser and the initial location of the photoexcited electron. In this limit, polarization anisotropy cannot be used to probe the ILET process.

C. Magic Angle. The "magic angle" spectra observed at 400 ps after photoexcitation are shown in Figure 8 for the two complexes. The absorption feature that dominates this spectral region arises from a ligand localized $\pi\pi^*$ transition.[45−49] For Os−BPY, this is a bpy^- absorption. For the mixed-ligand complex it is an excitation of the lowest energy ligand, which in this case is mab^-. A comparison of the limiting spectra indicates that the absorption of the mab^- ligand is red shifted relative to that of its bipyridine parent, which is qualitatively consistent with the more delocalized π-network in that ligand.

The time evolution of the Os−BPY and Os−MAB spectra is depicted in Figure 9, which show the transient absorption signal as a function of pump−probe delay at several different probe wavelengths. In our analysis of the transient absorption data we examined seven probe wavelengths dispersed across

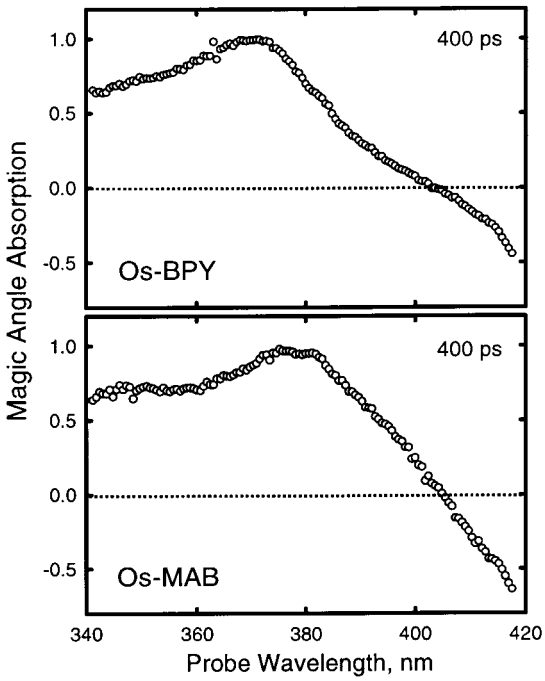

Figure 8. Magic angle spectra observed at 400 ps after photoexcitation of Os−BPY and Os−MAB. Os−BPY is excited at 693 nm and Os−MAB is excited at 700 nm. These are limiting spectra and reflect a ligand-localized $\pi\pi^*$ absorption on the lowest energy ligand. For Os−MAB this is the *mab* ligand.

this spectral region, although only three are shown for each complex. In both complexes there is a slight spectral reshaping that occurs in the first few picoseconds after photoexcitation. It is complete within 2−3 ps for Os−BPY and 10−15 ps for Os−MAB. In principle, this spectral evolution could stem from changes in either the ground-state bleach or excited-state absorption.

There are two possible contributions to spectral evolution of the bleach. The most obvious is the replenishment of the ground-state population, which would lead to an overall decrease in both the excited-state absorption and ground-state bleach contributions to the spectrum. This process can be ruled out because the excited state lifetimes of these osmium complexes are about 50 ns, and therefore, there is essentially no relaxation back to the ground state on the time scale of these experiments. The photoselective bleaching of a spectrally inhomogeneous ground-state population is another possible source. This is identical to the bleach evolution studied in transient hole burning experiments, which probe fluctuations in the solvent shell surrounding ground-state molecules. Recent ultrafast experiments[12] on Ru−BPY indicate that evolution in the bleach region of the spectrum (400−500 nm) is complete within 300 fs after photoexcitation. Since one would expect the time scale for solvent fluctuations surrounding a ground-state Ru−BPY complex to be similar to that for Os−BPY, this suggests that any bleach evolution that does occur is probably complete within a few hundred femtoseconds after photoexcitation. For this reason the observed spectral changes are attributed solely to changes in the excited-state absorption.

To quantify the changes at early delays, the magic angle absorption surface of each complex is fit to an exponential function of the form

$$A^{\lambda}_{MA}(t) = c^{\lambda}_1 \exp(-k_1 t) + c^{\lambda}_2 \exp(-k_2 t) + c^{\lambda}_{\infty} \quad (4)$$

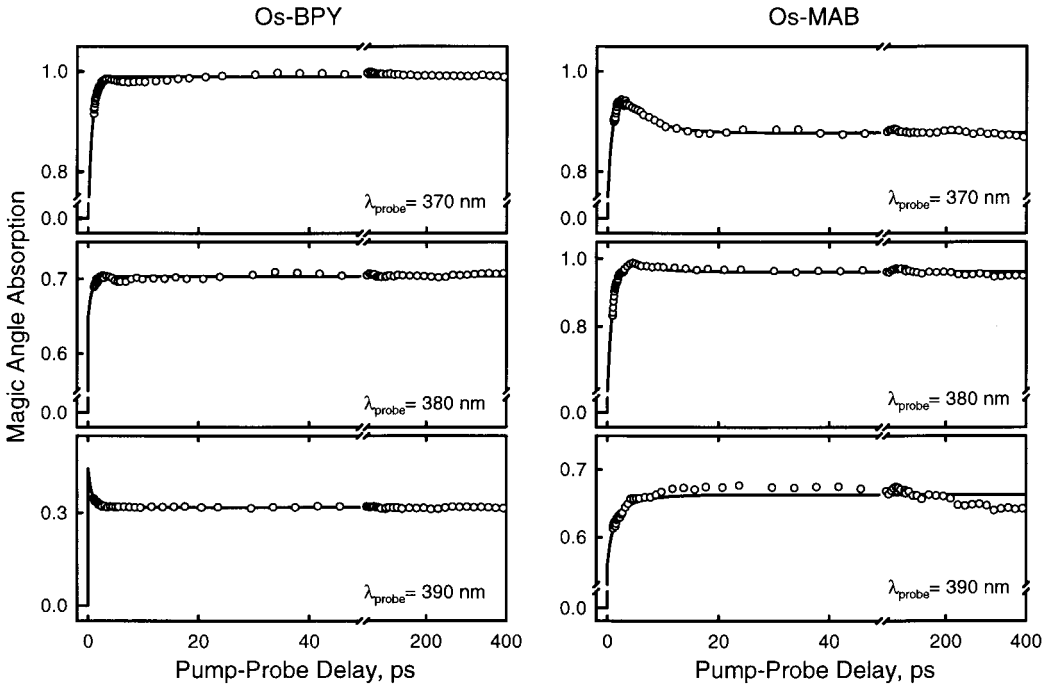

Figure 9. Transient absorption signal as a function of pump−probe delay for Os−BPY (left) and Os−MAB (right) in room-temperature CH_3CN. Transients at three probe wavelengths are shown for each complex; however, in our analysis of the data, seven such transients are utilized. A single exponential with a 0.75 ps time constant can describe all seven transients for Os−BPY. For the mixed ligand complex, a biexponential function with time constants of 1.0 and 4.5 ps are needed to obtain an adequate fit.

where λ refers to the probe wavelength, the rate constants (k_1 and k_2) are the same for λ's, and the amplitudes (c_1^λ, c_2^λ, and c_∞^λ) vary from one probe wavelength to another. The analysis involves the simultaneous fit of transients at seven different probe wavelengths.

The transient absorption surfaces of both complexes are well described by this functional form. The Os−BPY data can be fit using a single-exponential term with a 0.75 ps time constant. The spectral evolution in the mixed-ligand species is more complex, and two exponential terms (with 1 ps and 4−5 ps time constants) are needed. The solid lines in Figure 9 are the results of this fit. Displayed in Figure 10 are the coefficients that correspond to the growth (or decay) of the transient absorption signal, c_1^λ and c_2^λ. These are displayed such that a positive number reflects growth in the transient absorption signal. The fast decay component shows spectral changes that are qualitatively the same in both complexes. The similarities extend beyond just the fact that they evolve on similar time scales (0.75 ps vs 1.0 ps). In both cases there is a growth near the absorption maximum that is accompanied by a slight spectral narrowing. Rapid evolution in the transient spectra of polypyridyl complexes is not without precedence. McCusker and co-workers[12] have observed dramatic spectral changes in the first few hundred femtoseconds after the photoexcitation of Ru−BPY, which were attributed to single−triplet relaxation. The origin of the rapid growth in the Os−BPY and Os−MAB complexes is still not clear. It could arise from slight changes in the $\pi\pi^*$ absorption band that occur during relaxation through the low-lying triplet states and/or fast inertial reorganization of the solvent about the nascent charge distribution formed by MLCT excitation. Whatever the origin of this fast spectral reshaping, it appears to stem from a dynamical process that is common to both complexes.

The slow component is only present in the mixed-ligand complex, suggesting that its dynamical origin stems from the *mab* ligand. The coefficients associated with this kinetic component show growth at the absorption band's red edge and simultaneous decay at its blue edge, amounting to what is a red shift in the absorption band. The time constant for this

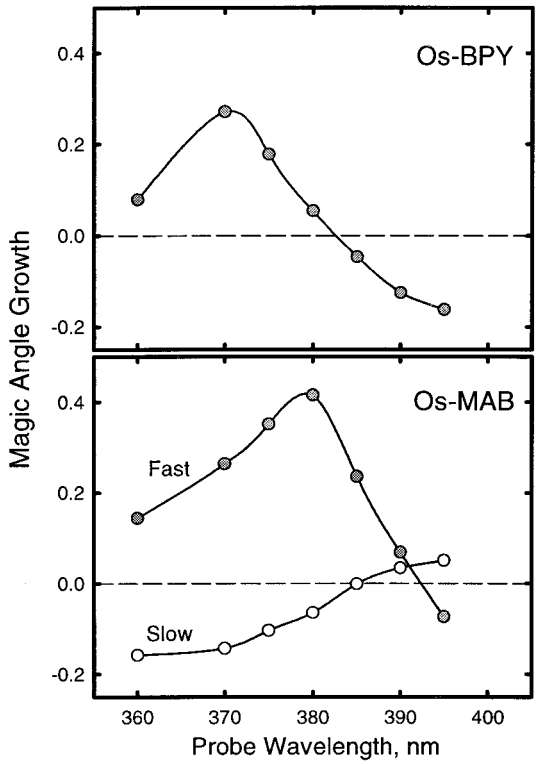

Figure 10. Amplitudes (c_1^λ and c_2^λ) obtained from nonlinear least-squares fit of magic angle spectral data to exponential functions. (Top panel) Results for Os−BPY, where only a single (0.75 ps) exponential function is needed. Thus, only a single amplitude (c_1^λ) is displayed. (Bottom panel) Results for Os−MAB. Two exponentials (1.0 and 4.5 ps) are needed to obtain an adequate fit for this complex. Filled and open circles represent amplitudes of fast and slow components, respectively. Positive numbers indicate growth of the transient absorption signal at that probe wavelength. Negative numbers indicate decay.

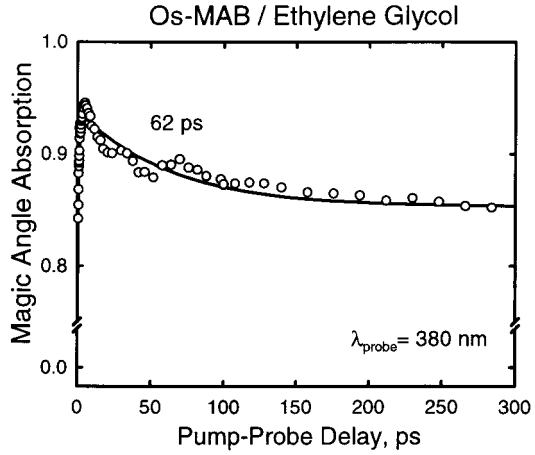

Figure 11. Transient absorption signal obtained for Os−MAB in room-temperature ethylene glycol. There is a rapid (0.7 ps) growth in the transient absorption signal at this probe wavelength followed by a slow (62 ps) decay. The time scale for the growth in ethylene glycol is similar to that observed in CH_3CN, but the decay is much slower. A rapid growth is also observed for Os−BPY in ethylene glycol (data not shown), but unlike Os−MAB there is no decay in the transient absorption signal at long delay times.

spectral shift depends on the reorganization time of the solvent. Shown in Figure 11 is the transient absorption signal at 380 nm for Os−MAB in room-temperature ethylene glycol. While the fast component in this solvent (0.7 ps) is similar to that observed in CH_3CN, the slow kinetic component (63 ps) is about 10 times longer. One possible origin for this slow component is intramolecular vibrational relaxation. While one would expect the relaxation time to be solvent dependent, the observation that the decay is almost 10 times faster in acetonitrile seems too large to attribute to vibrational relaxation. Another possibility is that it reflects the *bpy* → *mab* ILET process. However, this assignment is not consistent with the polarization anisotropy data discussed in Section D. A third possibility is that the red spectral shift arises from the solvation of the mab^- ligand *after* ILET occurs. The "diffusive" reorganization time of acetonitrile is 2−3 ps.[51] Ethylene glycol exhibits multiexponential solvation kinetics with diffusive reorganization times ranging from 4 to 284 ps.[51] The qualitative scaling of the spectral reshaping times with the diffusive reorganization times supports this assignment.

D. Polarization Anisotropy. Our discussion of the polarization anisotropy data is divided into three sections. In the first section we develop a framework in which to quantitatively analyze anisotropy data obtained in a transient absorption experiment. This discussion is motivated by anomalous anisotropy values observed at early pump−probe delay times. In the second section the anisotropy decays for Os−BPY and Os−MAB are discussed in the context of ILET. Based on solvent-dependence measurements, it is concluded that ILET occurs in a strongly coupled adiabatic limit. In the third section, the anisotropy amplitudes are analyzed taking into account the effects of the bleach. This analysis may speak to the nature of the excited state at the instant of photoexcitation and would seem to suggest the presence of a delocalized (or partially delocalized) wave function in a significant fraction of the excited-state ensemble.

1. Basic Framework. For most time-resolved spectroscopy methods, the magnitude of the polarization anisotropy lies in the range +0.4 to −0.2. The case is not always quite so simple for transient absorption spectroscopy. Figure 12 shows $r(t)$ for Os−BPY as a function of the probe wavelength at early pump−probe delays. Between 390 and 410 nm, $r(t)$ lies outside of the

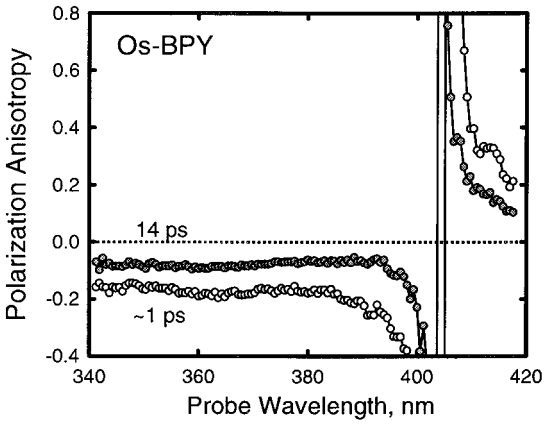

Figure 12. Polarization anisotropy, $r(t)$, as a function of the probe wavelength for Os−BPY in room-temperature CH_3CN. The open and filled circles are the anisotropy observed at 1 and 14 ps after photoexcitation, respectively.

normally expected range. A similar anisotropy spectrum is observed for the mixed ligand complex. There are two potential explanations for this behavior.

One possibility is that the anomalous $r(t)$ values arise from coherence effects. Indeed, a recent ultrafast experiment suggests that these are important in Ru−BPY,[14] especially within the first few hundred femtoseconds after photoexcitation. If coherence effects are the source, then this discontinuity in $r(t)$ should decay on a time scale commensurate with the lifetime of the coherence. This is not the case. The anisotropy spectrum at 14 ps after photoexcitation shows this same behavior. Since this is much longer than one might expect coherence to be maintained, it seems unlikely that it is the source of the anomalously large values observed here.

The more likely cause stems from the different contributions to the transient absorption signal itself. Differential absorption spectra are a superposition of both positive (absorption) and negative (bleach) going signals. Of course, stimulated emission can also contribute to the negative going signal, but that is not an issue in these experiments. When the positive and negative contributions nearly offset each other (i.e., are of similar magnitude) and have different polarization characteristics, the polarization anisotropy will lie outside the normally expected range dictated by eq 3. The origin of this can be seen by writing the parallel and perpendicular absorptions as

$$A_{\parallel}(t) = \alpha_{\parallel}^{T}(t) - \beta_{\parallel}^{T}(t) \tag{5a}$$

$$A_{\perp}(t) = \alpha_{\perp}^{T}(t) - \beta_{\perp}^{T}(t) \tag{5b}$$

where α^T and β^T refer to the *total* absorption and bleach contributions, respectively. (In this formalism, α and β are both positive quantities). The "magic angle" absorption is simply

$$A_{MA}(t) = \frac{1}{3}(\alpha^{T}(t) - \beta^{T}(t)) \tag{6}$$

where $\alpha^T = (\alpha_{\parallel}^T + 2\alpha_{\perp}^T)$ and $\beta^T = (\beta_{\parallel}^T + 2\beta_{\perp}^T)$. The polarization anisotropy measured in a transient absorption experiment is a weighted average of absorption and bleach anisotropies, $\langle r_\alpha(t)\rangle$ and $\langle r_\beta(t)\rangle$, and is given by

$$r(t) = \frac{\alpha^{T}}{\alpha^{T} - \beta^{T}}\langle r_{\alpha}(t)\rangle - \frac{\beta^{T}}{\alpha^{T} - \beta^{T}}\langle r_{\beta}(t)\rangle \tag{7}$$

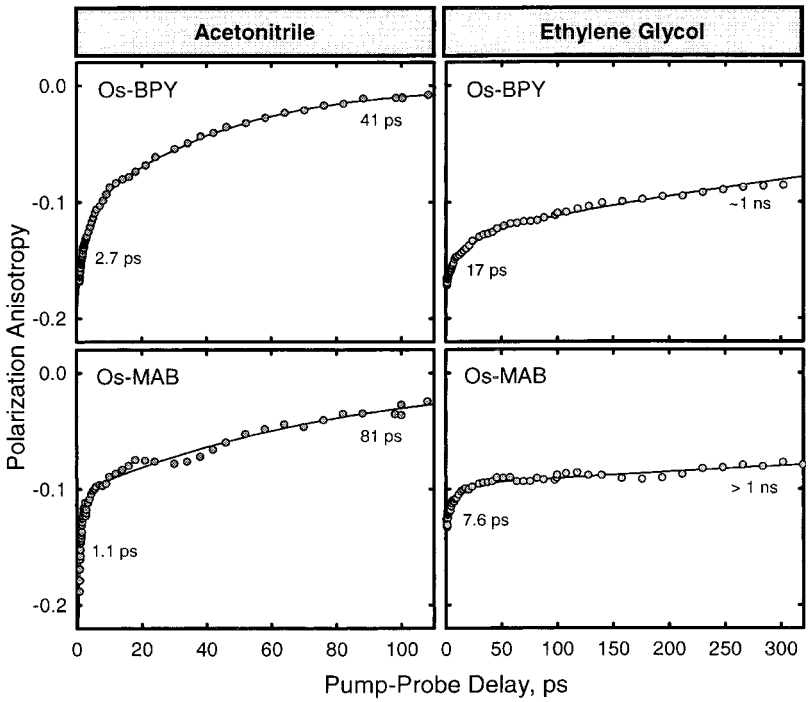

Figure 13. Decay in polarization anisotropy, $r(t)$, detected near the excited-state absorption maximum for Os−BPY and Os−MAB. The details for each panel are as follows: upper-right panel is Os−BPY in CH_3CN, upper-left is Os−BPY in ethylene glycol, lower-right is Os−BPY in CH_3CN, and lower-left is Os−MAB in ethylene glycol. Os−BPY and Os−MAB were excited at 693 and 700 nm, respectively. The decays are displayed for a 370 nm probe wavelength for Os−BPY and 380 nm for Os−MAB. All solvents were at room temperature.

If the absorption has contributions from multiple transitions, then $\langle r_a(t)\rangle$ is a weighted average,

$$\langle r_\alpha(t)\rangle = \sum_i \left(\frac{\alpha_i}{\alpha^T}\right) r_{\alpha,i}(t) \qquad (8)$$

where α_i represents the intensity of the individual transitions whose time-dependent anisotropies are given by $r_{\alpha,i}(t)$. There is a similar expression for the bleach anisotropy. When the bleach and absorption have different polarization characteristics (i.e., $\langle r_\alpha(t)\rangle \neq \langle r_\beta(t)\rangle$), $r(t)$ depends inversely on $(\alpha^T - \beta^T)$, and thus explains (at least qualitatively) why it diverges in the neighborhood of the transient absorption zero crossing. Other groups[14,52,53] have used similar expressions to explain anomalous anisotropy observations in transient absorption experiments.

Equation 7 provides a quantitative framework in which to discuss the anisotropy data. It shows that the observed anisotropy in a transient absorption experiment has contributions from not only the excited-state absorption anisotropy, but also the bleach anisotropy. In addition, through α^T and β^T it depends on the magnitude of the transient absorption signal. Because α^T and β^T could vary with pump−probe delay due to changes in excited-state populations, solvation dynamics, or intramolecular vibrational relaxation, their presence in eq 7 is a way for dynamical processes that *do not involve a change in transition dipole direction* to enter into the anisotropy decay. Thus, polarization anisotropy data collected in a transient absorption experiment must be interpreted with caution in order to avoid reaching erroneous conclusions.

2. Anisotropy Decay. Shown in Figure 13 are the anisotropy decays at 370 nm for Os−BPY and 380 nm for Os−MAB. The left-hand panels were obtained with acetonitrile as the solvent, and the right-hand panels are obtained when the complexes are dissolved in ethylene glycol. The individual points are the experimental data and solid lines are the result of a biexponential fit. All four transients show clear biphasic behavior; the time constants corresponding to the various kinetic components are indicated in the figure. In ethylene glycol, the decay times for the slow components are just estimates, since it is difficult to extract an exact time constant due to the limited pump−probe delay range over which the data were collected.

Kelley and co-workers[15−18] have performed similar polarization anisotropy measurements on both Ru−BPY and Os−BPY in a variety of polar solvents, including CH_3CN and ethylene glycol. The time constants for the slow components are consistent with the values reported by Kelley,[15] in both solvents. The slow component is attributed to rotational diffusion. This process is about a factor of 2 slower in Os−MAB than it is in Os−BPY, which is not surprising given the larger size of the *mab* ligand. When dissolved in ethylene glycol, the rotational diffusion times of both complexes increase, which is consistent with the higher viscosity of that solvent.

While the time constants for the slow components are in qualitative agreement with Kelley's, the decay times for the fast components are not. Kelley reports a 23 ps time constant in CH_3CN,[15] which is about 10 times slower than what we observe (2.7 ps). In ethylene glycol, the difference is less dramatic: 33 ps compared with 17 ps observed in our laboratory.[15] The origin of these discrepancies is unclear, but could be due to the use of a different probe wavelength (345 nm), or the slower time resolution of their instrument (10−15 ps).

There are several potential origins for the fast time component that must be considered. Ultimately we assign it to ILET in the MLCT excited state. However, before proceeding we present the other possibilities, and our arguments for dismissing them. According to eq 7, the observed anisotropy, $r(t)$, has contributions from the absorption and bleach anisotropies ($\langle r_\alpha(t)\rangle$ and $\langle r_\beta(t)\rangle$), and their relative amplitudes (α^T and β^T). In principle, any one of these could be responsible for the fast decay component. Since each can evolve on a different time scale, disentangling the different contributions to $r(t)$ will, generally speaking, be difficult. This task is simplified somewhat for Os−

BPY, where the magic angle signal (and hence α^T and β^T) does not have a 3 ps time component, in either solvent. This implies that the greatest contribution to the time dependence of $r(t)$ must come from $\langle r_\alpha(t)\rangle$ and/or $\langle r_\beta(t)\rangle$. We eliminate $\langle r_\beta(t)\rangle$, because it arises from rotational diffusion of the *unexcited complexes* in the sample, and therefore should only contribute to the slow component of the decay. The fast decay component must, therefore, stem from a dynamical process that takes place in the excited state.

We rule out relaxation through the manifold of low-lying triplet states as the source of this rapid decay. In order for changes in the electronic state to degrade the anisotropy, the transition dipole direction for the excited-state absorption would have to be different in each of the different states. It is unlikely that this is the case, however. The difference between the low-lying ^{3}MLCT states is determined primarily by the electronic configuration on the metal, not the bipyridine ligand. And since the $\pi\pi^*$ absorption is a ligand-localized transition, the direction of its transition dipole is expected to be the same for all of the MLCT states.

We attribute the fast decay component to ILET. This assignment is supported by two observations. The first is that the anisotropy decay times are consistent with the ligand energetics. As mentioned earlier, Os−MAB has a 700 cm^{-1} driving force for *bpy* → *mab* electron transfer, implying that the mixed-ligand complex should have a faster interligand hopping time than its symmetric counterpart, Os−BPY. This is, in fact, the case in both solvents. The second observation is that the decay time in each complex scales with the solvent reorganization time. When either complex is dissolved in ethylene glycol, its fast decay component is 6−7 times slower than it is in CH_3CN. This is generally the case for strongly coupled electron-transfer reactions, implying that the ILET process takes place in the adiabatic limit. This point is pursued further in Section E.

The connection between the observed decay time in $r(t)$ and the ILET time is relatively straightforward. For a totally symmetric complex like Os−BPY, the forward and backward electron-transfer rates are all identical. In this limit ILET rate constant is $^1/_3(k_{obs} - k_r)$, where k_{obs} is the observed anisotropy decay rate and k_r is the rate of decay due to rotational diffusion. Thus, the (2.7 ps)$^{-1}$ and (41 ps)$^{-1}$ decay rates observed in CH_3CN imply a *bpy* → *bpy* ILET time of 8.7 ps, which is about 15 times faster than the 130 ps time previously reported. In ethylene glycol the *bpy* → *bpy* ILET time is 52 ps. For the mixed ligand complex the forward and backward electron-transfer rates are not equal. In the limit that the *mab* → *bpy* electron transfer is slow compared to *bpy* → *bpy* and *bpy* → *mab* electron transfer, the ILET time for transfer to the lower energy *mab* ligand is estimated to be 1.5 ps in CH_3CN and 11 ps in ethylene glycol.

Recent evidence of ILET has been observed in two other mixed-ligand complexes, both of which support our notion of fast ligand−ligand electron transfer. Zewail and co-workers[23] report a 700 fs ILET time in dipyrido[3,2-*a*:2′-3′-*c*]phenazine (dppz) containing Ru(II) compound. Vlcek and co-workers[24] have also observed fast (≈8 ps) ILET in a mixed-ligand Re complex. The primary difference between these two compounds and Os−MAB is that their driving force for electron transfer exceeds that of the osmium complex by a factor 4−5.

3. Anisotropy Amplitudes. Equation 7 provides the framework for a quantitative modeling of the polarization anisotropy data. This analysis shows that $r(t)$ is not only consistent with ILET, but further suggests the presence of a partially *delocalized* excited state at the instant of photoexcitation. These conclusions are based upon an examination of the anisotropy amplitudes associated with the excited-state absorption at early pump−probe delay times.

In the previous section it was established that the excited-state anisotropy decay is biphasic with fast and slow components arising from ILET and rotational diffusion, respectively. In the limit that no other transitions contribute to the excited-state absorption, the absorption anisotropy, $\langle r_\alpha(t)\rangle$, must have the following form:

$$\langle r_\alpha(t)\rangle = a_F^\lambda \exp(-k_F t) + a_S^\lambda \exp(-k_S t) \tag{9}$$

The time constants (k_F and k_S) are associated with the fast and slow decays of the anisotropy, respectively. The corresponding amplitudes (a_F^λ and a_S^λ) are both equal to −0.1 if photoexcitation promotes the electron to the ligand that lies along the polarization vector of the laser (i.e., creates a localized electronic state) and then, through ILET, scrambles among the three ligands. According to eq 7, the absorption anisotropy, $\langle r_\alpha(t)\rangle$, is only one of four contributions to $r(t)$. Thus, to obtain estimates of a_F^λ and a_S^λ, a quantitative modeling of the anisotropy data is required.

Details. The absorption and bleach contributions, α^T and β^T, are treated as input into the model and are determined from the magic angle data (A_{MA}) and ground-state absorption spectrum (A_{GS}). The bleach arises from the hole in the ground-state population, and thus its contribution should (1) appear instantaneously, (2) have a spectral shape that mirrors A_{GS}, and (3) be independent of pump−probe delay. This assumes that the bleach can only decay in amplitude via replenishment of the ground-state population. While this suggests a spectral shape for β^T it says nothing about its magnitude relative to α^T. Thus, to make progress the relative intensity of α^T and β^T (denoted by γ) must be known at a single (reference) wavelength, λ_{rt}, i.e., $\gamma_r = \alpha^T(\lambda_r)/\beta^T(\lambda_r)$. The absorption and bleach contributions are given in terms of A_{MA}, A_{GS}, and γ_r, by

$$\beta^T(\lambda) = \frac{3A_{MA}(\lambda_r)}{\gamma_r - 1}\left(\frac{A_{GS}(\lambda)}{A_{GS}(\lambda_r)}\right) \tag{10}$$

and

$$\alpha^T(\lambda,t) = 3A_{MA}(\lambda,t) + \beta^T(\lambda) \tag{11}$$

where t is the pump−probe delay. Thus, α^T and β^T are determined uniquely, provided that there is an independent measurement of γ_r. On the basis of known spectroscopic data[45,46] we estimate that at 370 nm γ_r is in the neighborhood of 1.8−2.4. By incorporating the magic angle data into the analysis, we account for the changes in the transient absorption signal intensity with pump−probe delay.

The final quantity needed for the anisotropy analysis is $\langle r_\beta(t)\rangle$. Because the bleach arises from the hole in the ground-state population, its anisotropy decays only through the rotational diffusion of the unexcited complexes. To the extent that the ground and excited states have the same rotational diffusion times, the bleach anisotropy takes on a particularly simple form:

$$\langle r_\beta(t)\rangle = r_{\beta 0}^\lambda \exp(-k_S t) \tag{12}$$

where $r_{\beta 0}^\lambda$ is the limiting value of the bleach anisotropy at a particular probe wavelength. We do not have direct experimental evidence from which to calculate an exact value of $r_{\beta 0}^\lambda$, as there is no definitive assignment of the ground-state absorption

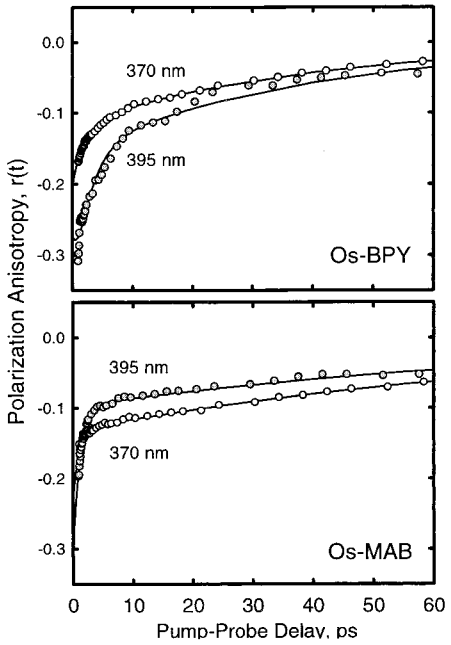

Figure 14. Comparison of experimental data and results of nonlinear least-squares fit to eq 7 as described in the text. The upper panel is for Os−BPY and lower panel is for Os−MAB. The regression involved the simultaneous fit to seven different probe wavelengths, but only two are shown in the figure for clarity.

band near 370 nm. The absorption spectrum is most likely a superposition of transitions that could be ligand-centered, metal-centered, or charge-transfer in nature, and $r_{\beta 0}^{\lambda}$ would be the weighted average of the limiting anisotropies for each transition. Thus, in our analysis, $r_{\beta 0}^{\lambda}$ is treated as an adjustable parameter that must take on a value in the range between −0.2 and +0.4. To simplify the model, we take $r_{\beta 0}^{\lambda}$ to be independent of probe wavelength, i.e., $r_{\beta 0}^{\lambda} \equiv r_{\beta 0}$. While this is probably not entirely correct, over a small spectral range it is a reasonable approximation. The treatment of $r_{\beta 0}$ as an adjustable parameter complicates matters, however, as there is a high correlation between it and a_S^{λ}. Thus, we are forced to examine the results of our analysis for different choices of $r_{\beta 0}$, eliminating those that yield physically unreasonable results. The criterion for excluding some values of $r_{\beta 0}$ is described in more detail below.

Analysis of Os−BPY Anisotropy. We first examined the polarization anisotropy data for Os−BPY. The anisotropy transients at seven probe wavelengths between 360 and 395 nm were simultaneously fit to the model described above. Rather than assign a_F^{λ} and a_S^{λ} exact values, in our analysis we treated both as adjustable parameters that can take on different values at each probe wavelength. For a given γ_r and $r_{\beta 0}$, the concurrent fit of seven transients requires 18 parameters—the excited-state anisotropy amplitudes, a_F^{λ} and a_S^{λ}, at each probe wavelength, and the two decay rates, k_F and k_S. A comparison between the fit to this model and the experimental data for Os−BPY is shown in the top panel of Figure 14. While seven transients were used in the analysis, only the transients at 370 and 395 nm are displayed for clarity. This fit was obtained with $\gamma_r = 2.1$ and $r_{\beta 0} = -0.09$.

Our primary interest is in the values obtained for a_F^{λ} and a_S^{λ}, the anisotropy amplitudes for the excited-state absorption. These are displayed for Os−BPY as the individual points in the upper panel of Figure 15. If the excited-state absorption arises from a single transition (or group of transitions with similar absorption characteristics), then $\langle r_\alpha(t) \rangle$ should be the same at all probe wavelengths throughout the absorption band. As demonstrated

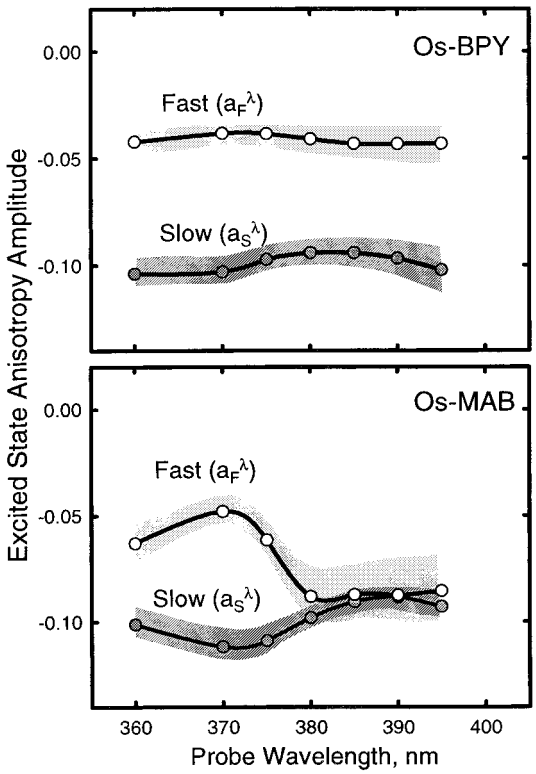

Figure 15. Excited-state anisotropy amplitudes (a_F^{λ} and a_S^{λ} from eq 9) displayed as a function of probe wavelength for Os−BPY (top panel) and Os−MAB (bottom panel). The two sets of points in each panel correspond to the anisotropy amplitudes on the fast and slow decay components. The individual points are obtained with $r_{\beta 0} = -0.09$ and $\gamma_r = 2.1$ (see text for details). The shaded areas illustrate the sensitivity of the analysis to these parameters as discussed in the text.

in the figure, the agreement between different probe wavelengths is reasonably good for both the fast and slow component amplitudes. Not all $r_{\beta 0}$ values yield the same degree of probe wavelength agreement, however, and we use this to eliminate some values of $r_{\beta 0}$. Choosing a different value for $r_{\beta 0}$ has little impact on the amplitude of the fast component (a_F^{λ}), but does influence the results for a_S^{λ}. The examination of a range of $r_{\beta 0}$ values shows that good probe wavelength agreement between the a_S^{λ} values is obtained only for $r_{\beta 0}$ between −0.11 and −0.08, with the best agreement being observed when $r_{\beta 0} = -0.09$. We have also examined the affect that varying γ_r has on the fit results. In contrast to $r_{\beta 0}$, using different values for γ_r only influences a_F^{λ}, the amplitude of the fast component. The sensitivity of this model to the choice of γ_r and $r_{\beta 0}$ is represented by the shaded areas in Figure 15, which correspond to the range of a_F^{λ} and a_S^{λ} values obtained when γ_r is in the range 1.8 to 2.4 and $r_{\beta 0}$ is between −0.11 and −0.08.

The excited-state anisotropy amplitudes obtained from this model are consistent with ILET. The amplitude of the slow component is ≈ −0.1, which is the value that is expected once the photoexcited electron randomizes among the three ligands. The initial anisotropy ($a_F^{\lambda} + a_S^{\lambda}$) is only −0.145. The initial anisotropy for a localized excitation is −0.2, provided that the excited-state absorption is dominated by the bpy^- absorption. In this limit, an initial anisotropy of −0.145 would imply that at the earliest pump−probe delay that can be measured with our apparatus (500 fs) only 63% of the initial population is on the photoselected ligand. This could be evidence for a rapid ILET process that occurs on a time scale that is not resolved in these experiments (<300−500 fs). The mechanism that would lead to such a fast delocalization is not at the moment clear. A

second possibility is that the photoexcitation of the ground-state ensemble produces a mixture of localized and delocalized excited states that arises from a distribution of local solvent environments. The purely localized states would have fast components (a_F^{λ}) equal to -0.1, while for purely delocalized states these would be equal to zero. Because the observed anisotropy is an ensemble average over all the solvent configurations present in the sample, the presence of a reduced anisotropy would imply that in a sizable fraction of the complexes, optical excitation prepares an excited-state wave function that is either delocalized (or partially delocalized) over at least two ligands.

Analysis of Os−MAB Anisotropy. The fit to the Os−MAB data is carried out using the same values for γ_r and $r_{\beta 0}$ that were used in the Os−BPY analysis. The comparison between the fit results and the experimental data is displayed in the lower panel of Figure 14, and the anisotropy amplitudes for the mixed ligand complex are shown in the lower panel of Figure 15. Like Os−BPY, the amplitude of the slow component is approximately -0.1 for all the probe wavelengths in this spectral region. Unlike Os−BPY, however, the amplitude of the fast component does depend on probe wavelength. To the red of 380 nm, where *mab* is the dominant absorber, the amplitude of this component is approximately -0.1; and to the blue of 380 nm, where *bpy* is the dominant absorber, it is around -0.05. This suggests that in the mixed-ligand complex there are two different electronic states produced by optical excitation—one that is localized on the unique ligand (in this case *mab*), and one that is partially delocalized over the other two. As in Os−BPY, this partially delocalized state is probably an ensemble average of localized and delocalized states arising from a distribution of local solvent environments. We must point out, however, that in the Os−MAB complex the time scale for the fast component is such that the amplitude analysis is a bit of an extrapolation. This introduces some uncertainty into the results and thus more experimentation is needed before a definitive conclusion can be reached.

E. Estimation of Ligand−Ligand Electronic Coupling. Taken together, the fast ILET rates and the observation of partial delocalization in the optically prepared electronic state suggests the presence of a large electronic coupling between the ligands. In this section we estimate a value for this coupling based on the driving force dependence of the ILET rate constants measured for the two complexes.

According to electron transfer theory,[54−58] the rate constant for electron transfer is determined by the activation energy (ΔG^*), the electronic coupling (H_{el}), and the solvent reorganization energy (λ). The most common formalisms treat electron transfer in either the adiabatic or the nonadiabatic regime. Rips and Jortner[57,58] extended the theory to include the solvent reorganization time (τ_s) and thereby bridge the two limits, i.e.,

$$k_{ET} = \left(\frac{1}{1+\kappa}\right)\frac{H_{el}^2}{\hbar}\sqrt{\frac{\pi}{\lambda k_B T}}\exp(-\Delta G^*/k_B T) \qquad (13)$$

where the quantity κ, known as the adiabaticity parameter, is given by

$$\kappa = \frac{4\pi H_{el}^2 \tau_s}{\hbar\lambda} \qquad (14)$$

As the electronic coupling increases, the activation energy (ΔG^*) is no longer related to the driving force (ΔG_o) by $\Delta G^* = (\lambda + \Delta G_o)^2/4\lambda$. Brunschwig and Sutin[59] developed an expression for the activation energy in the limit of large H_{el}, i.e.,

$$\Delta G^* = \frac{\lambda}{4} + \frac{\Delta G_o}{2} + \frac{(\Delta G_o)^2}{4(\lambda - 2H_{el})} - H_{el} + \frac{H_{el}^2}{\lambda + \Delta G_o} \qquad (15)$$

Together, eqs 13, 14, and 15 describe the electron-transfer rate constant for electronic couplings that span the adiabatic and nonadiabatic limits. Electron-transfer reactions that take place in the conventional nonadiabatic limit have $\kappa \ll 1$ and the well-known expression for the electron-transfer rate constant is recovered.[57] For electron-transfer reactions in the adiabatic limit, where $\kappa \gg 1$, the preexponential factor scales with the inverse of the solvent reorganization time, $1/\tau_s$. We have modeled our ILET data using these equations, and for the analysis we need estimates of both the reorganization time (τ_s) and reorganization energy (λ).

Solvent reorganization times have been measured for a number of solvents. These experiments show that typically there is more than one time scale associated with solvent motion, even in simple solvents. Acetonitrile exhibits two characteristic time scales: fast "inertial" motion (sub-100 fs) and slower "diffusive" motion (2−3 ps).[51] In our analysis we use an *average* reorganization time of 0.5 ps. An estimate of the reorganization energy can be obtained from dielectric continuum theory. Brunschwig and Sutin[60] developed a general expression for the outer-sphere reorganization energy arising from the redistribution of charge within a spherical cavity. For the case of interligand electron hopping, the outer-sphere contribution to λ is given by

$$\lambda = \frac{1}{2a}\left[\left(\frac{1}{D_{in}} - \frac{1}{D_S}\right)\sum_{n=1}^{\infty} g_n(\Delta e)\left(1 + \left(\frac{n}{n+1}\right)\frac{D_{in}}{D_S}\right)^{-1} - \left(\frac{1}{D_{in}} - \frac{1}{D_{OP}}\right)\sum_{n=1}^{\infty} g_n(\Delta e)\left(1 + \left(\frac{n}{n+1}\right)\frac{D_{in}}{D_{OP}}\right)^{-1}\right] \qquad (16)$$

where D_{in}, is the dielectric constant inside the cavity (usually taken to be unity), D_S and D_{OP} are the static and optical dielectric constants, and $g(\Delta e)$ is

$$g_n(\Delta e) = 2(\Delta e)^2\left(\frac{r}{R}\right)^{2n}[1 - P_n(\cos(\theta))] \qquad (17)$$

Here r is the distance of the photoexcited electron from the metal center, R is the radius of the cavity, and θ is the angle between the ligands (120°). On the basis of reasonable estimates for each of these parameters, we estimate outer-sphere contribution to λ to be in the range of 2000−3500 cm^{-1}. The Meyer group[61] has observed a broad absorption band in the MLCT excited state near 4700 cm^{-1}. This band could be the result of a ligand-to-ligand optical excitation, and could thus yield a direct measure of the reorganization energy.

For a given choice of λ, we can estimate H_{el} using eqs 13−15. Shown in Figure 16 are the ILET rate constants for Os−BPY and Os−MAB as a function of the electron-transfer driving force. The solid line is calculated from these equations using λ = 3500 cm^{-1}, τ_s = 0.5 ps, and H_{el} = 570 cm^{-1}. We have explored a range of values for λ in a similar manner. When λ is between 1800 and 4700 cm^{-1}, our analysis suggests that H_{el} is between 200 and 900 cm^{-1}. In all cases, the adiabaticity parameter, κ, is much greater than 1, suggesting that ILET takes place in the adiabatic limit.

IV. Conclusions

We have used femtosecond polarization anisotropy methods to investigate the interligand electron transfer (ILET) dynamics

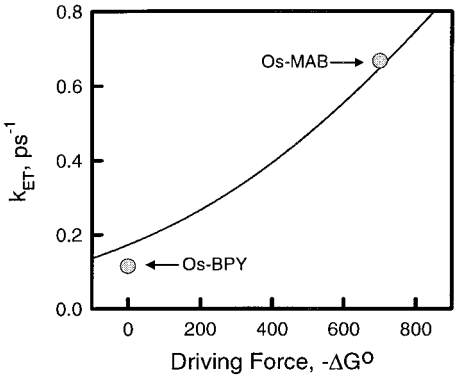

Figure 16. Electron-transfer rate constant as function of driving force. Points are experimental observation for Os−BPY and Os−MAB. The line is calculated from eq 14−16 with $\lambda = 3500$ cm^{-1} and $H_{el} = 570$ cm^{-1}.

in Os−BPY and one of its mixed-ligand analogues, Os−MAB. Our data show that ILET in Os−BPY has a rate constant of $(8.1\ ps)^{-1}$, much faster than previously thought. There is a driving force for ILET in the Os−MAB complex that increases the ILET rate constant to $(1.5\ ps)^{-1}$. Examination of the ILET process in different solvents shows that the ILET time scales with the solvent reorganization time, implying that electron transfer occurs in the strongly coupled (adiabatic) limit. An analysis of the anisotropy amplitudes suggests that a substantial portion of the excited-state ensemble is created with delocalized (or partially delocalized) excited-state wave functions.

Acknowledgment. Funding for this project was provided by The University of North Carolina at Chapel Hill and The Research Corporation (RI0048). We also thank T. J. Meyer for a number of stimulating discussions.

References and Notes

(1) Meyer, T. J. *Pure Appl. Chem.* **1986**, *50*, 1293.
(2) Casper, J. V.; Meyer, T. J. *J. Am. Chem. Soc.* **1983**, *105*, 5583.
(3) Casper, J. V.; Kober, E. M.; Sullivan, B. P.; Meyer, T. J. *J. Am. Chem. Soc.* **1982**, *104*, 630.
(4) Van Houten, J.; Watts, R. J. *J. Am. Chem. Soc.* **1976**, *98*, 4853.
(5) Van Houten, J.; Watts, R. J. *Inorg. Chem.* **1978**, *17*, 3381.
(6) Bradley, P. G.; Kress, N.; Hornberger, B. A.; Dallinger, R. F.; Woodruff, W. H. *J. Am. Chem. Soc.* **1981**, *103* (25), 7441−7446.
(7) Mabrouk, P. A.; Wrighton, M. S. *Inorg. Chem.* **1986**, *25* (4), 526−531.
(8) Vlcek, A. *Coord. Chem. Rev.* **2000**, *200*−*202*, 933−977.
(9) Ferguson, J.; Herren, F.; Krausz, E.; Maeder, M.; Vrbancich, J. *Coord. Chem. Rev.* **1985**, *64*, 21.
(10) Ferguson, J.; Herren, F. *Chem. Phys.* **1983**, *76*, 45−59.
(11) Creutz, C.; Chou, M.; Netzel, T. L.; Okumura, M.; Sutin, N. *J. Am. Chem. Soc.* **1980**, *102* (4), 1309−1319.
(12) Damrauer, N. H.; Cerullo G.; Yeh, A.; Boussie, T. R.; Shank, C. V.; McCusker, J. K. *Science* **1997**, *275*, 54−57.
(13) Damrauer, N. H.; McCusker, J. K. *J. Phys. Chem. A* **1999**, *103* (42), 8440−8446.
(14) Yeh, A. T.; Shank, C. V.; McCusker, J. K. *Science* **2000**, *289*, 935−938.
(15) Cushing, J. P.; Butoi, C.; Kelley, D. F. *J. Phys. Chem. A* **1997**, *101* (39), 7222−7230.
(16) Pogge, J. L.; Kelley, D. F. *Chem. Phys. Lett.* **1995**, *238*, 16−24.
(17) Malone, R. A.; Kelley, D. F. *J. Chem. Phys.* **1991**, *95* (12), 8970−8976.
(18) Cooley, L. F.; Bergquist, P.; Kelley, D. F. *J. Am. Chem. Soc.* **1990**, *112*, 2612−2617.
(19) Yabe, T.; Orman, L. K.; Anderson, D. R.; Yu, S.-C.; Xu, X.; Hopkins, J. B. *J. Phys. Chem.* **1990**, *94* (18), 7128−7132.
(20) Chang, Y. J.; Xu, X.; Yabe, T.; Yu, S.-C.; Anderson, D. R.; Orman, L. K.; Hopkins, J. B. *J. Phys. Chem.* **1990**, *94* (2), 729−736.
(21) Carroll, P. J.; Brus, L. E. *J. Am. Chem. Soc.* **1987**, *109*, 7613−7616.
(22) Carlin, C. M.; DeArmond, M. K. *J. Am. Chem. Soc.* **1985**, *107*, 53−57.
(23) Önfelt, B.; Lincoln, P.; Nordén, B.; Baskin, J. S.; Zewail, A. H. *Proc. Natl. Acad. Sci. U.S.A.* **2000**, *97* (11), 5708−5713.
(24) Liard, D. J.; Vlcek, A. *Inorg. Chem.* **2000**, *39* (3), 485−490.
(25) Hagfeldt, A.; Grätzel, M. *Chem. Rev.* **1995**, *95*, 49−68.
(26) Bignozzi C. A.; Schoonover, J. R.; Scandola, F. *Prog. Inorg. Chem.* **1997**, *44*, 1−95.
(27) Balzani, V.; Credi, A.; Scandola, F. *Transition Metals in Supramolecuar Chemistry*; Fabbrizzi, L., Poggi, A., Eds.; Kluwer: The Netherlands, 1994; p 1.
(28) Fleming, C. N.; Maxwell, K. A.; Meyer, T. J.; Papanikolas, J. M. *J. Am. Chem. Soc.* **2001**, *123* (42), 10336−10347.
(29) Smith, G. D.; Maxwell, K. A.; Desimone, J. M.; Meyer, T. J.; Palmer, R. A. *Inorg. Chem.* **2000**, *39* (5), 893−898.
(30) Maxwell, K. A. Doctoral Dissertation, University of North Carolina at Chapel Hill, Chapel Hill, NC, 1999.
(31) Kober, E. M.; Sullivan, B. P.; Meyer, T. J. *Inorg. Chem.* **1984**, *23* (14), 2098−2104.
(32) Riesen, H.; Wallace, L.; Krausz, E. *Inorg. Chem.* **2000**, *39*, 5044−5052.
(33) Riesen, H.; Krausz, E. *Chem. Phys. Lett.* **1998**, *287*, 388−394.
(34) Karka, L.; Hupp, J. T. *Inorg. Chem.* **1997**, *36* (15), 3318−3321.
(35) Oh, D. H.; Boxer, S. G. *J. Am. Chem. Soc.* **1989**, *111*, 1131−1133.
(36) Yersin, H.; Strasser, J. *Coord. Chem. Rev.* **2000**, *208*, 331−364.
(37) Yersin, H.; Humbs, W. *Inorg. Chem.* **1999**, *38*, 5820−5831.
(38) Humbs, W.; Strasser, J.; Yersin, H. *J. Lumin.* **1997**, *72*−*74*, 677−678.
(39) Huber, P.; Yersin, H. *J. Phys. Chem.* **1993**, *97* (49), 12705−12709.
(40) Riesen, H.; Wallace, L.; Krausz, E. *J. Chem. Phys.* **1995**, *102* (12), 4823.
(41) Demas, J. N.; Crosby, G. A. *J. Phys. Chem.* **1971**, *75*, 991.
(42) Demas, J. N.; Crosby, G. A. *J. Am. Chem. Soc.* **1971**, *93*, 2841.
(43) Kober, E. M.; Meyer, T. J. *Inorg. Chem.* **1984**, *23*, 3877−3886.
(44) Lumpkin, R. S.; Kober, E. M.; Worl, L. A.; Murtaza, Z.; Meyer, T. J. *J. Phys. Chem.* **1990**, *94*, 239−243.
(45) Noble, B.; Peacock, R. D. *Inorg. Chem.* **1996**, *35* (6), 1616−1620.
(46) Noble, B.; Peacock, R. D. *Spectrochim. Acta, Part A* **1990**, *46* (3), 407−412.
(47) Braterman, P. S.; Harriman, A.; Heath, G. A.; Yellowlees, L. J. *J. Chem. Soc., Dalton Trans.* **1983**, 1801−1803.
(48) Heath, G. A.; Yellowlees, L. J.; Braterman, P. S. *Chem. Commun.* **1981**, 287−289.
(49) Konig, E.; Kremer, S. *Chem. Phys. Lett.* **1970**, *5*, 87.
(50) Decurtins, S.; Felix, F.; Ferguson, J.; Güdel, H. U.; Ludi, A. *J. Am. Chem. Soc.* **1980**, *102* (12), 4102−4107.
(51) Passino, S. A.; Nagasawa, Y.; Fleming, G. R. *J. Chem. Phys.* **1997**, *107* (16), 6094−6108.
(52) Jonas, D. M.; Lang, M. J.; Nagasawa, Y.; Joo, T.; Fleming, G. R. *J. Phys. Chem.* **1996**, *100*, 12660−12673.
(53) Martinsson, P.; Oksanen, J. A. I.; Hilgendorff, M.; Hynninen, P. H.; Sundstrom, V.; Akesson, E. *Chem. Phys. Lett.* **1999**, *309* (5−6), 386−394.
(54) Sutin, N. *Adv. Chem. Phys.* **1999**, *106*, 7−33.
(55) Newton, M. D.; Sutin, N. *Annu. Rev. Phys. Chem.* **1984**, *35*, 437−480.
(56) Barbara, P. F.; Meyer, T. J.; Ratner, M. A. *J. Phys. Chem.* **1996**, *100* (31), 13148−13168.
(57) Rips, I.; Jortner, J. *J. Chem. Phys.* **1987**, *87* (4), 2090−2105.
(58) Rips, I.; Jortner, J. *J. Chem. Phys.* **1987**, *87* (11), 6513−6519.
(59) Brunschwig, B. S.; Sutin, N. *Coord. Chem. Rev.* **1999**, *187*, 233−254.
(60) Brunschwig, B. S.; Ehrenson, S.; Sutin, N. *J. Phys. Chem.* **1987**, *91*, 1 (18), 4714−4723.
(61) Meyer, T. J. Personal communication.

ARTICLES

Interligand Electron Transfer Dynamics in $[Os(bpy)_3]^{2+}$: Exploring the Excited State Potential Surfaces with Femtosecond Spectroscopy

George B. Shaw, David J. Styers-Barnett, Erika Z. Gannon, Jeremy C. Granger, and John M. Papanikolas*

Department of Chemistry, University of North Carolina at Chapel Hill, Chapel Hill, North Carolina 27599-3290

Received: August 11, 2003; In Final Form: March 16, 2004

Femtosecond transient absorption studies of $[Os(bpy)_3]^{2+}$ have been performed to gain new insights into the excited-state dynamics. Experiments were performed for a series of excitation wavelengths throughout both the singlet and triplet metal-to-ligand charge transfer (MLCT) bands. The dynamics are probed via the $\pi-\pi^*$ transition on the bpy^- anion at 370 nm. Time scales for interligand electron transfer (ILET) and vibrational cooling are extracted from the amplitude and anisotropy of the excited state absorptions. The ILET rate has been measured as a function of temperature and, from these data, estimates for the electron transfer activation energy and ligand−ligand coupling are made. Our data also provide insight into the vibrational cooling dynamics within these large complexes, suggesting that vibrational cooling occurs only when exciting into the singlet MLCT state, after intersystem crossing. It appears that photoexcitation within the triplet MLCT absorption produces molecules that are vibrationally cold, even for excitation at the blue edge of the absorption band.

I. Introduction

The photophysics of Ru(II) and Os(II) polypyridine complexes have been studied for more than three decades.[1−9] The motivation for this research has largely been driven by the use of $[Ru(bpy)_3]^{2+}$ and $[Os(bpy)_3]^{2+}$ (bpy = 2,2′-bipyridine) and their derivatives as photosensitizers in the fields of solar energy conversion,[10−12] photonic devices,[13−15] and molecular electronics.[16,17] Through this extensive investigation, the properties of the lowest energy triplet metal-to-ligand charge-transfer (^{3}MLCT) excited state and its evolution at long times after photoexcitation have been well-characterized. Only recently, however, have significant strides been taken toward understanding the behavior of these complexes at very early times after photoexcitation. Following ^{1}MLCT excitation, intersystem crossing (ISC) to the triplet manifold is the dominant relaxation pathway (i.e. near unit efficiency) prior to ground-state recovery via phosphorescence. Recent ultrafast experiments have suggested that ISC occurs in $[Ru(bpy)_3]^{2+}$ within a few hundred femtoseconds after photoexcitation,[18,19] though certain aspects remain open to interpretation.[20]

Despite the recent advances made in developing a comprehensive picture of the evolution of the excited state from the moment of photoexcitation, certain fundamental questions remain largely unanswered. It is well-established that a polar solvent localizes the electron distribution on a single ligand at long times after photoexcitation.[21,22] Whether a localized or delocalized excited state is initially produced is still a matter of debate. In the last two decades, compelling arguments have been made for both cases,[23−33] mostly investigating Ru(II) compounds. Nevertheless, this debate continues. Recently, McCusker and co-workers studied $[Ru(bpy)_3]^{2+}$ in nitrile solvents using ultrafast absorption anisotropy measurements.[34] They proposed that photoexcitation produced an initially delocalized ^{1}MLCT state that quickly localized on a single ligand due to nondiffusive solvation dynamics.

A previous contribution from our laboratory[35] discussed femtosecond transient absorption and absorption anisotropy experiments that were used to investigate the excited-state dynamics in $[Os(bpy)_3]^{2+}$ and a mixed ligand Os(II) complex that has two bipyridine ligands and one amide functionalized bipyridine. In those experiments, the complexes were excited at the far red edge of the ground state absorption spectrum. This allowed us to populate the lowest optically accessible ^{3}MLCT state, and circumvent the ISC process. In $[Os(bpy)_3]^{2+}$, it was found that the photoexcited electron was able to incoherently hop among the three bipyridines with an interligand electron transfer (ILET) time of $\tau_{ILET} = 8.1$ ps. We also found evidence suggesting that the distribution of local solvent configurations at the instant of photoexcitation gave rise to a mixture of localized and delocalized excited states.

This paper describes several extensions to our initial work that enhance our understanding about the excited-state potential surfaces in polar solvents. Molecular dynamics simulations were carried out to gain quantitative insight into the heterogeneity of the solvent environment at the moment of photoexcitation. The results support our previous findings that there should be a mixture of localized and delocalized excited states due to this inhomogeneity. These simulations also strengthen the conclusions drawn from the optical studies described in the current

* Address correspondence to this author.E-mail: john_papanikolas@unc.edu.

10.1021/jp0363850 CCC: $27.50
Published on Web 05/13/2004

work. We have measured the ILET rate constant as a function of temperature to determine the activation energy for electron transfer (850 cm^{-1}), and combined this with estimates of the reorganization energy to determine the ligand−ligand coupling (300−400 cm^{-1}). We have extended our ultrafast studies to other excitation wavelengths throughout the ^{1}MLCT and ^{3}MLCT absorption bands. These experiments explore higher energy portions of the excited-state potential surfaces, and provide insight into the partitioning of optical excitation energy between molecular vibrations (inner sphere) and solvent interactions (outer sphere). They indicate that the absorption spectra in polar solvents should be viewed, at least qualitatively, as overlapping absorption bands that correspond to the promotion of the electron to ligands whose energies are split by the inhomogeneous solvent environment. In short, excitation at the blue edge of the absorption band corresponds to promoting the system to an *upper* Marcus surface. Excitation into the ^{1}MLCT absorption band is followed by rapid intersystem crossing to form a vibrationally hot ^{3}MLCT state, which then cools with a time constant of 16 ps.

II. Experimental Section

The experimental apparatus has been described in detail elsewhere,[35,36] so only a brief description is provided here. The transient absorption spectrometer is based on a commercially available ultrafast laser system (Clark CPA-2001). Femtosecond pulses are produced by an erbium-doped fiber ring oscillator and injected into a chirped pulse Ti:sapphire regenerative amplifier. The amplifier, which is pumped by a frequency doubled, Q-switched Nd:YAG laser, produces 120 fs laser pulses at 775 nm at 1 kHz with pulse energies of approximately 950 μJ/pulse. The amplified output is split into two beams by an uncoated glass window.

The larger (96%) transmitted portion is directed into an optical parametric amplifier (OPA) where the tunable light used for photoexcitation is produced. For the ^{3}MLCT excitations the second harmonic of the OPA was used to generate light at 693, 675, 650, 625, and 580 nm with 5−10 μJ/pulse. The 500 nm excitation light (0.7 μJ/pulse) was generated by sum-frequency mixing of the fundamental at 1409 nm and the left over 775 nm light from the OPA, and the 440 nm excitation light was produced by fourth harmonic generation. For all excitation wavelengths, the pump was focused to a spot size of ∼500 μm at the sample. The polarization of the pump beam was controlled with an achromatic $\lambda/2$ waveplate. To account for fluctuations in laser intensity during the course of data collection, after the sample the pump was directed into a photodiode whose voltage was continuously monitored for power normalization.

The probe beam is generated from the weak (4%) reflected fraction of the amplifier output that is directed into a corner retroreflector mounted on a computer-controlled translation stage. The beam is focused into a 6 mm thick CaF_2 window to generate a white light continuum that is then collimated by an achromatic lens. The continuum is attenuated and split into two beams of nearly equal intensity by taking the front and rear surface reflections from a 25 mm thick uncoated quartz window. The resulting beams are designated "signal" and "reference". Both beams are focused by 300 mm lenses to have a 150 μm spot size at the sample. While both beams pass through the sample, only the signal beam is spatially overlapped at the sample with the pump beam. Both signal and reference beams are simultaneously directed into a 270 mm focal length spectrograph, dispersed by a 1200 line/mm holographic grating and detected by a 1024 × 256 pixel (25.4 × 6.35 mm) liquid nitrogen cooled CCD array. The spectrograph has a reciprocal linear dispersion of 3.1 nm/mm and the binning of the CCD has 128 pixels over the 25.4 mm dimension of the chip. Although we operate the device in a slit-less manner, the signal and reference beams are focused to a 0.5 mm spot at the entrance of the spectrograph—in essence, a virtual slit—resulting in a spectral resolution of 1.48 nm. The TA apparatus is capable of measuring a 77 nm segment of the transient absorption spectrum centered anywhere between 350 and 1000 nm with a sensitivity of better than 1 mOD.

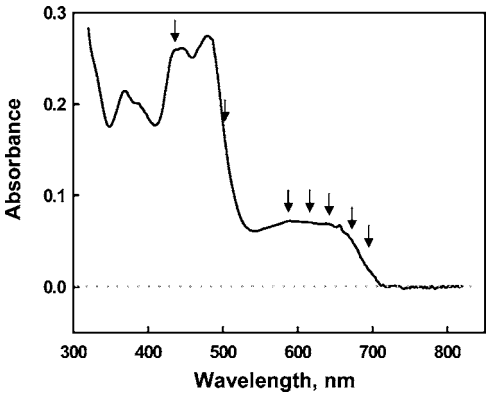

Figure 1. Ground-state absorption spectrum of $[Os(bpy)_3]^{2+}$. Photoexcitation wavelengths for TA experiments are indicated.

For the temperature-dependent studies, a home-built thermal regulator was designed. It consists of an aluminum block that was machined to accept our 2 mm path length sample cuvette and provide a small window to permit the pump, signal, and reference beams to pass through while ensuring maximum contact with the rest of the cuvette. Water (or a water/ethylene glycol mixture) pumped from a temperature-controlled circulating bath flows through channels machined in the aluminum block to maintain the temperature of the system. A thermocouple attached to the cuvette near where the laser beams pass through permits accurate measurement of the solution temperature. Sufficient time for thermal equilibration of the system was allowed before experiments were performed.

The $[Os(bpy)_3]^{2+}$ samples were obtained in crystal form (as PF_6^- salts) as gifts from Thomas J. Meyer and were used without further purification. Spectroscopic grade acetonitrile was used as obtained from the vendor (Burdick and Jackson). All experiments were performed on solutions whose concentrations were adjusted to give an optical density of ∼0.3 OD in a 2 mm path length sample cell.

III. Results and Discussion

The ground-state absorption spectrum for $[Os(bpy)_3]^{2+}$ is shown in Figure 1. There are two relevant MLCT absorptions in the visible region: an intense singlet absorption band centered at 450 nm and a weaker triplet absorption extending from 520 to 700 nm. Photoexcitation to the ^{1}MLCT state is followed by rapid and efficient intersystem crossing to the ^{3}MLCT state manifold. This paper describes femtosecond transient absorption studies that probe the excited-state relaxation dynamics in $[Os(bpy)_3]^{2+}$ following photoexcitation at both singlet and triplet excitation wavelengths. Seven different photoexcitation wavelengths were used, and these are indicated by the arrows in Figure 1.

A. Molecular Dynamics Simulations of Solvent Inhomogeneity: Implications for the Optically Prepared Excited State. The degree of charge delocalization in the optically prepared MLCT state is determined by the relative magnitudes

of the electronic coupling between the bipyridine ligands and the electrostatic asymmetry presented by the solvent environment. The electronic coupling mixes the π^*-orbitals on the three ligands yielding a delocalized excited state. For an isolated molecule, or one embedded in a symmetric environment, the ligand orbitals are nearly degenerate and a weak electronic coupling is sufficient to achieve complete delocalization. The situation may be quite different for a complex embedded in a polar solvent. The electrostatic asymmetry presented by the local environment will lift the degeneracy of the three ligands, and if the asymmetry is large enough, the electronic states will have localized charge distributions. The degree of charge localization in the *optically prepared* state will depend on the solvent configuration surrounding the ground-state complex at the instant of photon absorption. Thus, the relevant question is: what is the distribution of solvent configurations that surround the *ground state* complex? The $[Os(bpy)_3]^{2+}$ ground state has no dipole moment and so (on average) it is surrounded by a symmetric electrostatic solvent environment. This should not be interpreted to imply that at the instant of photoexcitation all of the complexes in the ensemble experience a truly symmetric solvent environment, as the electrostatic field produced by the solvent cage surrounding the ground-state complex could possess a considerable amount of inhomogeneity. To address the question of environmental inhomogeneity, we have performed molecular dynamics simulations on a dipolar solvent interacting with the electronic ground state of $[Os(bpy)_3]^{2+}$.

The computer model consists of a transition metal complex surrounded by 504 dipolar solvent molecules. The potential was composed of two parts, i.e.

$$V_{\text{total}} = V_{\text{ion-solvent}} + V_{\text{solvent-solvent}} \tag{1}$$

The first term represents the interaction between the ion and the solvent and the second term is the pairwise intermolecular potential between solvent molecules. Briefly, the interaction potential describes each solvent molecule by six Lennard-Jones sites located at the atomic centers, and the acetonitrile dipole moment is represented by three partial charges placed on the nitrogen (-0.43), central carbon ($+0.28$), and methyl carbon ($+0.15$). The $[Os(bpy)_3]^{2+}$ complex is represented by a Lennard-Jones sphere with a $+2$ charge located at its center. The sphere and 504 solvent molecules were placed in a box with periodic boundary conditions. Classical trajectories were calculated with the AMBER molecular simulation package. Trajectories at constant pressure and temperature were run for 2.8 ns, with the first 1.4 ns being used to establish equilibrium and the latter 1.4 ns used to sample the solvent configurations.

The degree of solvent inhomogeneity is ascertained by comparing the electrostatic potential produced by the solvent at each of the three bipyridine ligands and the metal center. For the ligands, the potential is sampled over three points situated within the π-framework to account for the spatial extent of the MLCT charge distribution. For each configuration of the solvent we calculate the quantity

$$\Delta E_j = (3U_{\text{M}} - U_j) - 2U_{\text{M}} \tag{2}$$

where U_j and U_{M} are the electrostatic potentials observed at the jth ligand and the metal center, respectively. The first term (in parentheses) is the excited-state solvation energy for the case where the photoexcited electron is promoted to the jth ligand while keeping the solvent frozen in a configuration appropriate for the ground electronic state. The second term is the solvation energy of the ground state, and thus ΔE_j is the change in solvation energy that is associated with moving an electron from the metal center to the jth ligand. Figure 2 shows the distributions for the largest and smallest energy gaps. Energy differences in excess of 550 cm^{-1} are observed in approximately 65−70% of the ensemble. This suggests that while the majority of systems have localized excited states, there is still a substantial fraction of the ensemble in which the excited state is delocalized over two or more ligands at the instant of photon absorption, in accord with our previous conclusion. The simulations also suggest that the solvent induces an energy separation that is on average 2500 cm^{-1} between the lowest energy ligand and highest energy ligand, a value that is comparable to the spectral width of the triplet absorption band.

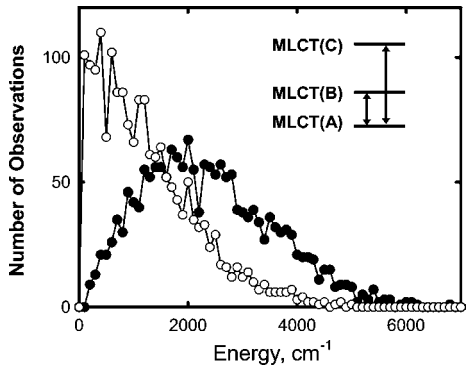

Figure 2. Distributions in the solvent induced energy splitting between ligands. Open circles show the smallest energy gap, and solid circles show the largest. The inset represents the energies of the three bipyridine ligands: MLCT(A) is the ligand with the lowest energy solvent configuration (i.e. the best solvated); MLCT(C) is the ligand with the highest energy solvent configuration; and MLCT(B) is intermediate.

Complexes residing in highly asymmetric solvent environments will exhibit three separate optical transitions. Photoexcitation at the red edge of the absorption band places the electron on the lowest energy ligand, i.e. the one with the most favorable solvent configuration. Excitations to the ligands with less favorable solvent configurations occur at higher energy. If the average value of the largest gap is 2500 cm^{-1}, then excitation to the highest energy ligand in the *triplet* absorption band would be in the vicinity of 600 nm, the blue edge. Because the solvent is not positioned appropriately for this MLCT charge distribution, it will rapidly reorganize. Thus, at higher photon energies, excess excitation energy could be directly placed into the solvent, rather than into molecular vibrations. The implications of this are discussed further in Section C.

B. Transient Absorption Studies. The excited-state dynamics are initiated by photoexcitation of $[Os(bpy)_3]^{2+}$ to a MLCT state with a femtosecond laser pulse and probed through a ligand-localized $\pi-\pi^*$ transition on the bipyridine radical anion (bpy^-) that is centered at 370 nm. The experiments described in this paper focus on both the changes in the *magic angle amplitude*, A_{MA}, and the *absorption anisotropy*, $r(t)$, of the excited-state absorptions. In this work, both of these quantities are derived from the transient spectra obtained with parallel and perpendicular pump−probe polarization conditions., i.e.

$$A_{\text{MA}} = \frac{1}{3}(A_{\parallel} + 2A_{\perp}) \tag{3}$$

$$r(t) = \frac{A_{\parallel} - A_{\perp}}{A_{\parallel} + 2A_{\perp}} \tag{4}$$

The magic angle signal reflects changes in the shape of the excited-state absorption band (e.g. due to changes in population),

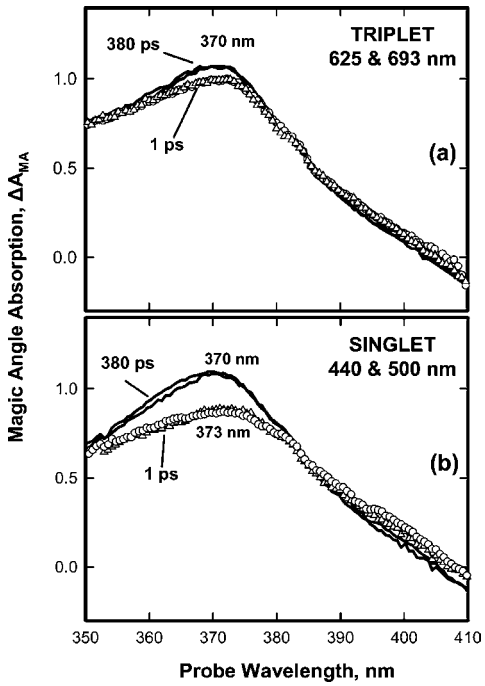

Figure 3. Magic angle transient absorption spectra (ΔA_{MA}) observed at 380 (—) and 1 ps (Δ, ○) after photoexcitation of $[Os(bpy)_3]^{2+}$ in room temperature acetonitrile: (a) spectra for ^{3}MLCT excitation and (b) spectra for ^{1}MLCT excitation.

while the anisotropy reflects changes in the transition dipole direction. Processes that alter the orientational distribution of the probe transition dipoles will lead to a decay in the magnitude of $r(t)$. In molecular systems rotational diffusion is the most common mechanism.

In the MLCT excited state of $[Os(bpy)_3]^{2+}$, ILET will also alter the direction of the probe transition dipole, and hence contribute to the anisotropy decay. The MLCT excitations are polarized along the metal−ligand axes, as long as the environmental heterogeneity is great enough to produce localized excited states, and the probe transition dipole is oriented along the long axis of the bipyridine ligand.[37] Because the pump and probe transition dipoles are orthogonal to each other, stronger excited-state absorption is observed when the probe beam is polarized perpendicular to that of the pump beam. From eq 4 it follows that the initial anisotropy value is negative, but with increasing time the system evolves to an isotropic one where the final anisotropy value is zero.

1. Magic Angle. Magic angle transient absorption spectra obtained at four different excitation wavelengths are displayed in Figure 3. Two spectra are shown for each excitation wavelength, one obtained at 1 ps and the other at 380 ps after photoexcitation. For clarity we present the data in two plots. The upper panel depicts the magic angle spectra resulting from ^{3}MLCT excitation (625 and 693 nm), while the lower one shows the magic angle spectra for ^{1}MLCT excitation (440 and 500 nm). The evolution of the spectra between these two temporal extremes is depicted in the contour plots shown in Figure 4, which show the transient absorption intensity as a function of both the pump−probe delay (*y*-axis) and probe wavelength (*x*-axis). Pump−probe delay (*y*-axis) is given on a logarithmic scale to permit inclusion of all transient spectra.

When the complex is excited in the triplet absorption band, only a slight evolution of the excited-state spectrum is observed. For both the 693 and 625 nm data, there is a small (∼5−6%) growth of intensity at the peak of the $\pi-\pi^*$ absorption from 1 (Δ and ○) to 380 ps (—). Additionally, there is a slight decay of intensity toward the red edge of the absorption (∼385 to 410 nm). In the plots shown in Figure 4a,b, a fast (<1 ps) growth of the absorption is the only discernible evolution of these two surfaces. This is also the case for each of the triplet excitation wavelengths studied (625, 650, 675, and 693 nm).

By contrast, the ^{1}MLCT excitations in Figure 3b exhibit a significant blue shift, as well as a large (∼25−30%) growth of signal intensity at the peak of the $\pi-\pi^*$ absorption. The transient spectra at 1 ps for the 500 (Δ) and 440 nm (○) excitations have a peak of the $\pi-\pi^*$ absorption centered at 373 nm. In the 380 ps limiting spectra (—), the peak of the absorption has shifted to 370 nm and the band has noticeably narrowed. This reshaping of the transient spectra takes place during the first 30−45 ps after photoexcitation (Figure 4c,d). Kinetic analysis reveals two time components. The fast time component is comparable to the subpicosecond evolution observed following triplet excitation. Since this fast evolution is observed at all excitation wavelengths, it is reasonable to assume that it stems from a common source, although its exact origin is at the moment unclear. The slow time component is observed only for the two singlet excitations, and is approximately 16 ps. While both the 500 and 440 nm excitations exhibit similar time scales, the *degree* of spectral shift differs. Difference spectra obtained by subtracting the 380 ps limiting spectrum from the 3.5 ps spectrum are shown in Figure 5 for each of the photoexcitation wavelengths. The difference spectra at 3.5 ps are chosen because by this time the fast (<1 ps) evolution is over and only the slow changes are evident. Both of the singlet excitations show significant spectral changes and the higher energy excitation (440 nm) seems to exhibit a slightly greater change than the lower energy excitation (500 nm).

One plausible interpretation of this observation is that the spectral blue shift is a signature of intersystem crossing in $[Os(bpy)_3]^{2+}$. If this were correct, it would make the ISC time in $[Os(bpy)_3]^{2+}$ about 100 times slower than the time scale measured in $[Ru(bpy)_3]^{2+}$. The spin−orbit coupling in $[Os(bpy)_3]^{2+}$ is even stronger than that in $[Ru(bpy)_3]^{2+}$ and since there is no significant structural rearrangement in the MLCT excited states, it is difficult to imagine why the ISC should be any slower in $[Os(bpy)_3]^{2+}$. In addition, one would anticipate that if it were the result of ISC, the magnitude of the spectral shift would be independent of the excitation wavelength within the ^{1}MLCT absorption band, which is contrary to our observations of a narrowing and blue shift of the spectrum.

On the other hand, these effects are consistent with vibrational energy relaxation (VER). In solution, VER can be described as a sequence of two processes: intramolecular vibrational redistribution (IVR) followed by a transfer of vibrational energy to the solvent (vibrational cooling). Although the order of events is well established, there is some ambiguity in the literature as to the time scales for IVR and vibrational cooling in large molecules (>25−30 atoms) dissolved in solution. For *trans*-stilbene, IVR is assigned to be as fast (or faster than) as 100 fs followed by cooling to the solvent in 8.5 ps.[38] In a variety of both free base and metalated porphyrins, IVR is generally given a time scale of ∼1 ps while vibrational cooling is ∼10−20 ps.[39−43] In their studies of *fac*-$[Re(MQ^+)(CO)_3(dmb)]^{2+}$ (where dmb = 4,4′-dimethyl-2,2′-bipyridine and MQ^+ = *N*-methyl-4,4′-bipyridinium) Vlček and co-workers describe complicated VER occurring in association with ILET.[44] In the same work, they also assign a time scale of ∼15 ps to vibrational cooling of $[Re(Etpy)(CO)_3(dmb)]^+$ (where Etpy = 4-ethylpyridine) in acetonitrile. In particular, Mizutani et al.[41] contribute a significant interpretation to the subject of VER for molecules in

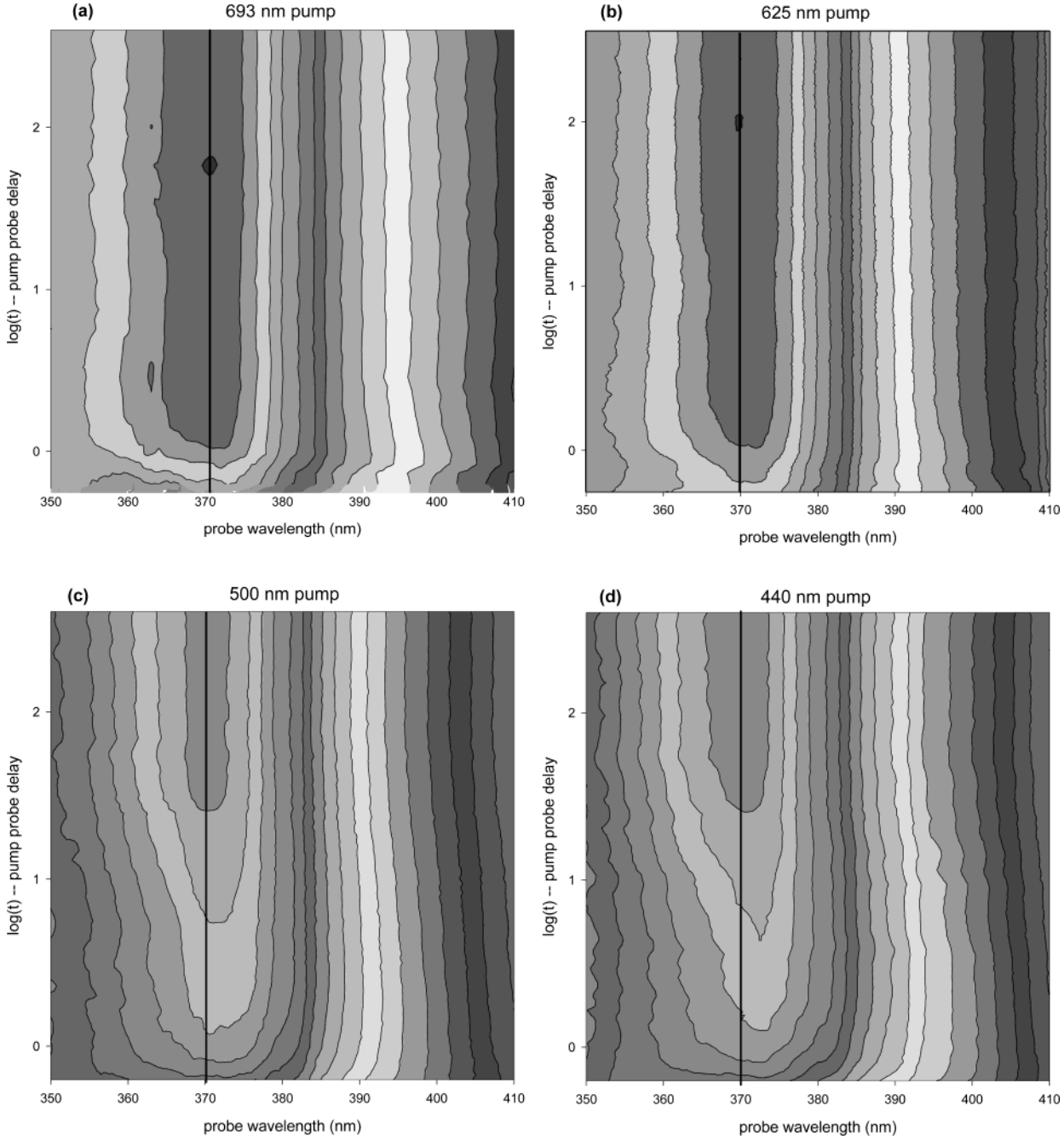

Figure 4. Magic angle transient absorption contour surface plots for ^{1}MLCT and ^{3}MLCT excitations. Surfaces correspond to excitation at (a) 693, (b) 625, (c) 500, and (d) 440 nm. A blue shift of the absorption band maximum is noticeable for panels c and d and absent for panels a and b.

solution as they reaffirm Vanden Bout et al.[45] by noting that the solvent provides the coupling and environment that assists IVR. This really blurs the distinction between the two processes involved in the VER path, especially in our case because it is through solvent fluctuations that the energies of the ligands are brought into resonance so that ILET can occur. Absorption band narrowing in transient absorption spectra has often been interpreted as vibrational cooling.[46] The amount of growth (25% of the total signal), the duration of the spectral evolution displayed (16 ps), and the dependence on excitation energy are all consistent with vibrational cooling observed in other large molecules dissolved in acetonitrile.[38,44] Thus, we assign the 16 ps component to vibrational cooling that occurs *after* a fast, subpicosecond, ISC event. In other words, it is cooling of a vibrationally hot *triplet* state.

In contrast to the 440 and 500 nm data, the triplet difference spectra (also shown in the figure) show no appreciable evolution

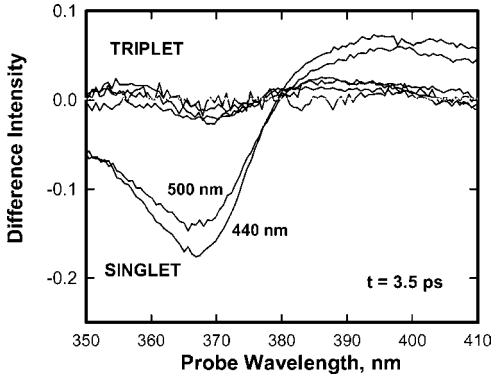

Figure 5. Difference spectra for ^{3}MLCT (693, 675, 650, and 625 nm) and ^{1}MLCT (500 and 440 nm) excitations obtained by subtracting the 380 ps limiting transient spectrum from the 3.5 ps transient spectrum.

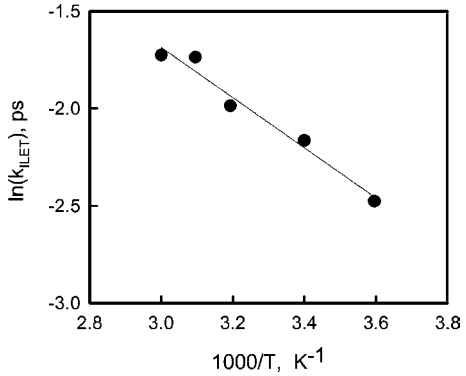

Figure 6. ILET rate constants as a function of temperature for $Os(bpy)_3^{2+}$ in acetonitrile.

after 3.5 ps, suggesting that vibrationally cold complexes are produced, even when the complex is excited at the blue edge of its absorption band (580 nm). This is discussed further in Section C.

2. Absorption Anisotropy. In a recent paper from our laboratory[35] we discussed absorption anisotropy measurements that assign the time scales for the ILET process in $[Os(bpy)_3]^{2+}$ and a mixed ligand osmium complex in acetonitrile and ethylene glycol. In that work, $[Os(bpy)_3]^{2+}$ was excited at the red edge of the ground state absorption spectrum (693 nm). Analysis of the anisotropy amplitudes suggests that photon absorption produces a distribution of excited state wave functions. For a majority of the ensemble, the excited state is localized on a single ligand, indicating that the solvent inhomogeneity is capable of overcoming the ligand−ligand electronic coupling. While this observation is at least qualitatively consistent with conventional thought, our experiments also suggest that in a sizable fraction (∼35−40%) of the ensemble the excited state is delocalized over two or more of the ligands.

In this work, we have measured the ILET rate as a function of temperature, which provides an estimate of the electron-transfer activation energy and electronic coupling. In addition, we have extended the anisotropy measurements to other excitation wavelengths. When these results are combined with the magic angle data presented in the previous section, a dynamical picture emerges that describes the evolution of the excited state following photoexcitation into both the singlet and triplet absorption bands.

a. Temperature Dependence. We have performed absorption anisotropy measurements with 693 nm excitation light at a series of temperatures and the results are displayed in Figure 6. From the slope, we obtain an activation enthalpy of 850 cm^{-1}. This represents the first direct measurement of the ILET barrier height in a polypyridyl complex.

The activation energy is related to the driving force ($\Delta G°$), solvent reorganization energy (λ), and the electronic coupling between the ligands in the MLCT excited state (H_{el}), using an equation developed by Brunschwig and Sutin:[47]

$$\Delta G^* = \frac{\lambda}{4} + \frac{\Delta G°}{2} + \frac{(\Delta G°)^2}{4(\lambda - 2H_{el})} - H_{el} + \frac{{H_{el}}^2}{\lambda + \Delta G°} \quad (5)$$

λ has both inner- and outer-sphere contributions, i.e. $\lambda = (\lambda_I + \lambda_O)$. The inner-sphere contribution is approximated to be twice the reorganization energy associated with the MLCT excitation, i.e. $2\lambda_I^{MLCT}$, which can be determined from emission spectral fitting.[48] The factor of 2 arises because vibrational modes on two of the ligands are affected in the ILET process. We thus estimate $\lambda_I \approx 2000$ cm^{-1}. The outer-sphere contribution is estimated from dielectric continuum models[49] to be about 2500−3000 cm^{-1}. Taking $\Delta G° = 0$ for the symmetric ET process, $\lambda = (\lambda_I + \lambda_O) = 4500$ cm^{-1}, and assuming that the activation entropy is small (i.e., $\Delta G^* \approx \Delta H^*$), we estimate H_{el} to be around 300−400 cm^{-1}.

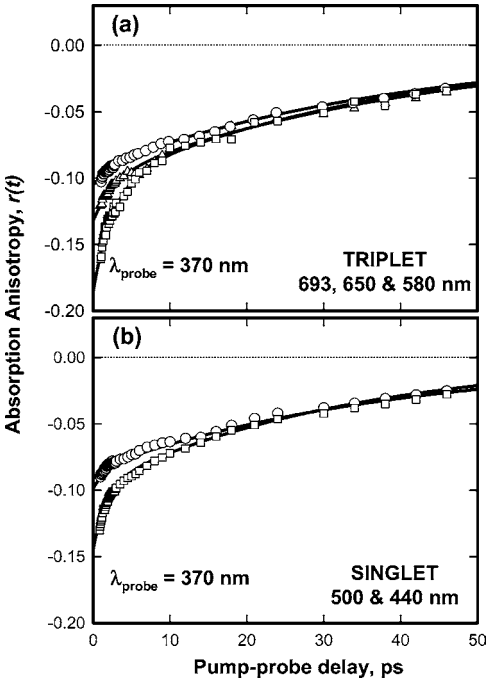

Figure 7. Absorption anisotropy decays at 370 nm for $[Os(bpy)_3]^{2+}$ in room temperature acetonitrile. The upper panel (a) shows transients for excitation into the ^{3}MLCT state: 693 (□), 650 (△), and 580 nm (○). The lower panel (b) shows transients for excitation into ^{1}MLCT state: 500 (□) and 440 nm (○). The solid lines are the result of biexponential to the data.

b. Pump-Wavelength-Dependent Decay Kinetics. Displayed in Figure 7 are anisotropy decays at 370 nm for $[Os(bpy)_3]^{2+}$ in acetonitrile. The upper panel shows $r(t)$ following triplet excitations (693, 650, and 580 nm) while the lower one shows the $r(t)$ following singlet excitations (500 and 440 nm). The most striking trend observed in this series of decays is the change in amplitude of the fast component. As the excitation wavelength is moved to the blue of 693 nm, the fast component gradually diminishes and by 580 nm it is nearly gone. It then reappears at the red edge of the singlet absorption band (500 nm), and again decreases as the excitation wavelength is shifted to higher energy.

The solid lines in Figure 7 are the results of biexponential fits for each data set. The time constants for the fast and slow kinetic components are given in Table 1. (Note that the anisotropy decays at 625 and 675 nm are not shown in the figure.) The slow component is attributed to rotational diffusion, and is relatively independent of excitation wavelength, both in its time constant (∼40 ps) and its amplitude. These results are consistent with our previously published results for $[Os(bpy)_3]^{2+}$.[35] The fast component of the decay is assigned to ILET. The ∼3 ps time scale observed at the 693, 675, and 650 nm excitations also agrees with our previous work.[35] For the other two triplet excitations (625 and 580 nm), the time constant obtained from the biexponential fit is likely an average of a component much faster than 1 ps and a slower one of approximately 3 ps. A more quantitative measure of these two "fast" components is hampered by a decrease in amplitude at these wavelengths. The 500 nm singlet excitation has a fast time component of 1.5 ps, about twice as fast as the lowest energy

TABLE 1: Summary of Fast and Slow Time Constants Resulting from Biexponential Fits of the Absorption Anisotropy Decays, $r(t)$[a]

	excitation wavelength, nm						
	693	675	650	625	580	500	440
fast component (ps)	2.8	3.0	3.1	2.5[b]	1.2[b]	1.5	0.7[b]
slow component (ps)	41	41	42	41	38	33	39

[a] Nonlinear least-squares analysis revealed that the $r(t)$ transients at a probe wavelength of 370 nm (the peak of the $\pi-\pi^*$ absorption) exhibit biphasic kinetics for all excitations. [b] Our kinetic analysis suggests that these are most likely an average of two kinetic components, a fast one that could not be resolved ($\ll$1 ps) and a slower one ($\approx$3 ps for 625 and 580 nm excitations and $\approx$1.5−2 ps for the 440 nm excitation).

triplet excitations. Like the blue triplet excitations, the fast component in the 440 nm decay also appears to be a combination of two subcomponents.

c. Anisotropy Amplitudes. The initial amplitude of the absorption anisotropy can provide details regarding the symmetry of the optically prepared excited state. For an initially *localized* excited state, the pump and probe transition dipoles are orthogonal to each other, and the excited-state absorption band will have $r(t=0) = -0.2$. If the wave function of the initial state is delocalized, on the other hand, then $r(t=0) = -0.1$. Thus, the value of $r(t=0)$ provides a measure of the degree of localization in the optically prepared excited state.

Obtaining the initial anisotropy amplitude from a transient absorption experiment is not necessarily straightforward,[34,35] since the observed absorption anisotropy is a weighted average of the *absorption* and *bleach* anisotropies, $\langle r_\alpha(t)\rangle$ and $\langle r_\beta(t)\rangle$, respectively. The observed anisotropy is given by

$$r(t) = \frac{\alpha^T}{\alpha^T - \beta^T}\langle r_\alpha(t)\rangle - \frac{\beta^T}{\alpha^T - \beta^T}\langle r_\beta(t)\rangle \qquad (6)$$

where α^T and β^T are the total absorption and total bleach contributions, respectively (both are positive quantities). We have developed a procedure for modeling the anisotropy data of $[Os(bpy)_3]^{2+}$, the details of which are discussed elsewhere.[35] But briefly, we use eq 6 to simultaneously fit the observed $r(t)$ transient data at seven probe wavelengths (360, 370, 375, 380, 385, 390, and 395 nm) across the $\pi-\pi^*$ absorption band. From the analysis we extract the *absorption* anisotropy, $\langle r_\alpha(t)\rangle$, which has the following form:

$$\langle r_\alpha(t)\rangle = a_F^{\lambda} \exp(-k_F t) + a_S^{\lambda} \exp(-k_S t) \qquad (7)$$

The time constants (k_F and k_S) are for the fast and slow components of the decay, respectively. The related amplitudes (a_F^{λ} and a_S^{λ}) are both equal to −0.1 when the initial wave function is localized on a single ligand, and then randomizes among the three ligands through ILET.

The values of a_F^{λ} and a_S^{λ} at each excitation wavelength are plotted in Figure 8. The gray bands that accompany the amplitudes reflect the uncertainty in the values obtained from the model. Regardless of excitation wavelength, the amplitudes of the slow component (a_S^{λ}) are ca. −0.1, which is the value expected once the photoexcited electron scrambles among the three ligands through ILET. The fast amplitude reflects the nature of the *initial* state, and unlike the slow component, the fast component exhibits a strong dependence on excitation wavelength, indicating that the nature of the excited-state wave function depends on the color of the photon absorbed. Localized states would have fast amplitudes (a_F^{λ}) equal to −0.1, while

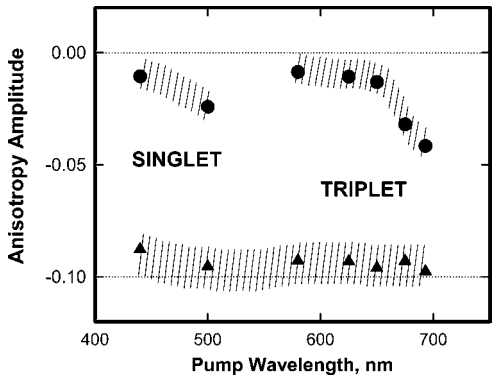

Figure 8. Initial absorption anisotropy amplitudes as a function of pump wavelength for $[Os(bpy)_3]^{2+}$. The solid circles (●) and triangles (▲) correspond to the initial amplitudes of the fast and slow components of eq 7 (a_F^{λ} and a_S^{λ}), respectively. The hatching that accompanies the amplitudes represents the uncertainty range associated with the modeling. The values for a_F^{λ} are all less than −0.1, which suggests differing degrees of initial excited-state delocalization with a strong dependence on excitation wavelength. The values for a_S^{λ} are $\approx$ −0.1, which is the expected value after the electron randomizes through ILET.

for excited states delocalized over all three ligands a_F^{λ} would be zero. When the complex is excited at the red edge of the ^{3}MLCT absorption band, the initial anisotropy ($a_F^{\lambda} + a_S^{\lambda}$) is between −0.1 and −0.2, indicating that there is a mixture of localized and delocalized excited states in the initial ensemble.

C. Excited-State Evolution. Regardless of the color of light used to excite the molecules, the agreement of the four 380 ps magic angle spectra in Figure 3 indicates that at long times after photoexcitation the system ultimately resides in the same low-energy triplet state. However, the path taken to arrive in this state is very dependent on excitation wavelength. The transient spectra that result from excitation to the triplet state exhibit one type of behavior, while the transient spectra observed after singlet excitation show something very different (Section B1). Thus, any description of the excited-state evolution must distinguish direct population of the triplet state from the triplet state formed after intersystem crossing from the singlet. Four distinct scenarios are considered: (1) low-energy excitation in the ^{3}MLCT band, (2) high-energy excitation of the triplet, (3) low-energy excitation of the singlet, and (4) high-energy excitation of the singlet. These four transitions are summarized in Figure 9.

The MLCT excited states consist of multiple minima that correspond to locating the photoexcited electron on each of the ligands. For clarity, only two minima are shown in the figure; however, in reality three exist. A three-dimensional view of this surface is shown in our previous paper. The point where the two diabatic curves cross corresponds to the solvent configuration that brings (at least) two of the ligands into resonance, and because of the ligand−ligand coupling the localized basis states are mixed to form two delocalized states. Because of the strong ligand−ligand electronic coupling in this system, the diabatic surfaces undergo an avoided crossing to form the adiabatic surfaces depicted in the figure. It is worth noting that Kelley and co-workers[50,51] examined the ILET process in $[Os(bpy)_3]^{2+}$ via absorption anisotropy measurements. Although the time resolution of their apparatus was limited to 10 ps, they concluded that $[Os(bpy)_3]^{2+}$ ILET dynamics in acetonitrile take place on a 130 ps time scale and occur in a nonadiabatic coupling limit.[50,51] These findings are in direct contrast to our observations.

1. Low-Energy ^{3}MLCT Excitation. When the $[Os(bpy)_3]^{2+}$ complex is excited at the red edge (693 nm) of its triplet band,

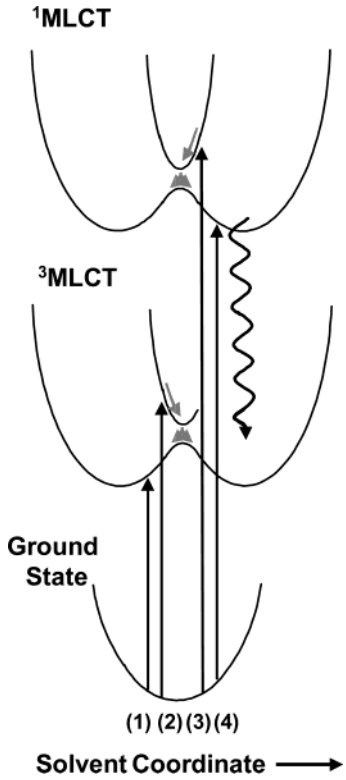

Figure 9. Schematic potential energy surfaces for the $[Os(bpy)_3]^{2+}$ ground state, ^{3}MLCT state, and ^{1}MLCT state in polar solvents. The MLCT excited states are represented by adiabatic surfaces formed from the avoided crossing of potential wells that correspond to the localization of the photoexcited electron on a different ligand. The actual surface would possess three wells, while for clarity, only two are shown here. The four transitions labeled (1)−(4) correspond to the different types of transitions explored in this work. See text for details.

the initial anisotropy is −0.14, which indicates that the excited ensemble consists of both localized and delocalized excited states. While some fraction of the ensemble is delocalized over two or more of the ligands, most of the population starts out on the lowest three-dimensional surface in Figure 9, in a localized region of the parabolic potential. The time scale for movement of the excited state from one parabolic surface to another (i.e. ILET) is equal to $1/3(k_{obs} - k_{rot})$, where k_{obs} is the observed decay rate (fast component) and k_{rot} is the rotational diffusion rate (slow component), i.e., $k_{obs} = (3k_{ILET} + k_{rot})$. Using the kinetic rates presented in Table 1 yields an ILET time of ≈9 ps.

2. High-Energy ^{3}MLCT Excitation. Excitations at 625 and 580 nm show qualitatively different anisotropy behavior. Both exhibit initial anisotropy values in the neighborhood of −0.11. The time scale of the fast component is also different, and as stated earlier, both wavelengths show some evidence of a fast (<1 ps) decay time. Both observations are consistent with an initial state starting on the upper adiabatic surface instead of the lowest one. In such a case, the excited state would initially be localized, then quickly delocalize over two ligands as it approached the avoided crossing from above.

The differences between these potential surfaces in Figure 9 correspond to the different solvent configurations around each ligand. When excited to the higher energy surface, the MLCT excitation is placed on a ligand with a less than favorable solvent configuration around it. Thus, as the excitation energy is increased, the excess energy is placed in the solvent degrees of freedom rather than molecular vibrations. Our molecular dynamics simulations support the notion that in the average solvent configuration the energy difference between the best solvated and worst solvated ligands is about 2500 cm^{-1}, nearly the entire width of the ^{3}MLCT absorption band. By promoting the electron to a less-solvated ligand (i.e. upper adiabatic surface) the complex would remain vibrationally cold and this would explain the lack of evolution in the magic angle spectra.

3. Low-Energy ^{1}MLCT Excitation. Following photoexcitation at 500 nm, the complex undergoes rapid ISC to the triplet state, with the MLCT excitation remaining on the ligand to which the electron was initially excited. The ISC process produces a vibrationally hot triplet state, which then cools through energy transfer to the solvent (16 ps). As this state cools, it undergoes ILET events with an electron transfer time of 4.5 ps (1.5 ps anisotropy decay), which is consistent with the expectation that ILET should proceed more quickly with the introduction of excess vibrational energy.

4. High-Energy ^{1}MLCT Excitation. At 440 nm excitation, the complex is promoted to one of the upper Marcus surfaces in the *singlet* state, which would lead to rapid delocalization as the system approached the avoided crossing from above. As occurs in the 500 nm excitation, ISC yields a vibrationally hot triplet state that reaches thermal equilibrium with the solvent on a 16 ps time scale.

Acknowledgment. Funding for this project was provided by The Research Corporation (RI0048), the Petroleum Research Fund (36385-G6), and the National Science Foundation (CHE-0301266). The authors also acknowledge a number of discussions with Thomas J. Meyer at Los Alamos National Laboratory.

References and Notes

(1) Demas, J. N.; Crosby, G. A. *J. Am. Chem. Soc.* **1971**, *93*, 2841−2847.
(2) Van Houten, J.; Watts, R. J. *J. Am. Chem. Soc.* **1976**, *98*, 4853.
(3) Van Houten, J.; Watts, R. J. *Inorg. Chem.* **1978**, *17*, 3381.
(4) Vlcek, A. *Coord. Chem. Rev.* **2000**, *200*, 933−977.
(5) Lumpkin, R. S.; Kober, E. M.; Worl, L. A.; Murtaza, Z.; Meyer, T. J. *J. Phys. Chem.* **1990**, *94*, 239−243.
(6) Meyer, T. J. *Pure Appl. Chem.* **1986**, *58*, 1193−1206.
(7) Caspar, J. V.; Westmoreland, T. D.; Allen, G. H.; Bradley, P. G.; Meyer, T. J.; Woodruff, W. H. *J. Am. Chem. Soc.* **1984**, *106*, 3492−3500.
(8) Durham, B.; Caspar, J. V.; Nagle, J. K.; Meyer, T. J. *J. Am. Chem. Soc.* **1982**, *104*, 4803−4810.
(9) Creutz, C.; Chou, M.; Netzel, T. L.; Okumura, M.; Sutin, N. *J. Am. Chem. Soc.* **1980**, *102*, 1309−1319.
(10) Kuciauskas, D.; Freund, M. S.; Gray, H. B.; Winkler, J. R.; Lewis, N. S. *J. Phys. Chem. B* **2001**, *105*, 392−403.
(11) Schwarz, O.; Van Loyen, D.; Jockusch, S.; Turro, N. J.; Durr, H. *J. Photochem. Photobiol., A* **2000**, *132*, 91−98.
(12) Kohle, O.; Ruile, S.; Gratzel, M. *Inorg. Chem.* **1996**, *35*, 4779−4787.
(13) Albano, G.; Belser, P.; Daul, C. *Inorg. Chem.* **2001**, *40*, 1408−1413.
(14) Belser, P.; Bernhard, S.; Blum, C.; Beyeler, A.; De Cola, L.; Balzani, V. *Coord. Chem. Rev.* **1999**, *192*, 155−169.
(15) Kalyanasundaram, K.; Gratzel, M. *Coord. Chem. Rev.* **1998**, *177*, 347−414.
(16) Launay, J. P.; Fraysse, S.; Coudret, C. *Mol. Cryst. Liq. Cryst.* **2000**, *344*, 125−132.
(17) Harriman, A.; Ziessel, R. *Coord. Chem. Rev.* **1998**, *171*, 331−339.
(18) Damrauer, N. H.; Cerullo, G.; Yeh, A.; Boussie, T. R.; Shank, C. V.; Mccusker, J. K. *Science* **1997**, *275*, 54−57.
(19) Bhasikuttan, A. C.; Suzuki, M.; Nakashima, S.; Okada, T. *J. Am. Chem. Soc.* **2002**, *124*, 8398−8405.
(20) Browne, W. R.; Coates, C. G.; Brady, C.; Matousek, P.; Towrie, M.; Botchway, S. W.; Parker, A. W.; Vos, J. G.; Mcgarvey, J. J. *J. Am. Chem. Soc.* **2003**, *125*, 1706−1707.
(21) Mabrouk, P. A.; Wrighton, M. S. *Inorg. Chem.* **1986**, *25*, 526−531.
(22) Bradley, P. G.; Kress, N.; Hornberger, B. A.; Dallinger, R. F.; Woodruff, W. H. *J. Am. Chem. Soc.* **1981**, *103*, 7441−7446.

(23) Riesen, H.; Wallace, L.; Krausz, E. *Inorg. Chem.* **2000**, *39*, 5044−5052.
(24) Yersin, H.; Strasser, J. *Coord. Chem. Rev.* **2000**, *208*, 331−364.
(25) Yersin, H.; Humbs, W. *Inorg. Chem.* **1999**, *38*, 5820−5831.
(26) Riesen, H.; Krausz, E. *Chem. Phys. Lett.* **1998**, *287*, 388−394.
(27) Riesen, H.; Wallace, L.; Krausz, E. *Int. Rev. Phys. Chem.* **1997**, *16*, 291−359.
(28) Karki, L.; Hupp, J. T. *Inorg. Chem.* **1997**, *36*, 3318−3321.
(29) Humbs, W.; Strasser, J.; Yersin, H. *J. Lumin.* **1997**, *72*−*4*, 677−678.
(30) Riesen, H.; Wallace, L.; Krausz, E. *J. Chem. Phys.* **1995**, *102*, 4823−4831.
(31) Huber, P.; Yersin, H. *J. Phys. Chem.* **1993**, *97*, 12705−12709.
(32) Oh, D. H.; Boxer, S. G. *J. Am. Chem. Soc.* **1989**, *111*, 1130−1131.
(33) Kober, E. M.; Sullivan, B. P.; Meyer, T. J. *Inorg. Chem.* **1984**, *23*, 2098−2104.
(34) Yeh, A. T.; Shank, C. V.; McCusker, J. K. *Science* **2000**, *289*, 935−938.
(35) Shaw, G. B.; Brown, C. L.; Papanikolas, J. M. *J. Phys. Chem. A* **2002**, *106*, 1483−1495.
(36) Shaw, G. B.; Papanikolas, J. M. *J. Phys. Chem. B* **2002**, *106*, 6156−6162.
(37) König, E.; Kremer, S. *Chem. Phys. Lett.* **1970**, *5*, 87−90.
(38) Kovalenko, S. A.; Schanz, R.; Hennig, H.; Ernsting, N. P. *J. Chem. Phys.* **2001**, *115*, 3256−3273.
(39) Baskin, J. S.; Yu, H. Z.; Zewail, A. H. *J. Phys. Chem. A* **2002**, *106*, 9837−9844.
(40) Yu, H. Z.; Baskin, J. S.; Zewail, A. H. *J. Phys. Chem. A* **2002**, *106*, 9845−9854.
(41) Mizutani, Y.; Uesugi, Y.; Kitagawa, T. *J. Chem. Phys.* **1999**, *111*, 8950−8962.
(42) Yu, H. Z.; Baskin, J. S.; Steiger, B.; Wan, C. Z.; Anson, F. C.; Zewail, A. H. *Chem. Phys. Lett.* **1998**, *293*, 1−8.
(43) Eom, H. S.; Jeoung, S. C.; Kim, D.; Ha, J. H.; Kim, Y. R. *J. Phys. Chem. A* **1997**, *101*, 3661−3669.
(44) Liard, D. J.; Busby, M.; Farrell, I. R.; Matousek, P.; Towrie, M.; Vlček, A. *J. Phys. Chem. A* **2004**, *108*, 556−567.
(45) Vanden Bout, D.; Freitas, J. E.; Berg, M. *Chem. Phys. Lett.* **1994**, *229*, 87−92.
(46) Gustafson, T. L.; Kyllo, E. M.; Frost, T. L.; Sun, R. G.; Lim, H. S.; Wang, D. K.; Epstein, A. J.; Lefumeux, C.; Burdzinski, G.; Buntinx, G.; Poizat, O. *Synth. Met.* **2001**, *116*, 31−34.
(47) Brunschwig, B. S.; Sutin, N. *Coord. Chem. Rev.* **1999**, *187*, 233−254.
(48) Murtaza, Z.; Graff, D. K.; Zipp, A. P.; Worl, L. A.; Jones, W. E.; Bates, W. D.; Meyer, T. J. *J. Phys. Chem.* **1994**, *98*, 10504−10513.
(49) Brunschwig, B. S.; Ehrenson, S.; Sutin, N. *J. Phys. Chem.* **1987**, *91*, 4714−4723.
(50) Pogge, J. L.; Kelley, D. F. *Chem. Phys. Lett.* **1995**, *238*, 16−24.
(51) Cushing, J. P.; Butoi, C.; Kelley, D. F. *J. Phys. Chem. A* **1997**, *101*, 7222−7230.